Ag Nanoparticles and their Application in Low-Temperature Bonding of Cu

by

Hani Abdulkareem Alarifi

A thesis

presented to the University of Waterloo

in fulfillment of the

thesis requirement for the degree of

Doctor of Philosophy

in

Mechanical Engineering

Waterloo, Ontario, Canada, 2013

© Hani Abdulkareem Alarifi 2013

I hereby declare that I am the sole author of this thesis. This is a true copy of the thesis, including any required final revisions, as accepted by my examiners. I understand that my thesis may be made electronically available to the public.

ABSTRACT

Ag nanoparticle (NP) paste was fabricated and used to bond Cu wire to Cu foil at low temperatures down to 433 K. The relatively low bonding temperature promotes this method to be used in polymer-based flexible electronics, which cannot withstand high bonding temperatures due the possible melting of the polymer substrate. Unlike low-temperature soldering techniquies, bonds formed by this method was proved to withstand temperatures higher than the bonding temperature, which also promotes it to be used in electronics that operate at high temperatures.

The Ag NP paste was developed by increasing the concentration of 50 nm Ag NP sol from 0.001 vol.% to 0.1 vol.% by centrifugation. The 0.001 vol.% Ag NP sol was fabricated in water by reducing silver nitrate ($AgNO_3$) using sodium citrate dihydrate ($Na_3C_6H_5O_7.2H_2O$). The bond was formed by solid state sintering among the individual Ag NPs and solid state bonding of these Ag NPs onto both Cu wire and foil. Metallurgical bonds between Ag NPs and Cu were confirmed by transmission electron microscopy (TEM). The Ag NPs were coated with an organic shell to prevent sintering at room temperature. It was found that the organic shell decomposed at 433 K, defining the lowest temperature at which a bond could be formed. Shear tests showed that the joint strength increased as the bonding temperature increased due to enhanced sintering of Ag NPs at higher temperatures.

For better understanding of the melting and the sintering kinetics of Ag NPs, a molecular dynamics (MD) simulation based on the embedded atom method (EAM) was conducted to different sizes of Ag NPs with diameters between 4 nm and 20 nm. Programmed heating of an equal rate was applied to all sizes of NPs to find the complete melting and surface premelting points and sintering kinetics of the Ag NPs. The initial structural configuration of the Ag NPs was FCC truncated octahedral, which found to be stable for this size range of NPs. As a first step toward drawing a phase map of stable solid phases of Ag NPs at different temperatures and sizes of Ag NPs, the stability of the FCC truncated octahedral was studied for Ag NPs in size range of 1 nm to 4 nm. The smallest Ag NPs at which this configuration is stable was determined as 1.8 nm.

Unlike the previous theoretical models, this MD model predicted both complete melting and surface premelting points for a wider size range of NPs. Melting kinetics showed three different trends that are, respectively, associated with NPs in the size ranges of 4 nm to 7 nm, 8 nm to 10 nm, and 12 nm to 20 nm. Ag NPs in the first range melted at a single temperature without passing through a surface premelting stage. Melting of the second range started by forming a quasi-liquid layer that expanded to the core, followed by the formation of a liquid layer of 1.8 nm thickness that also subsequently expanded to the core with increasing temperature, completing the melting process. For particles in the third range, the 1.8 nm liquid layer was formed once the thickness of the quasi-liquid layer reached 5 nm. The liquid layer expanded to the core and formed thicker stable liquid layers as the temperature increased toward the complete melting point. The ratio of the quasi-liquid layer thickness to the NP radius showed a linear relationship with temperature.

Sintering kinetics of two Ag NPs in the size range of 4 nm to 20 nm, and sintering of three and four Ag NPs of 4 nm diameter was also studied by MD simulation. The sintering process passed through three main stages. The first was the neck formation followed by a rapid increase of the neck radius to particle radius ratio at 50 K for 20 nm particles and at 10 K for smaller NPs. The second was characterized by a gradual linear increase of the neck radius to particle radius ratio as the temperature of the sintered structure was increased to the surface premelting point. A twin boundary was formed during the second stage that relaxed the sintered structure and decreased the average potential energy (PE) of all atoms. The third stage of sintering was a rapid shrinkage during surface premelting of the sintered structure. Based on pore geometry, densification occurred during the first stage for three 4 nm particles and during the second stage for four 4 nm particles. Sintering rates obtained here were higher than those obtained by theoretical models generally used for predicting sintering rates of micro-particles.

In memory of my father

Abdulkaeem Nasser Alarifi

To my mother with love

Ni’ma Ahmed Madwar

To my siblings with love

Abeer, Ibtesam, Nasser, Ahmed, and Fahad.

ACKNOWLEDGMENTS

I would like to convey my gratitude to my supervisors, Prof. Mustafa Yavuz, and Prof. Norman Zhou for their ongoing and unconditional guidance during my study at the University of Waterloo. They have helped me to greatly improve my research skills, critical thinking, and technical writing.

I would also like to express my sincere appreciation to Prof. Anming Hu at CAMJ, Prof. Murat Atis at Nevsehir University in Turkey, Prof. Cem Ozdogan at Cankaya University in Turkey, and Prof. Scott Lawson at the University of Waterloo. I was lucky to work closely to other CAMJ members, which introduced me to different joining methods and research fields ranging from welding of different bulk materials to nanojoining.

I greatly appreciate the financial support of King Abdulaziz City for Science and Technology (KACST) in Riyadh, Saudi Arabia during my study. I would also like thank my sister Abeer for her care and support during all stages of my study.

TABLE OF CONTENTS

LIST OF FIGURES

LIST OF TABLES

1. INTRODUCATION

1.1 Background

Replacing Pb based solders due to the hazards of Pb on human health became a crucial issue [1]. Current candidates for replacing Pb solders such as Au-Sn alloys, Bi alloys and Zn alloys suffer poor corrosion resistance, poor processability, and high cost [2-4]. Also, developing a bonding method that can work at temperatures below 523 K is important for the development of polymer-based flexible electronics. It is also economically effective to decrease the bonding temperatures for electronic packaging and interconnections. On the other hand, electronics that operate at high temperatures needs a bonding method that can withstand these high operating temperatures. Forming joints that can withstand higher temperatures than the bonding temperature has great advantage over conventional soldering techniques, which form bonds that cannot withstand high temperatures due to the low melting point of the soldering material [5]. Fig. 1.1 shows the operative temperature range of electronics that are used in different industries [6].

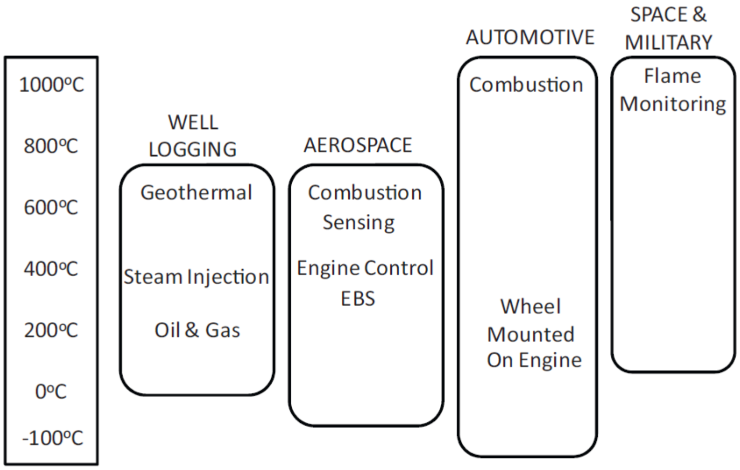

Fig. 1.1 Indicative temperature range [6].

During the last decades, nanomaterials have attracted great attention due to their potential usage in different fields that range from medicine to energy, electronics, and other fields as well. Due to their outstanding electronic properties, Ag nanoparticles (NPs) have recently been used in bonding of electronics. As shown by the schematic description in Fig.1.2, Ag NPs can be used to bond two pieces of metals by sintering between these individual NPs combines with sintering of the NPs on the metal pieces. Sintering rates and the diffusion process can be enhanced by applying temperature and pressure during the bonding process. Ag NPs coated with organic shells have been used to bond metals at temperature as low as 523 K [7-9]. These bonds were formed by sintering of NPs, which started at the temperature at which the organic shell decomposes. The organic shells serve as barriers between NPs in order to prevent their possible agglomeration and sintering at room temperature (RT).

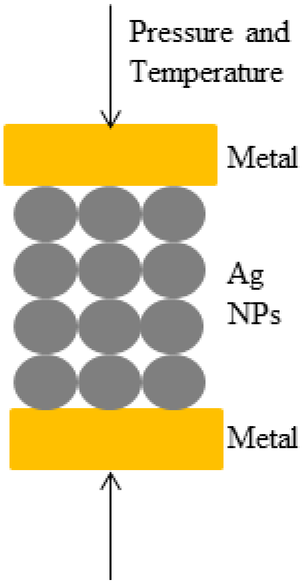

Fig. 1.2 A schematic diagram showing bonding procedure of two pieces of metals by Ag nanoparticles.

Fundamental understanding of the thermodynamic properties of Ag NPs is important because of their potential in utilizing nano scale devices [1,10], electronics packaging [11,12], and developing lead free soldering materials [13]. Materials properties such as melting points, mechanical properties, and electrical properties change at the nano-scale. Therefore, properties of the bulk and the theoretical models found in literature may not be valid for nanomaterials. It has been proved experimentally and theoretically that NPs melt at temperatures below the melting point of the bulk due to their higher surface energy [14-20]. Liquid drop model [21], Shi's model [22], and Hanszen's model [23] are found to be the most popular models for determining the complete melting point (T_m) of NPs. Liquid drop model was based on the variation of cohesive energy and surface energy of the NPs. Shi's model was developed in terms of Lindemann's criterion [24], which suggests that a NP melts when the root mean square displacement (rmsd) of the atoms exceeds a certain fraction of the interatomic distance.

While liquid drop model [21] and Shi's model [22] have assumed homogenous melting of a NP, Hanszen's model [23] has considered, melting of a NP starts at the surface by forming a thin liquid layer, which expands to the core and complete full transition of the structure from solid to liquid. This initial stage of melting is called surface premelting, which initiates in order to reduce the total interfacial energy of the material. The diversity of the analytical models found in literature for determining T_m of NPs and the different results that can be obtained by them, makes it difficult to decide which model can correctly predict T_m. Also, the kinetics of surface premelting of Ag NPs is still not well understood and at what range of temperatures it occurs.

1.2 Objectives

The main objective of this research is to develop an Ag NP paste that can be used for bonding in polymer-based flexible electronics and in electronics that operate at high temperatures. As in nano-scale materials, Ag NPs are expected to have different properties than the bulk. Therefore, molecular dynamics simulation will be performed to understand melting and sintering kinetics, and the stability of FCC truncated octahedral Ag NPs. The objectives of this research can be specified in the following points

1 To fabricate an Ag NP paste that can be used to bond Cu wires to Cu foils at low temperatures. The formed bond should withstand higher temperatures than the bonding temperature.

2 To determine complete melting and surface premelting points of Ag NPs in size range of 4 nm to 20 nm and compare the results with the previously developed theoretical models.

3 To study the stability of FCC truncated octahedral configuration at different sizes of Ag NPs.

4 To study sintering kinetics of Ag NPs in size range of 4 nm to 20 nm and to compare the results with previously developed sintering theories of microparticles.

1.3 Major Results and Contributions

Ag Nanoparticle Paste for Low-Temperature Bonding of Cu

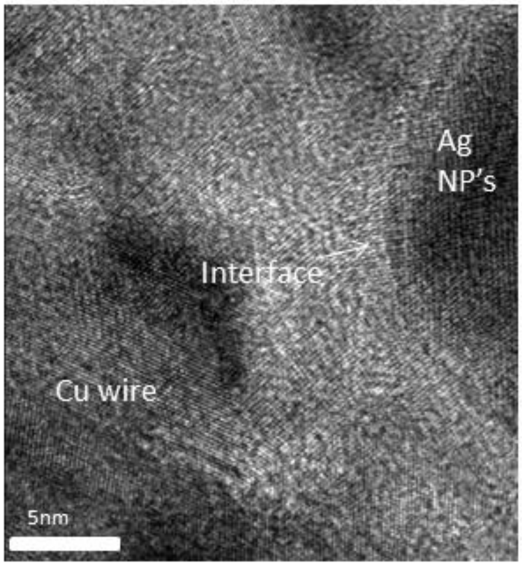

A silver NP paste was fabricated and used to bond Cu wires to Cu foils at 433 K, which is much lower than conventional soldering temperatures. This low bonding temperature has a great advantage in bonding in polymer-based flexible electronics, which require a low bonding temperature that would not melt the polymer substrate. The bond strength was increased as the temperature of the bonding is increased toward 573 K. Unlike bonds formed by conventional soldering methods, bonds formed here could withstand operating temperatures that are higher than the bonding temperature, which promotes this method to be used in electronics that operate at relatively high temperatures.

Determination of Complete Melting and Surface Premelting Points of Ag Nanoparticles

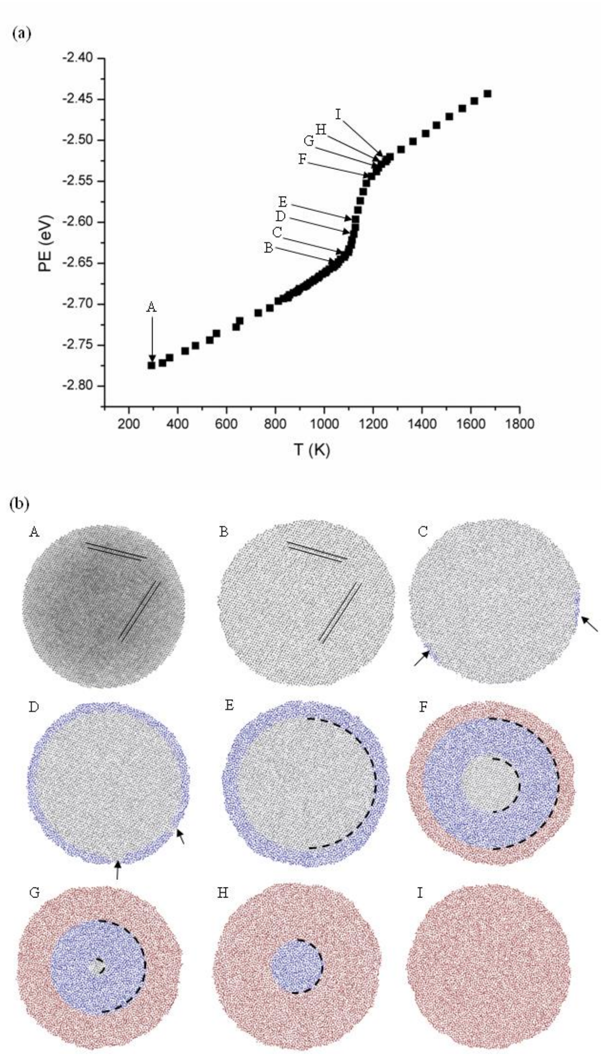

Different than previous melting theories, Ag nanoparticles in size range of 8 nm to 20 nm are found to melt in range of temperatures that start at the surface premelting point (T_{sm}), at which quasi-liquid ponds started to form on the surface of the NP. These ponds expand and coalesce and form the first liquid shell of 1.8 nm thickness. The ratio of the thickness of the quasi-liquid layer to the NP radius increased linearly as the temperature of the NP increased toward its complete melting point (T_m). The previous theoretical models were found to be only valid for certain ranges of NP sizes. Complete melting points obtained in this study fit well with Liquid Drop Model [21] and Shi's model [22] in size range of 4 nm to 7 nm, and with Hanszen's model [23] in size range of 8 nm to 12 nm. Complete melting points of larger NPs have not been predicted earlier due to the formation of multiple stable liquid layers between T_{sm} and $T_{m.}$

Molecular Dynamics Simulation of the Stability of FCC Truncated Octahedral Ag Nanoparticles

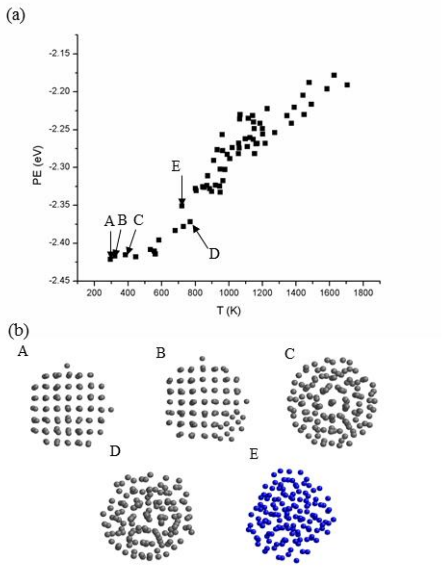

The minimum size at which FCC truncated octahedral Ag NPs is stable below T_m was determined as 1.8 nm. Solid to solid phase transition from FCC truncated octahedral to icosahedral configuration was confirmed during heating of 1.2 nm. These results are considered as the first step toward drawing a phase map of Ag NPs at different sizes and temperatures.

Molecular Dynamics Simulation of Sintering of Ag Nanoparticles

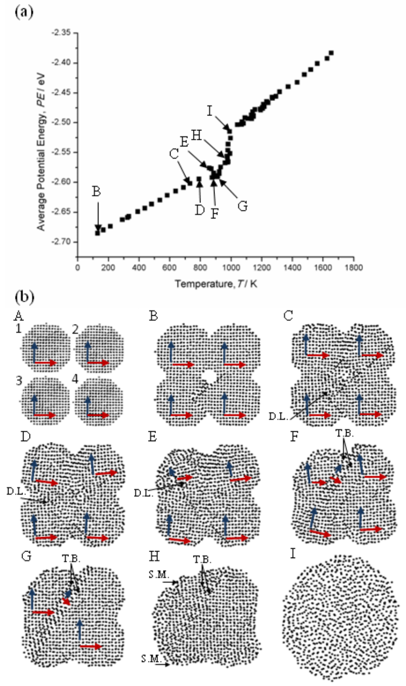

Sintering kinetics of Ag NPs of different sizes in range of 4 nm to 20 nm was studied by MD simulation. The first two stage of sintering was found to agree with the previous sintering theories and are characterized by a formation of a neck followed by a gradual linear increase in the neck radius to NP radius ratio. However, the third (final) stage was found to be different than previous sintering theories and is characterised by a rapid shrinkage driven by liquid state sintering between T_{sm} and T_m of the sintered structure.

1.4 Organisation of Thesis

This thesis is divided into seven chapters that are organised as follow. The second chapter provides the reader with a literature survey on Ag NPs pastes that have been used as bonding materials, theoretical and experimental background on melting and surface premelting of bulk and of nanomaterials, solid state configurations and solid to solid phase transition of NPs, and finally, a brief background on sintering of microparticles and nanoparticles, as well as sintering of NPs on metallic substrates. Chapter three reports the experimental, the numerical, and the analytical methods used in this thesis. Chapter four provides a detailed characterisation of the Ag NP paste and the formed bonds between the Cu wires and the Cu foils. The Ag NPs was characterised by scanning electron microscopy (SEM), Thermogravimetric Analysis (TGA), and Raman spectroscopy. The formed bonds were characterized by shear tests, and SEM, and transmission electron microscopy (TEM) of the interface. Chapter five reports the molecular dynamics simulation results on periodic heating of individual Ag nanoparticles in size range of 4 nm to 20 nm. Complete melting and surface premelting points for each size is determined based on average kinetic and potential energy values of inner and surface atoms values as well as the atomic arrangement of the NPs. It also provides justifications of the reasons behind agreement/disagreement between the results obtained here and the results obtained by previous theoretical models. Chapter six reports the molecular dynamics simulation results on the stability of 1 nm FCC truncated octahedral and larger Ag particles. Chapter seven reports the sintering kinetics of two NPs in size range of 4 nm to 20 nm and sintering of three and four NPs of 4 nm Ag nanoparticles. Finally, chapter eight reports the conclusion and suggests further research ideas that are related to this thesis.

2. LITERATURE REVIEW

This chapter is divided into four sections. The first provides the reader with a background on the development of the Ag NP pastes and their usage in electronic industry. Different factors that affect the strength of the joints such as bonding temperature and pressure, and size of NPs are discussed. The second section discusses melting theories, melting kinetics, and the role of defects in initiating the melting process. It also discusses surface premelting of both bulk and nanomaterials, and the resistance of different atomic planes to surface premelting. The third section provides a brief introduction on sintering stages and sintering mechanisms that contribute to sintering process of microparticles and nanoparticles. Section four reports the solid phases of NPs and discusses different factors that contribute to formation of the stable solid phases in NPs.

2.1 Ag Nanoparticle Paste for Electronic Packaging

2.1.1 From Micro Ag Flakes to Nano Ag

Ag micro flakes pastes have been used as a die attach material for power electronics packaging since the late 1980s [25]. The paste contained Ag micro flakes (about 15 µm in diameter) [26,27] and a solvent like terpineol [28], cyclohexanol [26,29], and butanol [30]. The main disadvantage of this method is the large amount of pressure needed to achieve the bonding (10-40 MPa) [25], which may damage the silicon die. It was possible to reduce the bonding pressure and temperature by using nano Ag paste as bonding material [11,12]. It has been shown that it is possible to bond two pieces of Cu through a sintered network of Ag NPs [31-34]. These bonds are formed by sintering of individual Ag NPs combined with sintering of these NPs onto

Cu surfaces. The sinterability between individual Ag NPs and the sinterability of the NPs onto the Cu surface determine the strength of the bond.

The weight percentage of the Ag NPs in the bonding paste was between 70% [35] to 80% [36]. In addition to the Ag NPs, the paste contained solvents, dispersant, and binders. Viscosity of the paste can be controlled by using different solvents. Binders and dispersants serve the same function of dispersing the NPs and both terms have been often used interchangeably in literature [37]. In addition to dispersing the NPs, binders prevent cracking of the paste during the heating process.

2.1.2 Bonding Temperature

Bonding temperature has a strong effect on the sintering behaviour of the paste and therefore on the mechanical strength of the joint. Based on Arrhenius equation, the diffusion process among the NPs and between the NPs and the substrate will be enhanced as the temperature is increased. Surface diffusion is dominant at low temperature while grain boundary diffusion and lattice diffusion need higher temperatures to be achieved [38]. For NPs that are coated with organic shells, it is important to heat the paste to the decomposition temperature of the organic shell in order to promote the bonding between the Ag NP paste and the substrate [7-9].

2.1.3 Bonding Time

In order to achieve bonding, it is important to allow enough time for the dispersant to oxidize and for the Ag NPs to sinter [37]. Similar to the temperature effect on Ag NPs coated with organic shells, it is important to allow enough time for the organic shell to decompose and promote sintering of the Ag NP paste [9]. Sintering of two particles starts by forming an initial point contact and surface diffusion starts at the early of stage of heating, which results in the formation of a neck and a grain boundary between the two particles. At later stages of heating, neck growth continues and grain boundary diffusion occurs. After a long enough time, the two particles coalesce and form one larger particle [38]. A study by Knoerr *et al.* [39] showed that by increasing the bonding time from 5 s to 60 s, the joint density has increased from 68% to 75%. As a result, the shear strength of the joint increased by 30%.

2.1.4 Bonding Pressure

Pressure enhances the sintering process by increasing the average number of contacts between the Ag NPs [39,40] and by closing the porosity at the joint. This increases the final density of the joint and therefore increases the joint strength. Fig. 2.1 shows that the shear strength values of Ag NP paste-Cu joints formed at 573 K have increased as the bonding pressure increased. Although pressureless sintering might be achieved, Lei *et al.* [40] found that a joint formed under a pressure of 5 MPa and a temperature of 548 K has a shear strength that is four times higher than the shear strength of a joint formed at the same temperature but with no bonding pressure. Contact formation between NPs during pressureless sintering is driven by van der Waals forces [41].

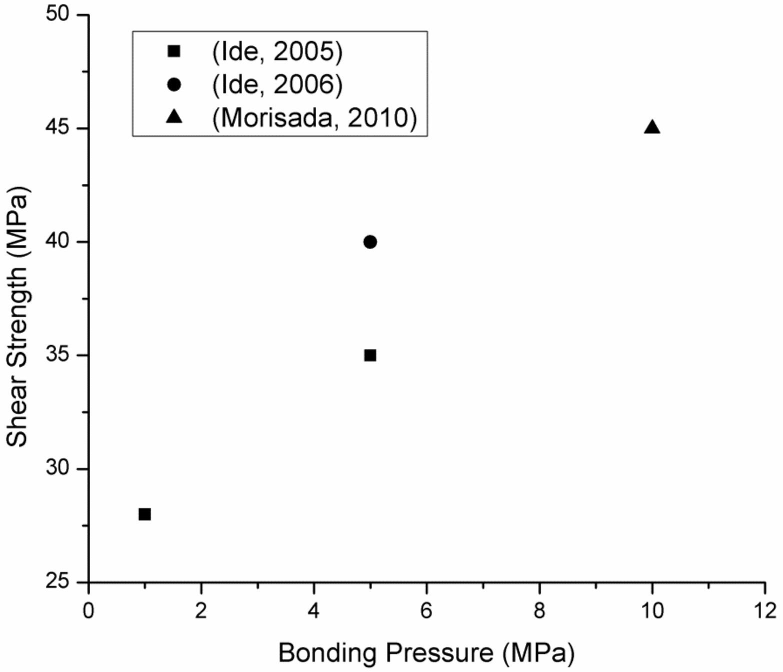

Fig. 2.1 Shear strength value of joints formed by Ag NPs paste at 573 K under different bonding pressure [9,13,35].

2.1.5 Size of Ag NPs

As will be discussed below in section 2.4.2, the driving force of sintering depends on the specific surface energy and surface curvature of the NPs. Both values increase as the size of the NPs decreases, this leads to denser joints and therefore higher shear strength values. It was found that the density of a joint formed using 30 nm Ag NPs is significantly higher than a joint formed by 100 nm NPs [42]. Siow [37] has compared in his review on Ag pastes the shear strength of joints formed by different sizes of Ag NPs and found out that using smaller NPs increased the shear strength of the joint. Fig. 2.2 shows shear strength values of Ag NPs-Cu joints formed with different sizes of Ag NPs at 573 K [37]. The figure shows that at equal sintering pressures, shear strength of the joints increased as the size of the NPs is decreased. The figure also shows that shear strength values of bonds formed by 11 nm particles is about six times larger than the shear strength of bonds formed by 100 nm Ag particles [37].

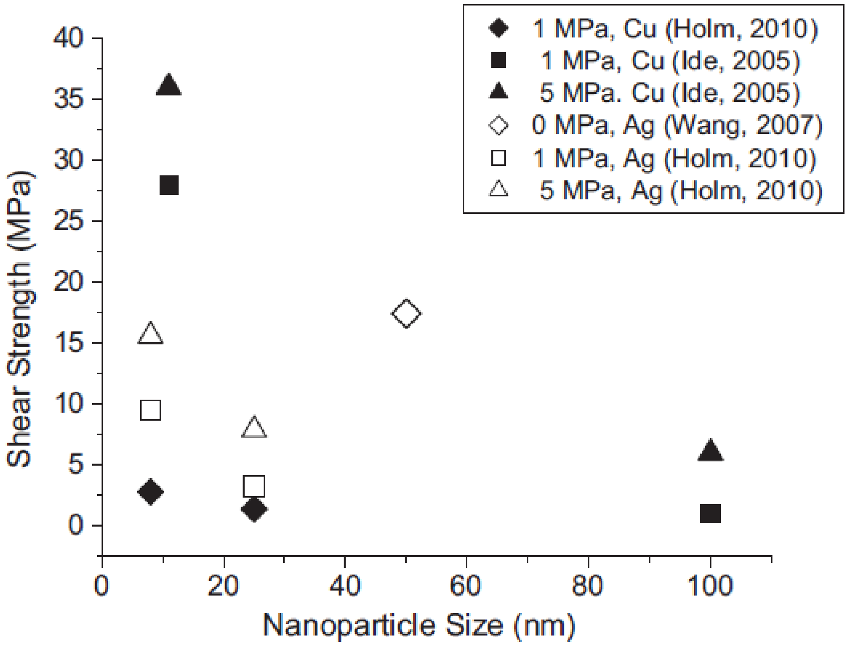

Fig. 2.2 Shear strength of Ag nanoparticles joints for bonding Ag or copper (Cu) substrates in ambient atmosphere for Ag nano-particle size ranging from 8 to 100 nm at sintering temperatures of 573 K [13,42,43]. Holm *et al.* used Ag nano-ink in their work [37].

Particles distribution and morphology might also have an effect on the joint properties [44,45]. These two factors change the initial density of the joint and therefore the final density of the joint will be affected. It was found that Ag NP paste that contains NPs with different sizes and morphologies had better sinterability and therefore stronger joints were achieved [44].

2.1.6 Bonding Substrate

Bare Cu is still the most favourable materials to be used as leadframe in electronic packaging [37]. Although most literature have used Cu as a substrate, Ag and Au plated substrates was also considered [37]. The main challenge with bonding Ag NPs to bare Cu substrate is oxidation of Cu. This effect can be reduced by applying a partial oxygen pressure of 0.08 atm during the bonding process to oxidize the dispersant and reduce the oxidation effect on the Cu substrate [46].

The problem of oxidation does not exist when Ag and Au plated substrate are used and stronger joints can be formed. It is expected that Ag NPs form the strongest bonds with Ag plated substrates due to the similar chemistry and the equal lattice parameter between the particles and the substrates. For Au plated substrates, a quasi-epitaxial match between the Ag NPs and the substrate was achieved [7,47]. This is due to the small difference between the lattice parameters of Au (0.4079 nm) and Ag (0.4086) [7]. The lattice parameter of Cu is much less (0.3615 nm) and therefore higher energy (temperature) is needed to from the bond. . It was suggested that the difference in lattice parameters between Ag and Cu is responsible for forming a distorted layer of about 3 nm thickness [7,8,13]. Ni was also used as a substrate but the mechanical strength of the bond was 50% less than joints formed on Cu substrate [9]. Bonds that are formed on Al and Ti substrates have even lower strength values than Ni, this is due to the stable oxide layer that could not be removed by the oxidation of the dispersant [9].

2.2 Melting and Surface Premelting

2.2.1 Melting Theories of Bulk Materials

In 1891, Sutherland [48] suggested that melting occurs when the distances between atoms exceeds a certain value relative to the atomic diameter. As a result of increasing distances between atoms as the temperature increases, shear modulus of the solid also decreases. A relationship between the temperature of the solid and the shear strength (G) was proposed in equation 2.1 [48]. The shear modulus reaches zero at T_m and the rigidity of the metal vanishes.

$$G = G_o\left(1 - \frac{T}{T_m}\right) \qquad (2.1)$$

where G_o is shear modulus at 0 K and T is the temperature.

In 1910, Lindemann [24] advanced Sutherland idea and suggested that melting occur when the amplitude of atomic vibration exceeds a certain fraction of interatomic distance, this causes collisions between atoms and therefore destabilise the lattice. Gilvarry [49] further advanced Lindemann's model and suggested that melting occurs when the root mean square displacement (rmsd) exceed a certain fraction of the nearest neighbour-separation. Currently, Gilvarry definition of melting is the most accepted form of Lindemann's criterion.

In 1938, Brillouin [50] has also advanced Sutherland work on the relationship between shear strength and melting and suggested that as T_m is approached, macroscopic rigidity disappears while microscopic rigidity remains finite. He considered the anisotropy of solids and suggested that some rigidity coefficients might remain finite at T_m. One year later, Born [51] developed his criteria of melting, which suggested that melting of a crystal occurs when one of the shear modulus vanishes. Another proposed melting model is thermoelastic instability criterion, which was developed by Herzfeld and Goeppert-Mayer (HGM) [52] in 1934 and suggested that melting is caused by thermoelastic instability of the material. It was also suggested that isothermal compressibility diverges as the temperature of the solid reaches T_m [52].

It has been shown that melting occurs when vacancies in the solid show a dramatic increase [53,54]. It was found that the concentration of vacancies in many metals increased from 0.37% at the beginning of melting to 10% [55]. The increase of electrical resistivity at T_m is an indication of the increase in the concentration of vacancies [56]. However, this model failed to explain the mechanism of melting and why and how the vacancies concentration increased from 0.37% to 10% at T_m.

2.2.2 Premelting at Defects:

It has been shown the melting process starts below T_m at defects such as vacancies, interstitials, dislocations, and grain boundaries [20]. This is because the atoms at defects vibrate more freely than other atoms due to their lower coordination number [57,58]. It has been shown that it is possible for a prefect crystal lattice with no defects to be superheated to a temperature higher than T_m before melting occurs [59].

Fig. 2.3 shows an example of premelting at a grain boundary and at a dislocation in a colloidal crystal with T_m of 28.3^o C [60]. The crystal in Fig. 2.3(a) shows a grain boundary separating two crystallites with a relative tilting angle of 13^o and cuts the crystal into two different planes as shown by the yellow line. The dashed line shows a partial dislocation. As the temperature of the crystal increased from 27.2^o C to 28^o C, an amorphous layer started to form at the grain boundary region as an indication of premelting. As the temperature increased to 28.1^o C (Fig. 2.3(c)), premelting at the partial dislocation took place. The melted layer thickness increased as the temperature of the crystal increased to 28.2^o C (Fig. 2.3(d)).

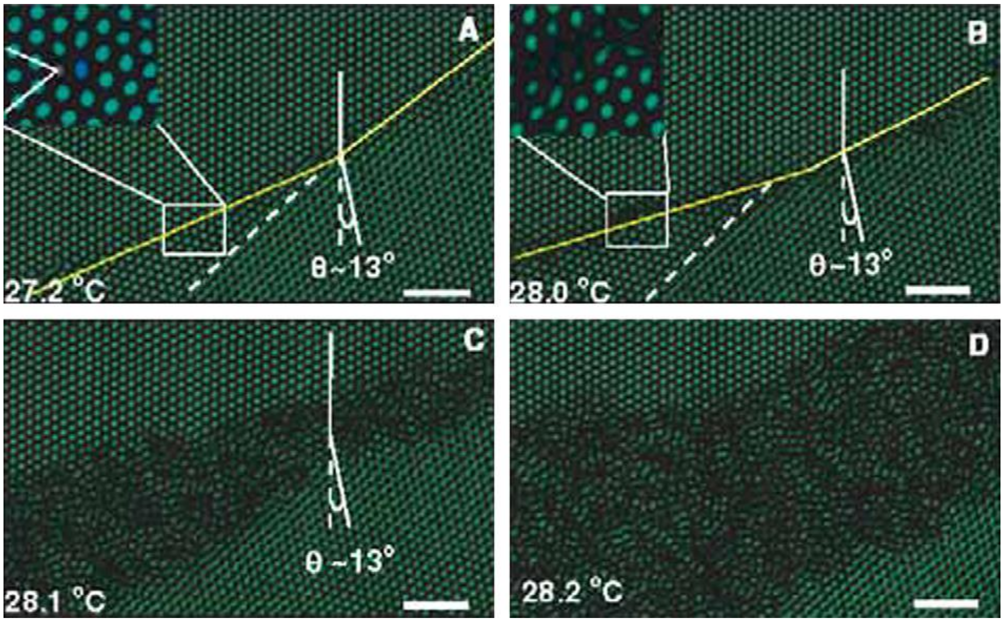

Fig. 2.3 Premelting of the colloidal crystal at a grain boundary [60]. The length of scale bars is 5 µm .

Fig. 2.4 shows Lindmann parameter (δ_L) values at 28.1^o C for atoms near and far away from different type of defects such as a melted boundary, a partial dislocation and a vacancy [60]. δ_L is calculated by dividing rmsd value of the atom by the distance between the atom and the nearest neighbor [20]. It can be seen from Fig 2.4 that δ_L values increased exponentially for atoms near the defects. This confirms that melting started at defects. It can also be seen in the figure that δ_L values near the melted boundary shows the highest values, middle values near the partial dislocation, and smallest values near the vacancy. This is because δ_L is higher at defects with higher interfacial energies.

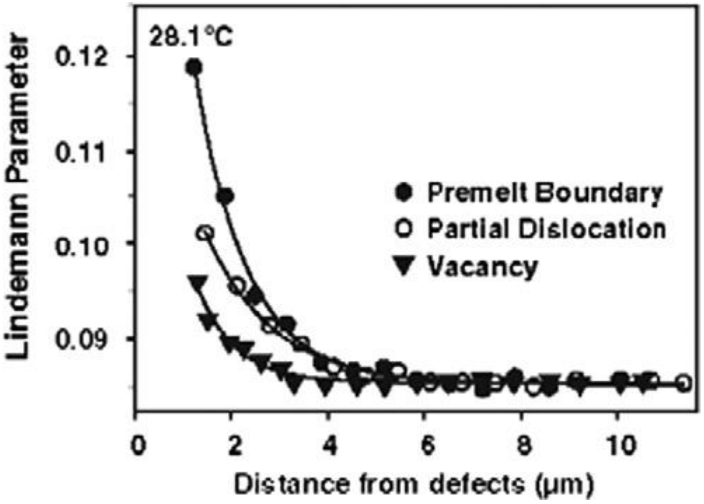

Fig. 2.4 The local Lindemann parameter as a function of distance from a vacancy, a partial dislocation, and a melt front. Within 1 μm of the defects, the particle motion was too rapid and calculation of Lindemann parameter was unreliable [60].

2.2.3 Surface Premelting of Bulk Materials

Faraday [61] has made the first observation of surface premleting of ice during the 19 century. Surface premelting of metals was then observed by different experimental techniques such as electron diffraction (ED), [62,63], X-ray reflectivity [64], and low energy ion scattering spectroscopy (LEIS) [65,66]. As shown in equation (2.2), the energetic requirement for surface premelting to occur is that the solid-vapour interfacial energy (γ_{sv}) should be larger than the sum of solid-liquid interfacial energy (γ_{sl}) and the liquid-vapour interfacial energy (γ_{lv}) [67]. Fig, 2.5 shows the process of formation of a liquid layer on a solid surface and the different interfacial energies associated with it.

$$\gamma_{sv} > \gamma_{sl} + \gamma_{lv} \qquad (2.2)$$

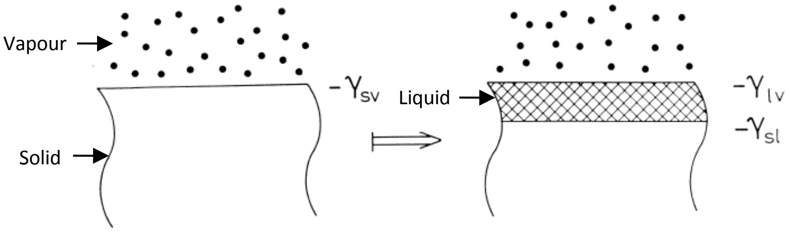

Fig. 2.5 A schematic diagram of surface premelting.

Surface premelting starts by forming a quasi-liquid layer on the solid surface below T_m [20]. This layer expands and transforms at T_m into a liquid layer that is thick enough to be considered as liquid (several atomic layers) [68]. The quasi-liquid layer has intermediate structural, dynamic, and transport properties between solid and liquid [69]. The liquid layer expands to the solid core to complete the melting process [68].

Resistance to surface premelting varies among different atomic planes due to the variation in their packing densities [20]. For FCC metals, plane (110) exhibited complete surface premelting for Ni [70], Cu [71], Al [72], In [73], and Au [74]. Denser (100) planes of FCC metals such as Au [75], Ni [76], and Pb [77] showed non complete surface premelting, i.e. the thickness of the quasi-liquid layer did not increase as the temperature approach T_m. Closed packed (111) planes of many FCC materials showed no surface premelting below T_m [66, 78-81]. Jin [82] has performed an MD simulation to find mean square displacement (msd) values of an Al (110) surface. The study showed that surface atoms vibrate with different amplitudes in different directions. Fig 2.6 shows the crystal structure of an FCC (110) surface with Z direction perpendicular to it. The most outer layer of the surface is numbered as 1. Fig. 2.7(a) shows msd components of Al (110) surface atoms at the three outer most layers and the bulk at 700 K, which is less than T_{sm}. The figure shows that x and y components of msd values (parallel to the surface) are largest at the outer most layer. This indicates that atoms at the outer most layer has easier channels to vibrate in x and y directions than inner layers. On the other hand, the second layer shows higher msd values in z direction (perpendicular to the surface) than the outer most layer. This also indicates another easy channel for atoms at the second layer to vibrate in z direction, which allows these atoms to pop out of the surface and create vacancies. This is can be further eased by cooperative high amplitude vibration of the outer most layer in x and y directions. Surface premelting starts when the concentration of vacancies at the surface becomes sufficiently large. Fig. 2.7 (a) also shows that msd values of the atoms in third layer almost reached the bulk values in all directions.

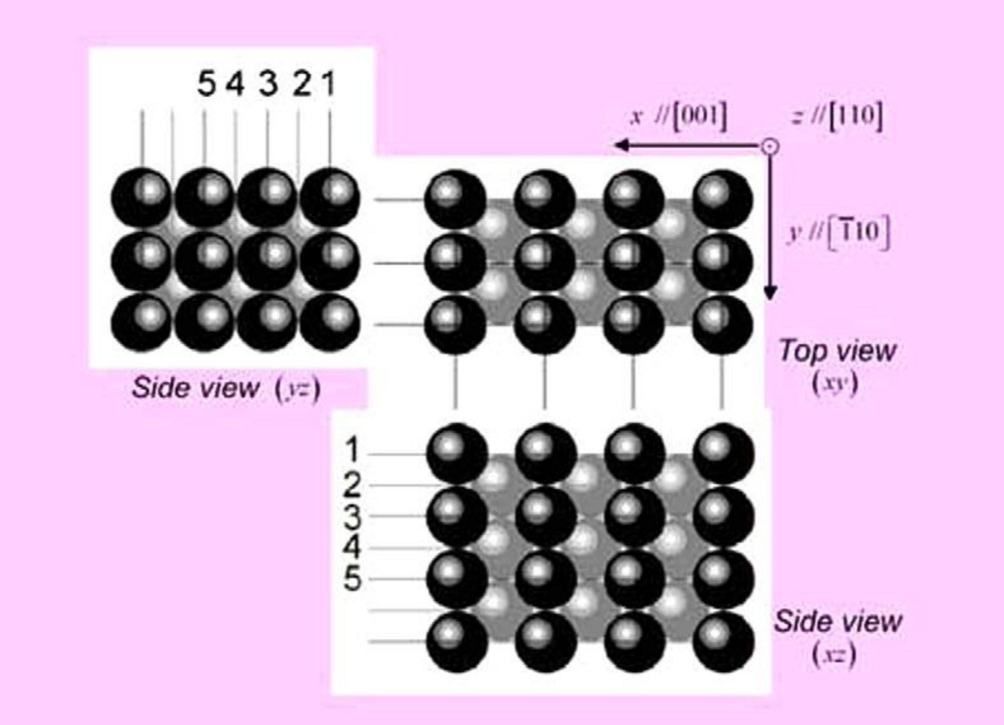

Fig. 2.6 The geometry of FCC (110) surface. The reference directions are indicated in the 3D projected views. Five layers normal to the surface are marked as 1–5, with 1 being the top surface layer [82].

Fig. 2.7 (b) shows msd values of atoms vibrating inside the easy channels indicated above increase dramatically as the temperature increase. This is different than msd values of bulk atoms, which increase linearly with temperature. These results agree with experimental results obtained by LEIS and showed in Fig 2.7 (c) [83]. The figure shows a linear relationship between temperature and msd values below 700 K. Similar to the results shown at Fig. 2.7 (b), a dramatic increase of the msd occurs above 700 K. This was attributed to the anharmonic effect of atomic vibration inside these easy channels at temperatures higher than 700 K.

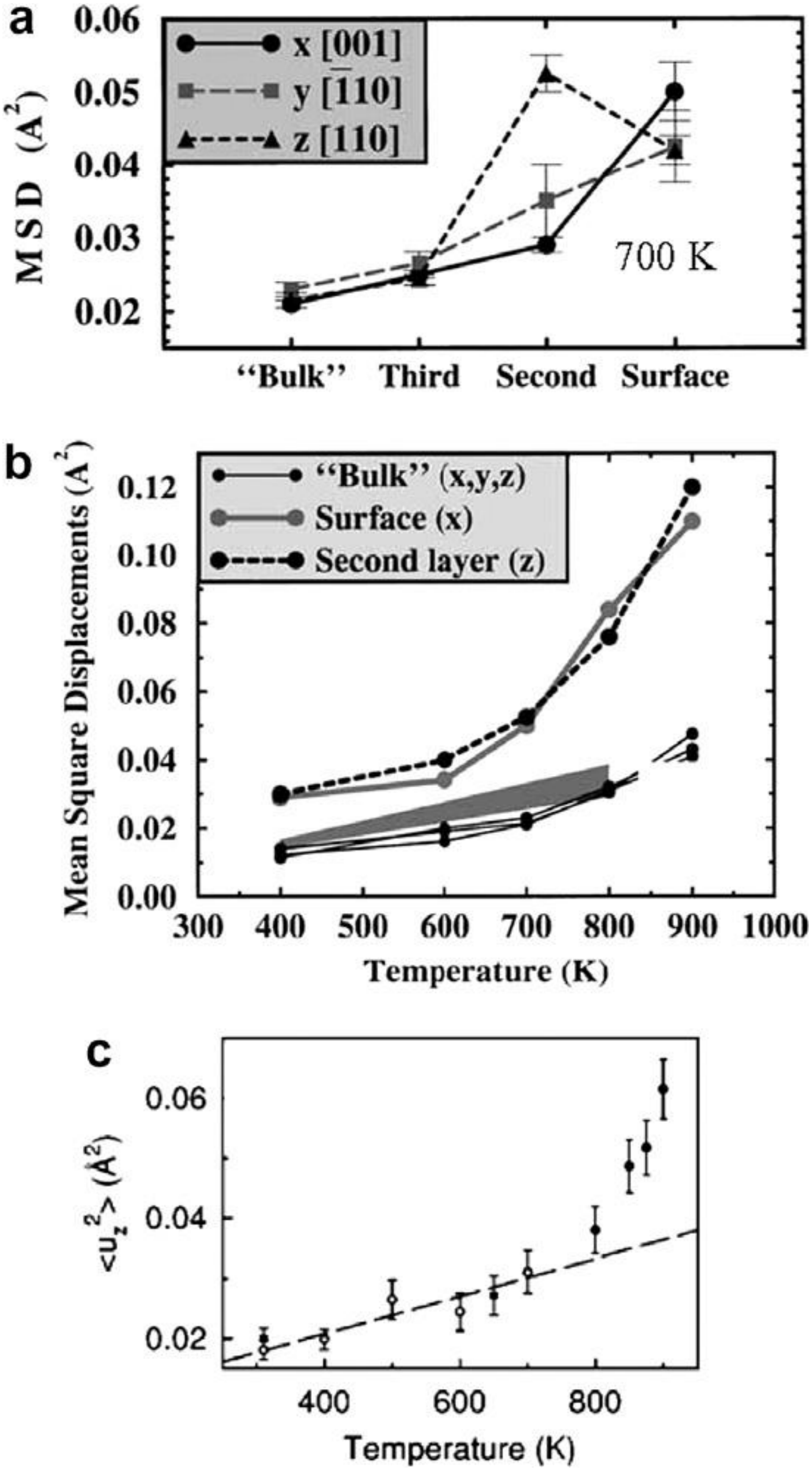

Fig. 2.7 Layer-resolved MSDs as a function of temperature ('bulk' refers to the two inner layers). The shaded area in (b) corresponds to the bulk experimental values. The data by neutral impact collision ion scattering spectroscopy measurements are shown in (c): circles and squares refer to measurements along the <001> and <1$\bar{1}$0> directions, respectively. The dashed line is the linear regression for the open circles [82,83].

2.2.4 Melting of Nanomaterials:

In addition to the theoretical models [21-23] that predicted melting point depression of NPs (see section 1.1), many experimental techniques have confirmed the depression of T_m at the nanoscale. Electron diffraction (ED) has been used to determine T_m of thin films of (Pb, Sn and Bi) [84], In [85], and Sn [86], and NPs of (In, Pb) [87], Sn [68], and Au [88]. T_m was determined at the temperature at which diffraction patterns changes from rings to halos. In situ electron microscopy was also used to determine T_m of NPs at the temperature at which the image is greatly dims in dark field mode or at the temperature at which the facets of a NP disappear in the bright field mode. The former method was used to study melting of (Sn, In, Pb, and Bi) [14], In [89], and Sn [90], while the later was used to study melting of Bi [91]. Other experimental methods such as nanocalorimetry, X-ray diffratction (XRD), and differential scanning calorimetry (DSC) were used to study melting of Sn [92], Pb [93,94], and Al [95,96], respectively.

As shown in Fig. 2.8, T_m values of Sn, In, Bi, and Pb NPs show a linear relation with inverse radius of the NP [14]. Fig. 2.9 shows that T_m of Au decreased dramatically for NPs smaller than 10 nm in radius [88]. Although all these experiments confirmed the depression of T_m of nano materials, the obtained T_m values were scattered even for similar materials and sizes. This was due to the effect of defects such as grain boundaries and dislocations on T_m [20]. The material of the mounting substrate might also have an effect on T_m of the NPs [21].

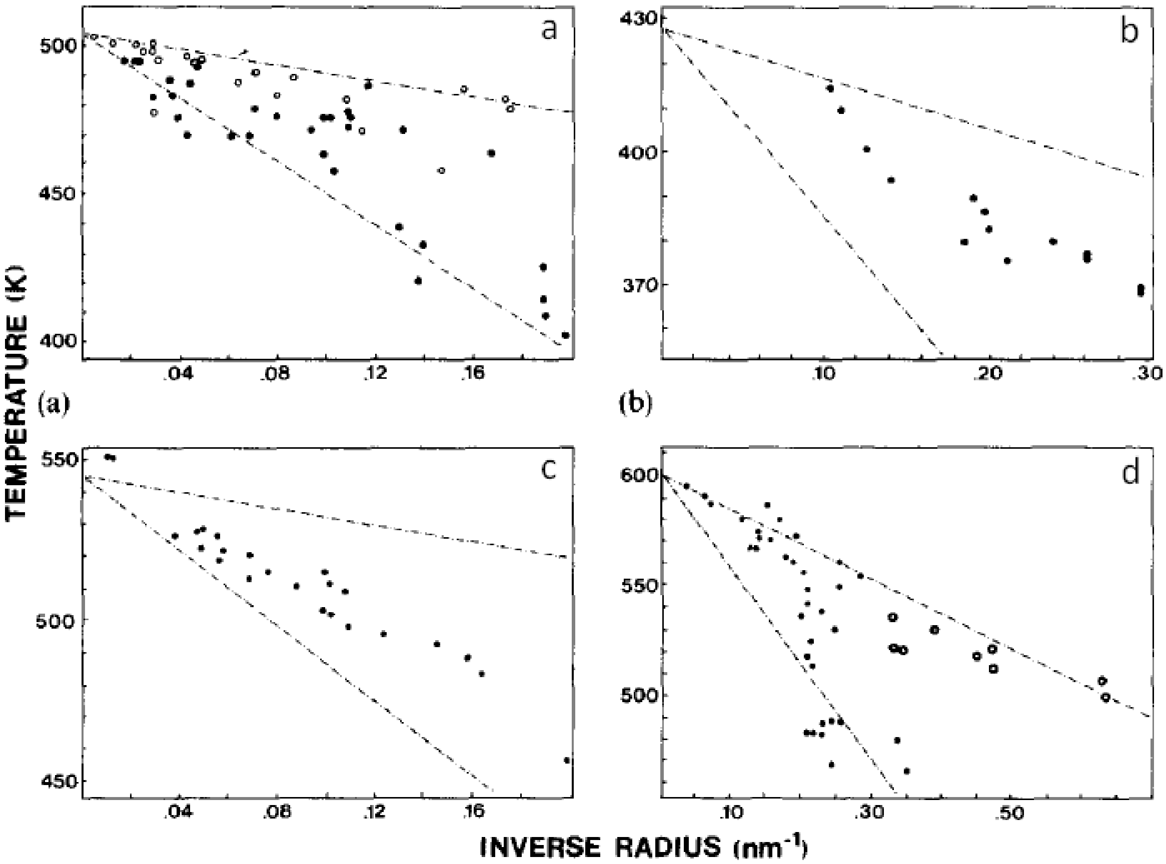

Fig. 2.8 Plots of melting temperatures vs the reciprocal of the particle radius for (a) tin, (b) indium, (c) bismuth and (d) lead. The broken lines represent the predicted lower and upper bounds. The experimental data are represented by circles with the open circles denoting data taken under more contaminated conditions than those represented by full circles, e.g. the open circles in (a) correspond to a second melting of tin particles and in (d) to lead particles under a higher ambient pressure [14].

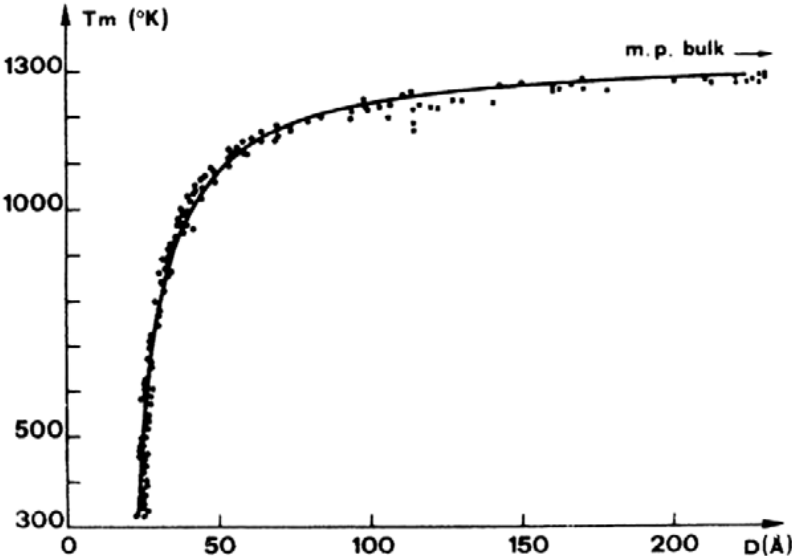

Fig. 2.9 Melting point of Au ultrafine particles as a function of particle size determined by means of scanning electron-diffraction method [88].

2.2.5 Surface Premelting of Nanoparticles:

Similar to bulk materials, surface premelting was also experimentally confirmed for nano-sized materials such Sn NPs [92,97], and Pb [94], and Pt nanocrystals [98], and was also numerically confirmed for Au NPs [99], and Ni nanoclusters [100]. The finite curvature of NPs has an effect on the thickness of the liquid layer [101]. It was found that liquid layers formed on NPs are thicker than those formed on bulk material and may reach half of the particle radius. Fig 2.10 shows SEM image of Sn NPs with different sizes at about 10 K below T_m. The white rings are stable liquid layers covering the solid core. It can be seen that smaller particles were fully melted without passing the surface premelting stage [101].

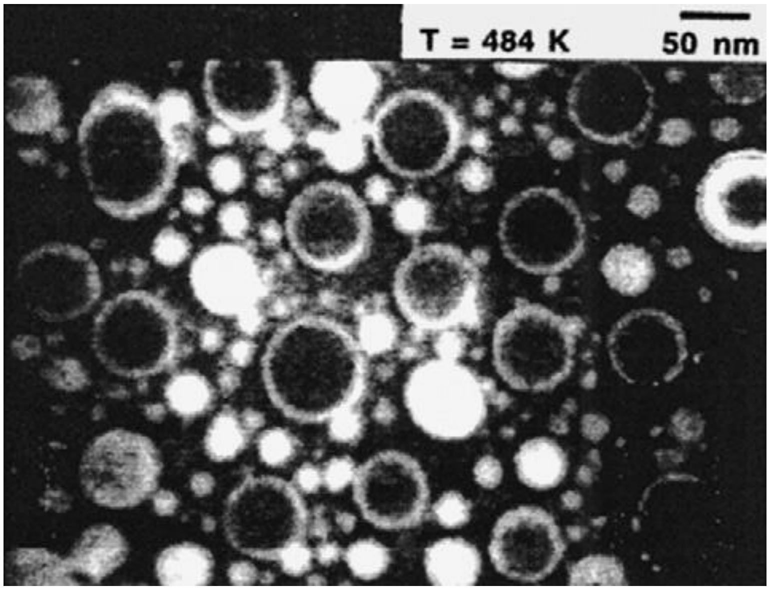

Fig. 2.10 Dark field TEM image for Sn clusters on SiO_2. A stable surface liquid layer is observed for large clusters with a bright ring around a dark core. Smaller (white) clusters are melted entirely [101].

An analytical model was recently developed by Chernyshev to determine the onset temperature of surface premelting (T_{sm}) for NPs in terms of the mean-field approximation [102]. Chernyshev developed the model based on Shi's model [22] and has shown that surface premelting does not take place if the NP radius is smaller than a critical radius r_c, which is different for different materials. Instead, the surface layer makes a transition to a pseudo-crystalline state before the whole particle melts [103].

2.3 Solid State Phases of Metallic Nanoparticles

2.3.1 Atomic Structure of Solid Phases in Metallic Nanoparticles

Unlike bulk materials, metallic NPs may exist in non-crystalline solid phases arranged in icosahedral or decahedral configurations [104-105]. Fig. 2.11 shows atomic arrangement of the most stable solid phases of metallic NPs [106]. Icosahedral structure has only (111) closed pack facets and is formed by 20 tetrahedral sharing a vertex at a fivefold symmetry axis. This structure has less surface energy than other solid configurations but on the expenses of the large internal strain caused by the 20 distorted tetrahedral, which make this structure energetically unfavorable for large NPs. Decahedral structure is less spherical with less internal strain and is formed by five tetrahedral sharing one edge with (111) and (100) facets. FCC truncated octahedral structure has (111) and wide (100) facets, which increase the surface energy with no internal strain. This makes this configuration the most stable for large NP, at which surface energy is reduced due to the decrease in the surface curvature.

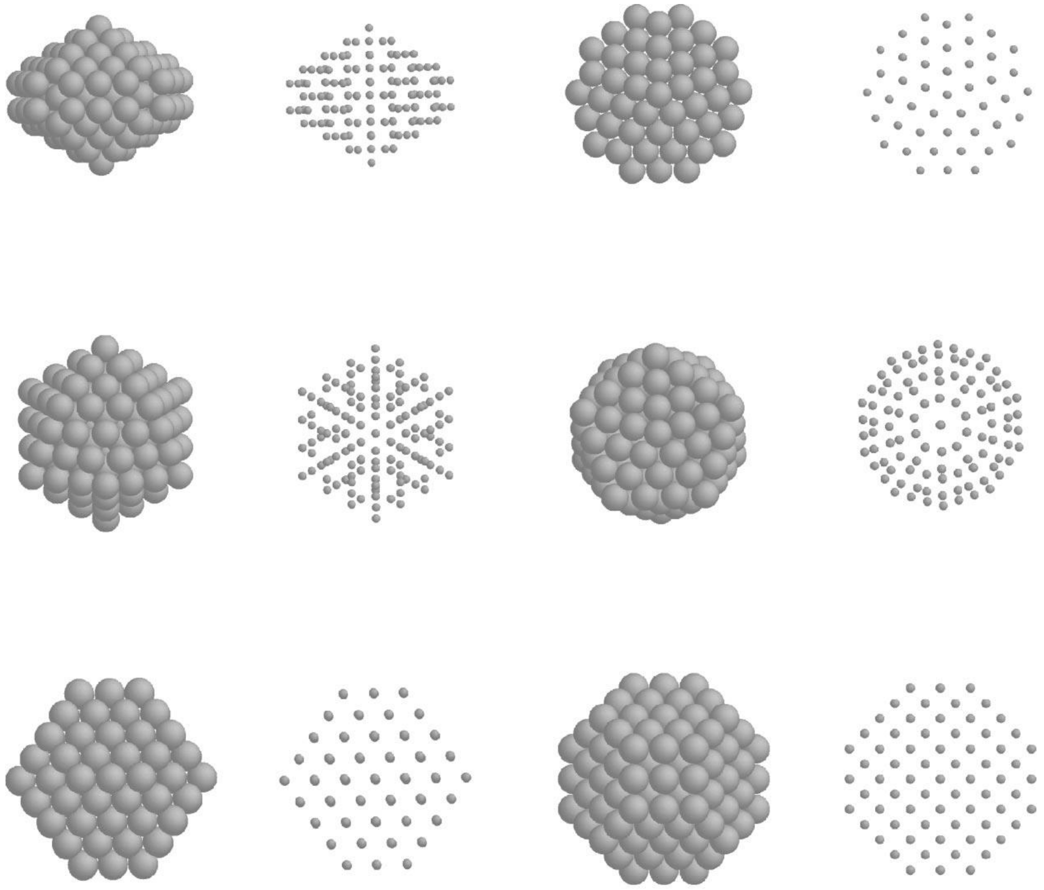

Fig. 2.11 Decahedral (top row), icosahedral (middle row), and fcc truncated octahedral structures (bottom row). Each structure is shown in side (first two columns of the figure) and top views (third and fourth columns), and each view is given in two representations [106].

2.3.2 Stability of Solid Phases in Metallic Nanoparticles

It has become possible by MD simulation to find the most stable configuration by either depositing the atoms on a very small particle (seed) at a specific temperature [107] or by freezing a liquid nanodroplet [108-112]. Fig. 2.12 shows Ag NPs solid structures obtained by freezing different sizes of Ag nanodroplets with specific magic numbers [112]. Magic number is the number of atoms that would form high symmetrical structure of a certain configuration [113]. As it can be seen in the figure, nano-droplets of 147 and 309 atoms solidified in icosahedral structures. The frozen structure became decahedra and then FCC polyhedron as the size of the nanodroplet increases. A parameter (Δ) was introduced and defined as the ratio of the excess energy caused by the surface and the internal strain to $N^{2/3}$, where N is number of atoms in the NP. Fig. 2.13 shows the values of Δ for different sizes of Ag NPs with different icosahedral, decahedral, and FCC truncated octahedral configurations [114]. The figure clearly shows that the minimum energy values of the small particles are associated with the icosahedral configuration, decahedral has minimum energy values for intermediate size of Ag NPs, which suggests that the formation of the stable phases obtained in Fig. 2.12 is mainly driven by minimization of the excessive energy. It was also generally agreed based on the ground state energy of a NP that the icosahedral configuration is the most stable phase for small NPs, decahedra is stable for intermediate size, and the FCC structures is the stable configuration for larger NPs [115-116]. Nevertheless, other studies have shown that the stable solid configuration might deviate from the minimal energy values due to thermal and kinetic effects [117]. For example, icosahedral structures of large Fe [118], Au [119], and Ag [120,121] nanoparticles were fabricated by different experimental methods. Fig. 2.14 shows TEM images of Ag NPs synthesized in a kinetically controlled polyol process that allows the formation of multiple twinned icosahedral Ag NPs that are larger than multiple twinned decahedral particles and single crystal truncated octahedral particle [122].

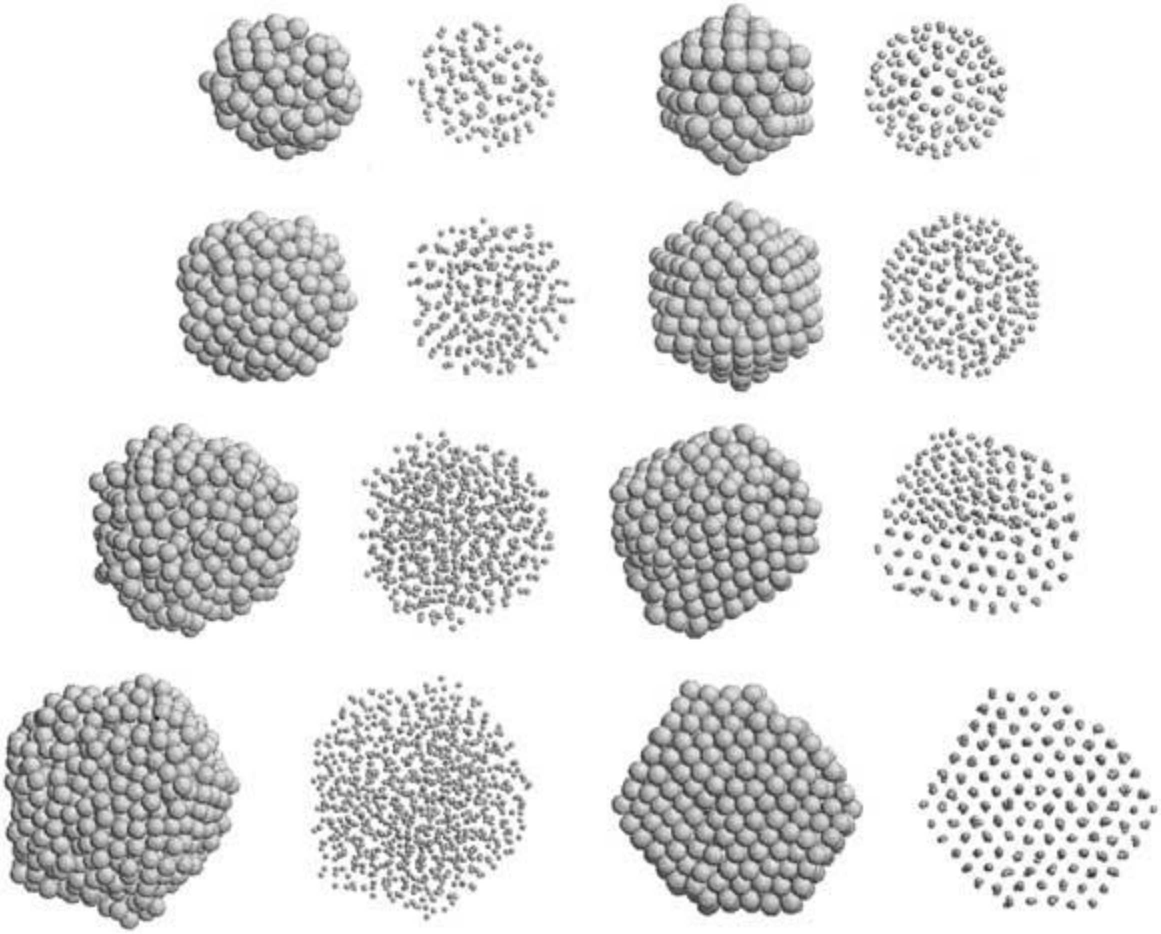

Fig. 2.12 On the left, Baletto et. al. reported the initial configurations of silver nanodroplets at magic icosahedral numbers (147, 309, 561 and 923), while on the right, there are typical final structures obtained cooling at 1 K/ns: from top to bottom, icosahedra at 147 and 309, a decahedron at 561 (strongly asymmetric and with an island on hcp stacking above) and a fcc polyhedron at 923 [112] .

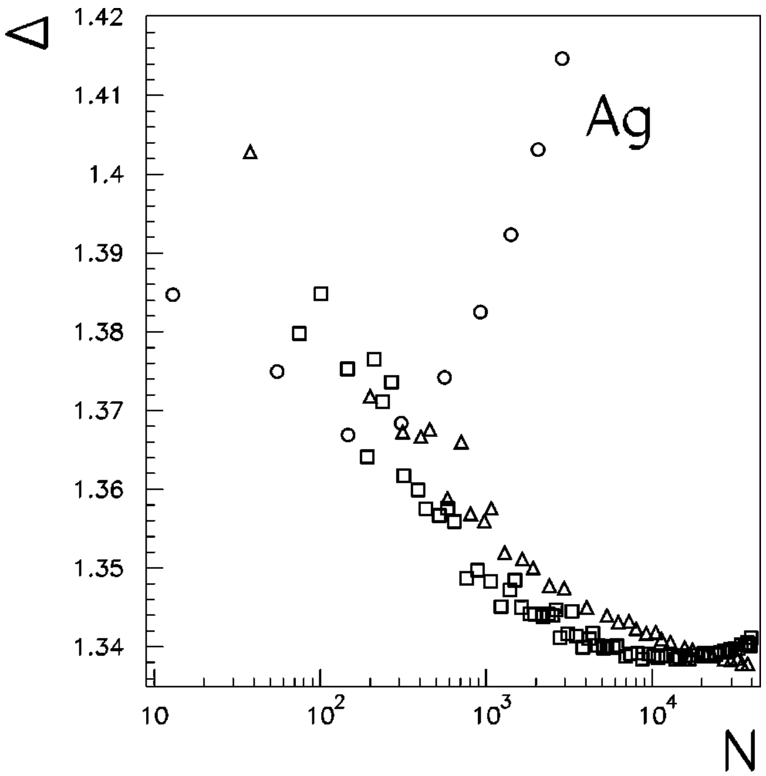

Fig. 2.13 The quantity Δ=$(E_{tot}$-$NE_{coh})/N^{2/3}$ as a function of the size N, calculated by means of Rosato, Guillope`, and, Legrand (RGL) potentials for silver clusters. Circles, squares, and triangles refer to icosahedra, decahedra, and truncated octahedra, respectively [114].

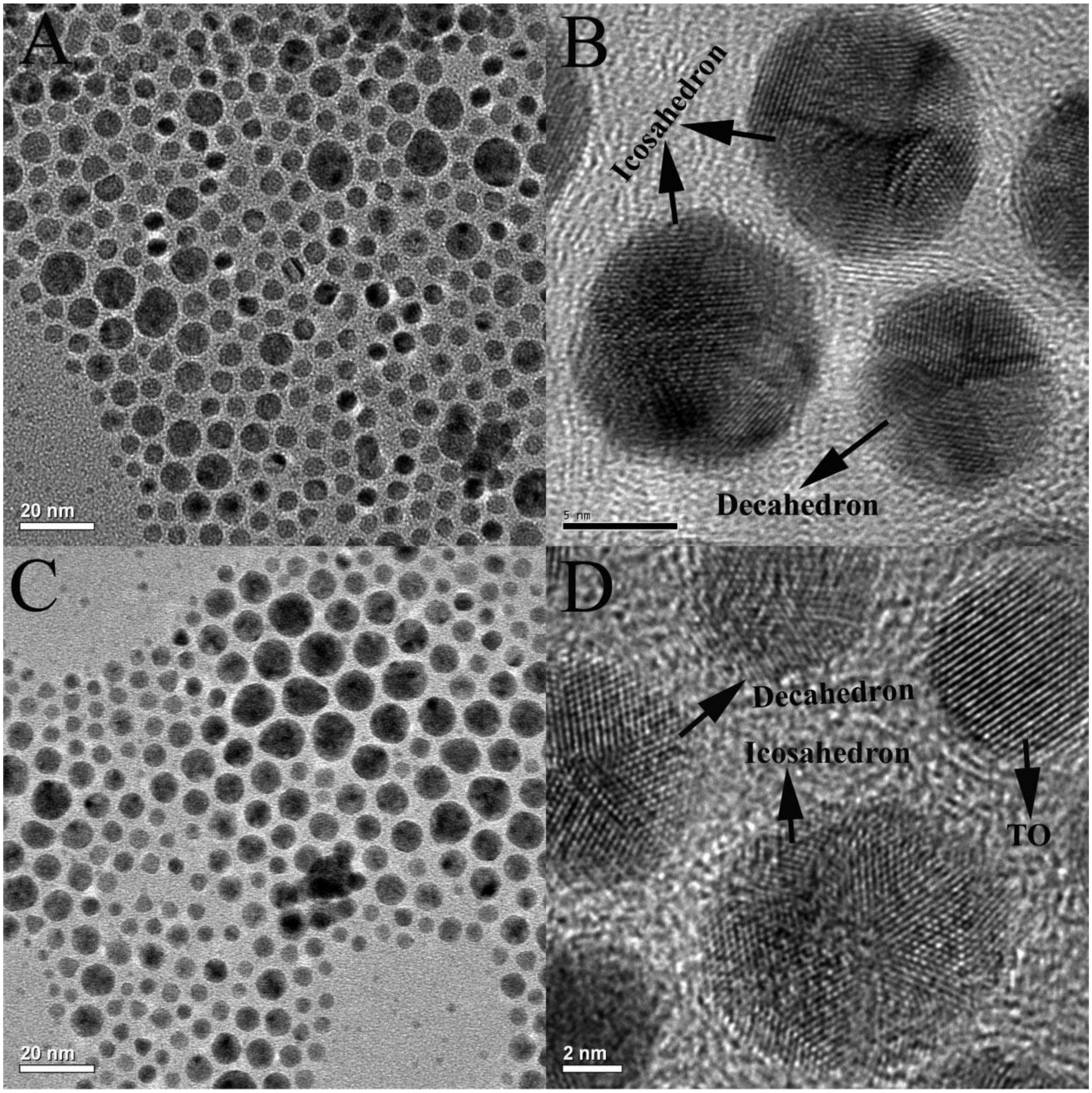

Figure 2.14 (A) TEM image of the mixture of icosahedral and decahedral Ag multiple twinned particles (MTPs). (B) HRTEM image of the mixture of icosahedral and decahedral Ag MTPs. (C) TEM image of the mixture of icosahedral and decahedral Ag MTPs and single-crystalline truncated octahedral nanoparticles. (D) HRTEM image of the mixture of icosahedral and decahedral Ag MTPs and single crystalline truncated octahedral nanoparticles [122].

2.3.3 Solid to Solid Phase Transitions in Metallic Nanoparticles

Solid to solid phase transition between different phases of NPs has been observed in many studies [123-129]. A multiple twinned Ag NP of 2.4 nm was transformed into an epitaxial FCC during annealing below the melting point [125]. Decahedra to Icosahedra transition was observed during in-situ TEM cooling of Au NPs smaller than 10 nm [126]. Valkealahti and Manninen [127] reported a non-diffusive transition of cuboctahedral Cu NPs with less than 2000 atoms to Icosahedral structure at 0 K. Koga et al. [128] proposed a cooperative slip dislocation mechanism for the transition of Icosahedral Au NPs to decahedral configuration just below T_{m}. Fig. 2.15 shows a recent MD study on phase transition of a Cu NP from cuboctahedra to icosahedra by a dislocation free shear wave at 700 K [129]. These transitions occurred in different conditions and by different mechanisms and have been driven by different energetic, thermal, and kinetics factors [129].

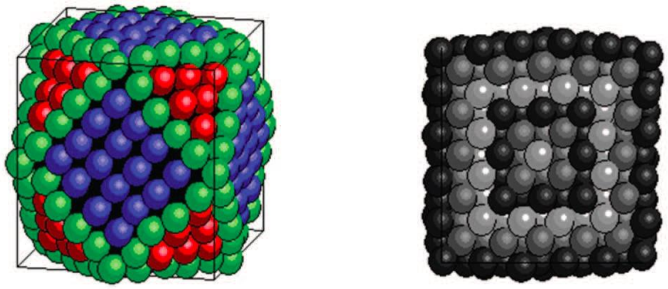

(a)t=0.0ps

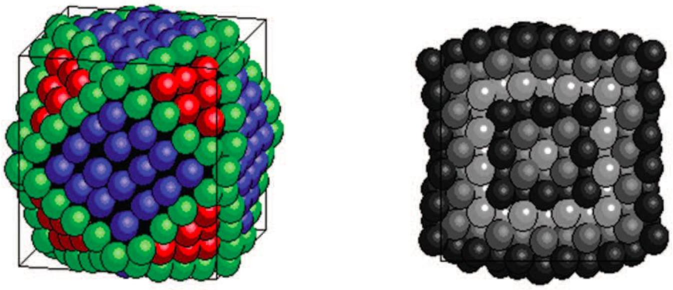

(b)t=4.0ps

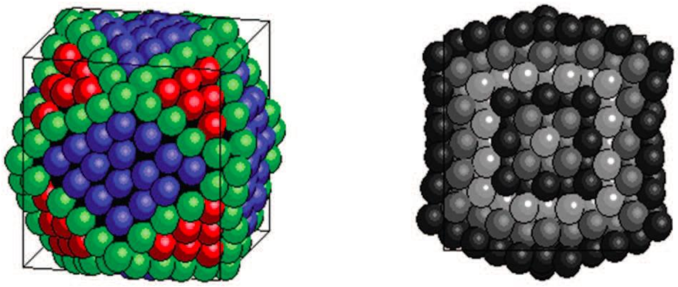

(c)t=5.0ps

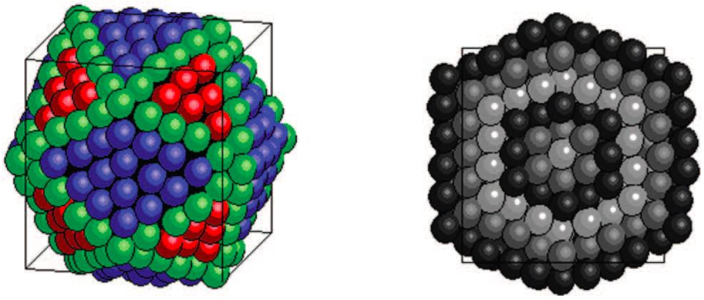

(d)t=10.0ps

Fig 2.15. The shape evolution of Cu cuboctahedral nanoparticles with 561 atoms at 700 K. The atoms initially on (100) surfaces, (111) surfaces, and edges are marked in blue, red, and green, respectively. For the cross-sections of the particles, atoms belonging to each shell layer in the initial cuboctahedron are denoted by different shades of gray. Time is specified below each snapshot: (a) t = 0.0 ps, (b) t = 4.0 ps, (c) t = 5.0 ps, (d) t = 10.0 ps. Time zero indicates when the transition begins [129].

2.4 Sintering of Microparticles and Nanoparticles

2.4.1 Sintering of Microparticles

Fundamental understanding of sintering of microparticles is of a great advantage for the development of powder processing and technology [130]. Traditionally, sintering is characterized by three stages shown in Fig. 2.16 [38]. The first is neck formation between two particles followed by a rapid increase in the neck radius. The second is gradual increase in the neck radius and the third is densification of the structure. The driving mechanism of sintering varies between viscous flow [131], evaporation condensation [132,133], surface diffusion [134], lattice diffusion [135], grain boundary diffusion [136,137], and plastic deformation [138,139]. Although sintering is a solid state process, liquid phase sintering has been applied to enhance the sintering by performing it in a liquid matrix [140-143]. Pressure also could be applied to assist the sintering process and enhance the diffusivity between the particles [144-146]. Based on the sintering mechanism, different theoretical models have been proposed to measure the rate of sintering, which is measured by the densification rate, the growth of neck radius to particle radius ratio (x/r), and shrinkage ($[4r-L]/4r$), [38]. As shown in the schematic in Fig. 2.17, r is the particle radius, x is the radius of the formed neck, and L is the final length of sintered NPs.

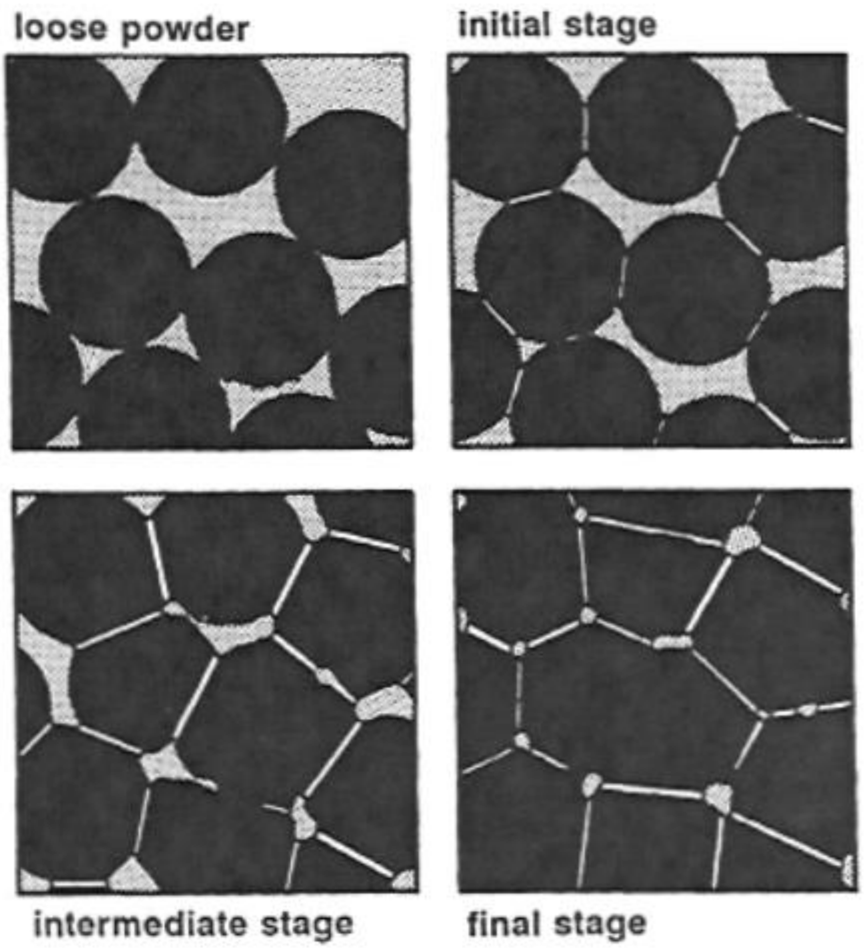

Fig. 2.16 Sintering stages starting with a loose powder and subsequently being sintered in each of the three stages. The initial open pore structure and high porosity are consumed by interarticle neck growth, grain growth, and pore shrinkage, with eventual formation of closed, spherical pores in the final stage [38]

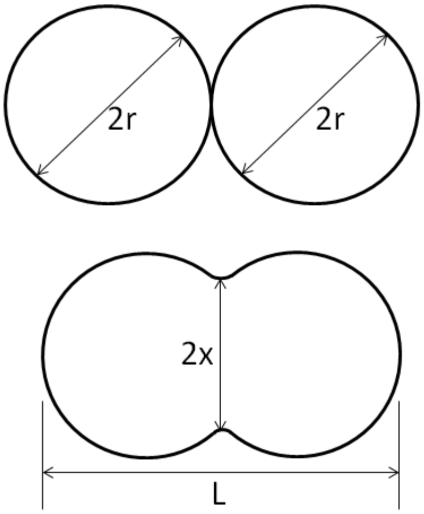

Fig. 2.17 Geometrical parameters of two particles during the sintering process.

2.4.2 Sintering of Nanoparticles

Sintering of NPs was performed numerically on Au (147, 148), Cu (148,149), Ni (150), and experimentally on Ag [151-154], and ZrO_2 [155]. These studies showed enhanced sintering rates at much lower temperatures than sintering of microparticles. Fig. 2.18 shows the atomic plots of 4.8 nm Cu NPs sintered at 50 K by molecular dynamics simulation [156]. As shown in the figure, the NPs rotated during the sintering process to align the atomic planes of the two NPs with each other and hence reducing the interfacial energy [156]. Full densification of seven 2.4 nm nanocylinders positioned in closed pack configuration at 300 K is shown in Fig. 2.19 [156]. Fig. 2.20 shows two Ag clusters of 55 atoms sintered at 0.001 K by Monte Carlo simulation [157]. In these studies, the reasons of the enhanced sintering of the NPs was attributed to the large driving force of sintering, which is caused by high curvature of the NPs surfaces, mechanical rotation, and the significant increase in diffusion coefficients at the nano-scale. Because of these factors, theoretical models used to estimate sintering kinetics of microparticles may not be valid for NPs sintering and therefore molecular dynamics simulation becomes of a great advantage here.

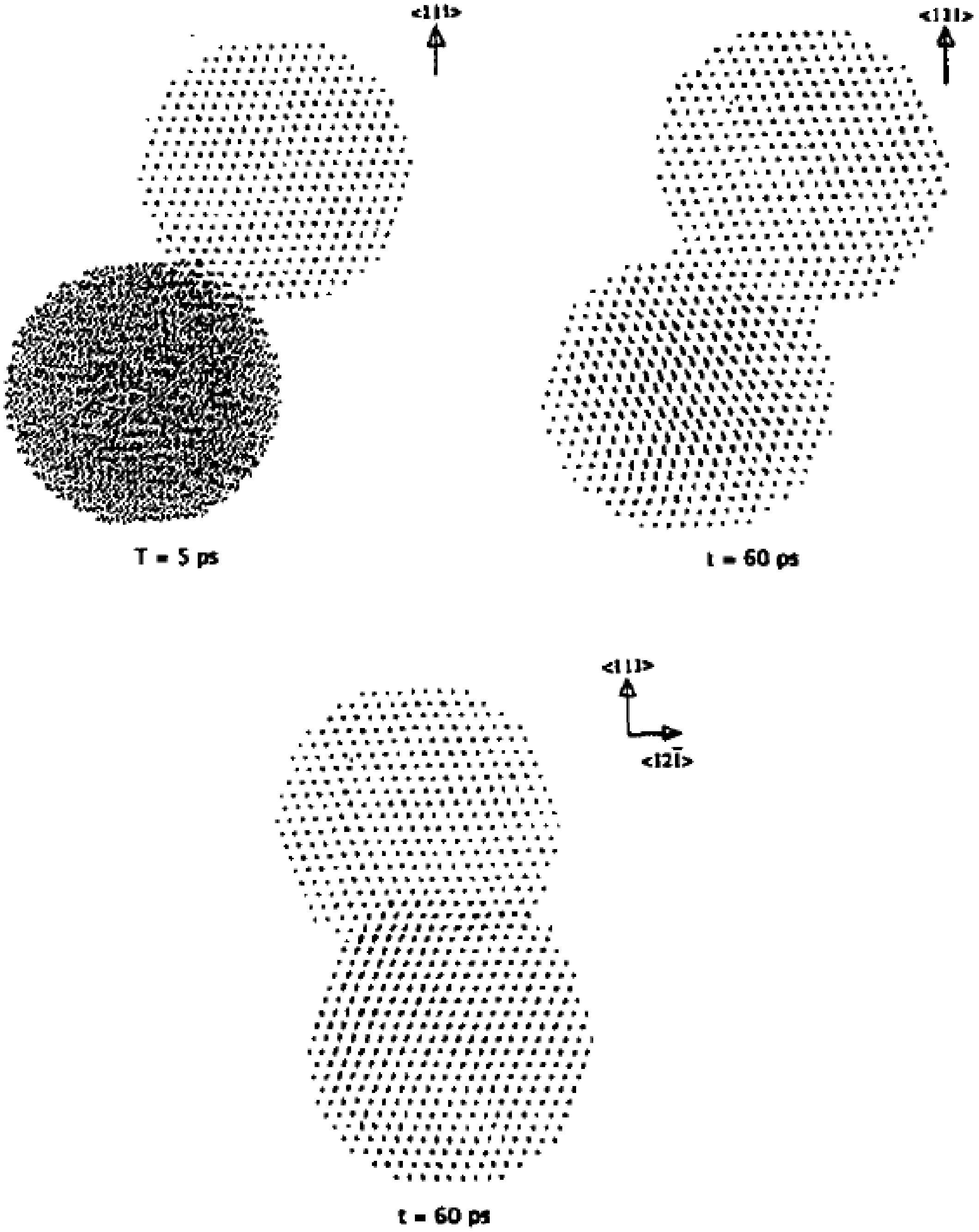

Fig. 2.18 Position of all atoms at various instants of time during two-particle sintering at 50 K, projected onto the (121) plane of the bottom [156].

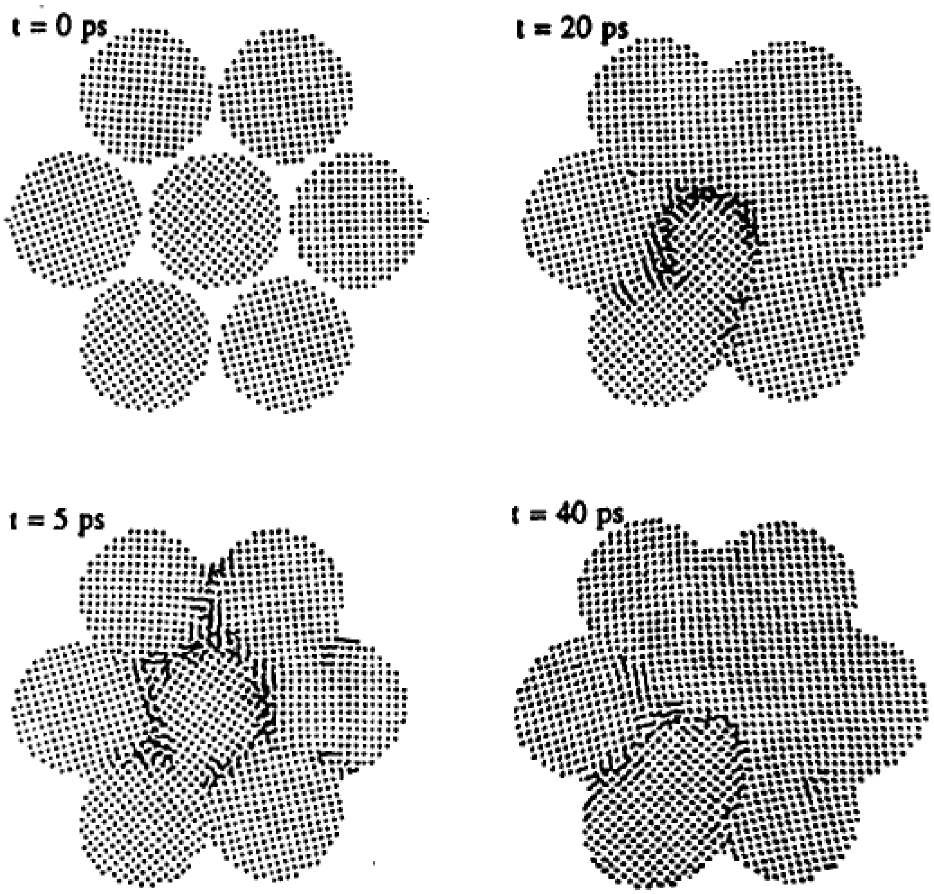

Fig. 2.19 Sintering of seven close-packed cylinders to full density at 300 K [156].

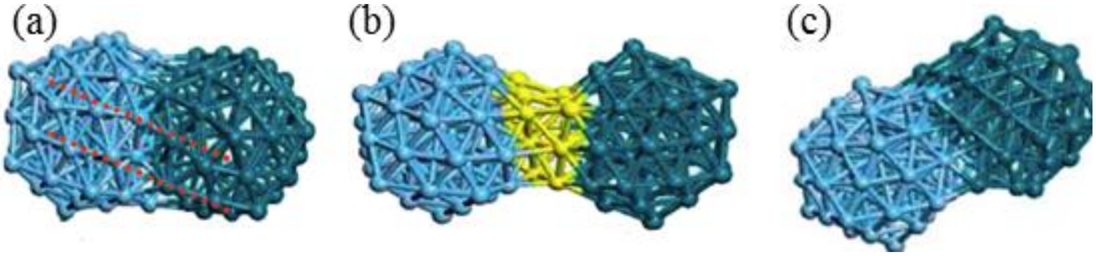

Fig. 2.20 Representative snap-shots at 0.01 K corresponding to three arranged configurations (a) vertex to vertex (b) face to face (yellow atoms highlight oriented attachment) and (c) edge to edge. The red dotted lines illustrate queues. (For interpretation of the references to color in this figure legend, the reader is referred to the web version of this article.) [157].

2.4.3 Sintering of Metallic Nanoparticles on Metallic Substrates

Sintering of metallic nanoparticles on metallic substrates has been experimentally investigated by in situ ultrahigh-vacuum TEM [158] and numerically by MD simulation [47,159]. Fig. 2.21 shows atomic plots of two 1.2 nm Au NPs sintered on Au substrate at different temperatures by MD simulation [159]. It can be clearly seen from the atomic plots that the porosity between the NPs and the substrate disappeared at 400 K. The sintering is enhanced as the temperature is increased and a thin film is almost formed on top of the substrate at 800 K. Similar trend was observed for sintering of Ag nanoparticles on Au substrate shown in Fig. 2.22 [159]. As shown in Fig. 2.23., another study has also confirmed densification of Ag NPs and Au substrate at 423 K [47]. The figure shows a non-diffusional formation of an epitaxial layer between the Ag NPs and the Au substrate after 30 ps of heating.

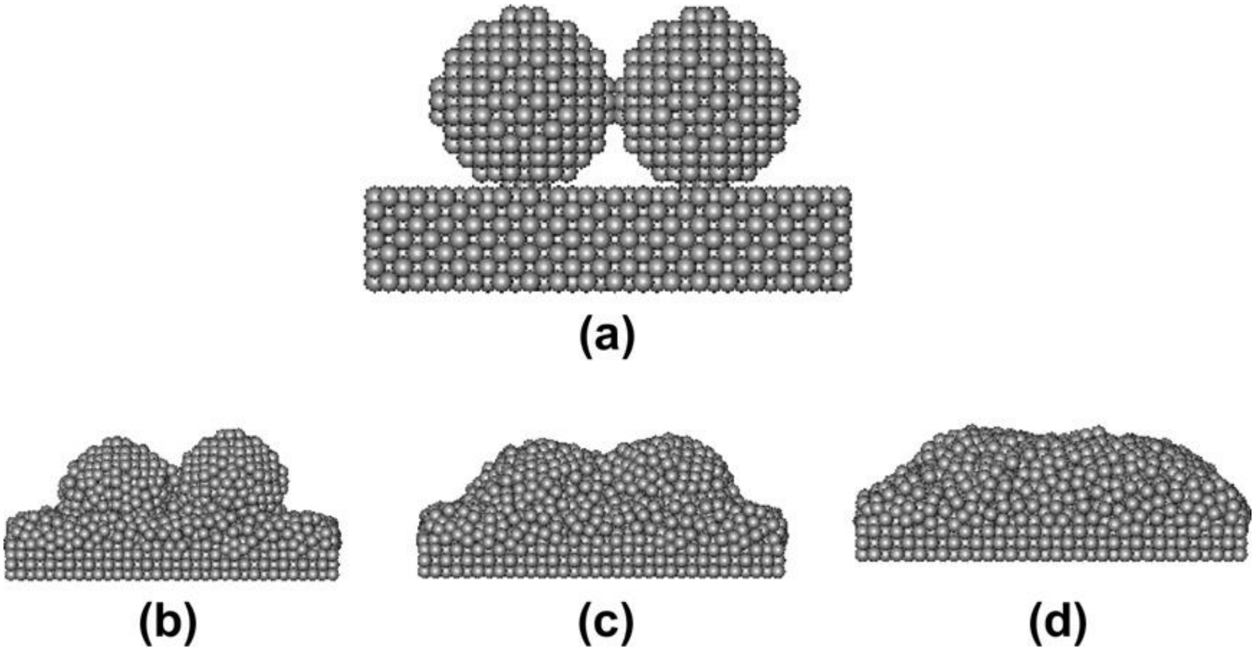

Fig. 2.21 (a) The x–z plane projection of initial configuration. The x–z plane projection at (b) 400 K, (c) 600 K and (d) 800 K with simulation time of 300 ps for Au–Au [159].

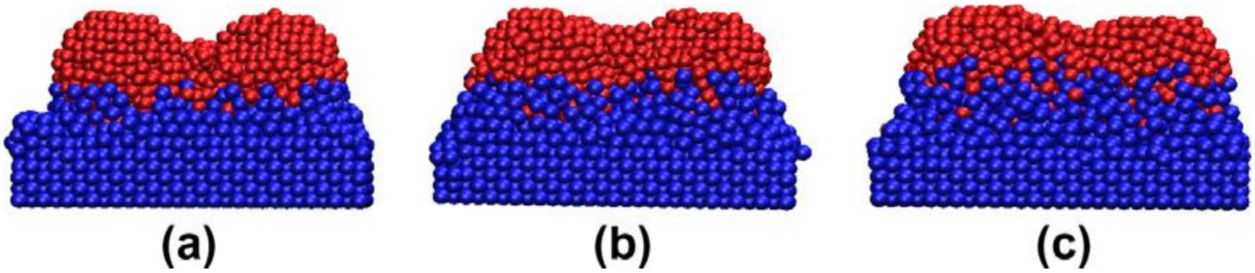

Fig. 2.22 The x–z plane projection of Ag–Au at: (a) 400 K, (b) 600 K and (c) 800 K with simulation time of 300 ps [159].

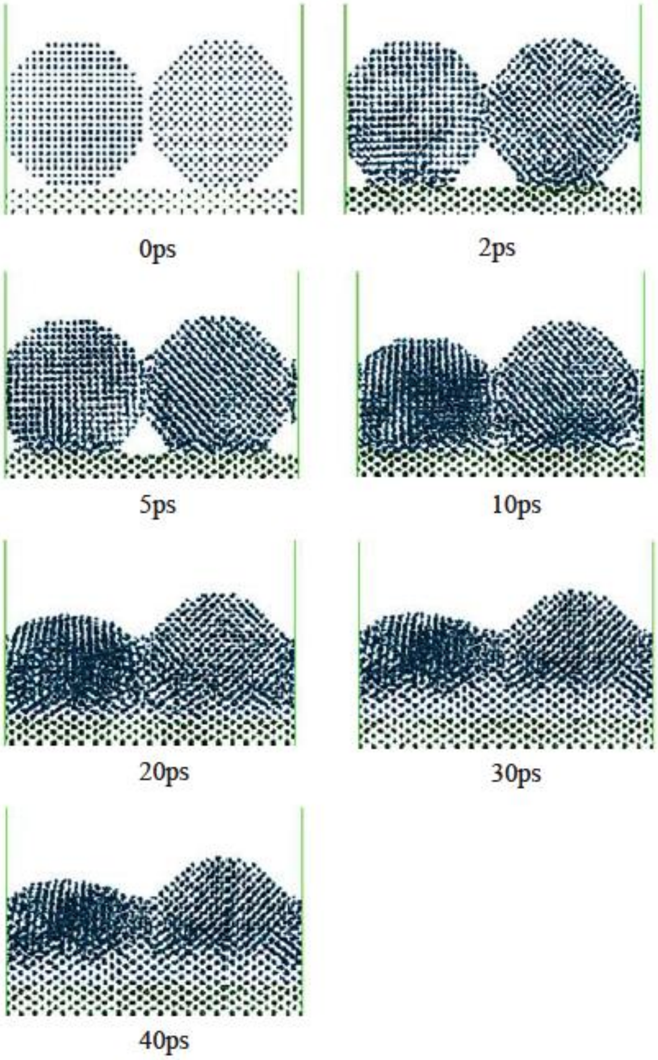

Fig. 2.23 Atom arrangement of 4 nm-sized silver nanoparticles and the gold substrate with (011) orientation at 523K. Corresponding simulation times are also shown [47].

3 METHODOLOGY

This chapter describes the methods applied in this thesis. Section 3.1 describes the fabrication method and the application of Ag NP paste in bonding Cu wires to Cu foils. The characterization methods of the paste and the bonds are also described. Section 3.2 describes the computational methods that were applied to simulate the heating process of the Ag NPs. Section 3.3 reports the analytical models of melting, surface premelting, and sintering that has been used in this thesis.

3.1 Experimental Methods

3.1.1 Cu Foils and Wires

The Cu foils was received from the manufacturer were of 50 µm thickness and 5 cm width (McMaster Carr, Aurora, OH). The foils were cut across their length into 5-cm pieces using a shear cutter. The used Cu wires were of three different diameters: 50 µm, 250 µm, and 500 µm (McMaster Carr, Aurora, OH). The wires were cut into 10-cm pieces. Prior to bonding, the foils and the wires were ultrasonically cleaned in acetone for 3 min and rinsed by ultrapure water (electrical resistivity is approximately between 16 MΩ cm and 18 MΩ cm).

3.1.2 Fabrication of Ag Nanoparticle Sol

Reduction of metal ions by reducing agents is a common way to fabricate metallic NPs [160]. In this work, Ag NPs were prepared by the reduction action of silver nitrate ($AgNO_3$) using sodium citrate dihydrate ($Na_3C_6H_5O_7.2H_2O$) [161,162]. A solution of ($AgNO_3$, 1 mM) in 250 mL ultrapure water was heated to 353 K. A volume of 10 mL aqueous solution of ($Na_3C_6H_5O_7.2H_2O$, 0.34 mM) was then added to the $AgNO_3$ solution. Heating was continued to

363 K for 30 min after adding the citrate solution. The color of the solution changed from the colorless water to yellow after 15 min of heating, and to gray after 25 min. The produced sol was simply Ag NPs coated with organic shells and dispersed in water with a concentration of 0.001 vol.%. The excess amount of citrate used in this reaction is responsible for coating the NPs with the organic shell.

The fabricated Ag NPs had an average size of 50 nm and size distribution in the range of 20 nm to 100 nm. A few Ag nanobars were found in the prepared sol as a result of different growth rates at different crystallographic planes of the particles. The length of the nanobars was approximately 100 nm, and their diameter ranged from 10 nm to 20 nm. The amount of nanobars might be reduced by adding aniline to the $AgNO_3$ solution prior to heating [163]. However, precise control of the shape and the amount of the nanobars is beyond the scope of this thesis.

3.1.3 Fabrication of Ag Nanoparticle Paste

The Ag NP paste was simply fabricated by increasing the concentration of the Ag NP sol from 0.001 vol.% to 0.1 vol.% by centrifugation. A centrifugal force of 1700 × g was applied for 30 min on 15-mL centrifuge tubes (length 118.54 mm, outer diameter 15.62 mm) filled with 0.001 vol.% sol . As a result of the centrifugal force, the Ag NPs condensed at the bottom of the centrifuge tubes, leaving only water on top. The water was extracted from the centrifuge tubes using a pipette, leaving 0.15 mL 0.1% Ag NP sol (Ag NP paste) at the bottom. The carrier of the Ag NP paste was just water. This paste was used for all experiments in this work.

3.1.4 Deposition Control of Ag Nanoparticle Paste

A fine needle attached to a 10-mL syringe was used to extract the Ag NP paste from the centrifuge tubes and deposit it onto the Cu foils. After depositing one droplet of paste onto the Cu foil, the Ag NPs migrated to the edge of the droplet, showing the coffee-ring effect (CRE) [164]. This resulted in an undesirable variation in the thickness of the deposited layer. Thus, to suppress CRE, multiple depositions of the paste on Cu foil were performed. This led to relatively uniform thickness within the droplet. A volume of 0.15 mL of the Ag NP paste was deposited on each bonded sample. The number of depositions per sample was in the range of 22 to 30 droplets. This gave a droplet volume of approximately 0.006 mL and approximately 97 µg Ag NPs for each deposition. The droplets were dried at 353 K after each deposition.

3.1.5 Bonding Technique

After depositing the Ag NPs onto the Cu foil, the Cu wire was mounted on the Ag NP paste and clamped by a 2-inch screw clamp. A schematic diagram of the clamping geometry is shown in Fig. 3.1. An alumina ceramic piece was placed underneath the screw to prevent bonding between the Ag NPs and the metallic screw. The pressure exerted on the sample was 5 MPa, which was determined by dividing the applied force by the area of the ceramic piece. The applied force was measured using a load cell. A torque wrench was used to tighten the screw and thus to exert the same force on all samples. The clamped sample was then heated at the bonding temperature for 30 min.

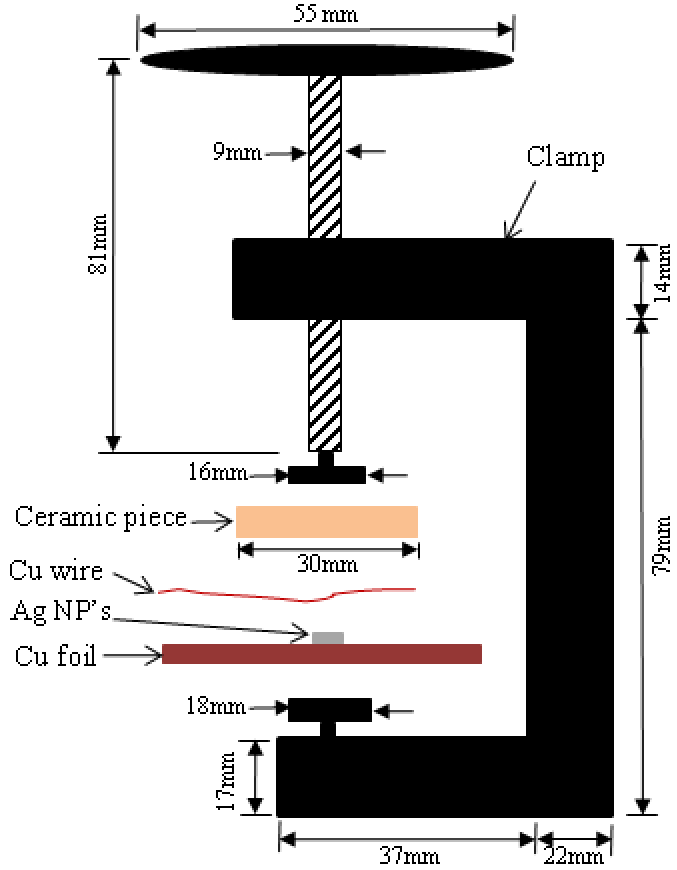

Fig. 3.1 Schematic diagram of clamping the Cu wire to the foil.

3.1.6 Shear Testing

Shear testing was applied by shearing the wire at a rate of 5 mm/min. Fig. 3.2 (a) shows an optical image of a 50-µm Cu wire bonded to Ag NPs, and a schematic diagram of the shear test is shown in Fig. 3.2 (b). To avoid bending on the joint, the wire was clamped at a distance of 7 cm from the joint. The maximum shear strength was calculated by dividing the maximum force by the area of the bond. Three samples were tested for each shear experiment.

The used needle deposited droplets that covered the foil with a circular area of 4.00 ± 0.25 mm in diameter; any extra area resulting from uncontrolled deposition was scratched. After clamping, the Cu wire deformed to a nearly elliptical shape and formed a contact with the Ag

NPs. The contact area was estimated by multiplying the length of the cross-sectional contact between the deformed wire and the foil by the diameter of the Ag NP coverage on the foil. Both lengths were measured for each sample by optical microscopy.

Shear testing at high temperature was performed by heating the unbonded side of the foil using a heat gun. The temperature of the sample was measured using a thermocouple attached to the bonded side, 10 mm away from the joint. The shear test was run just after the joint reached the desired temperature.

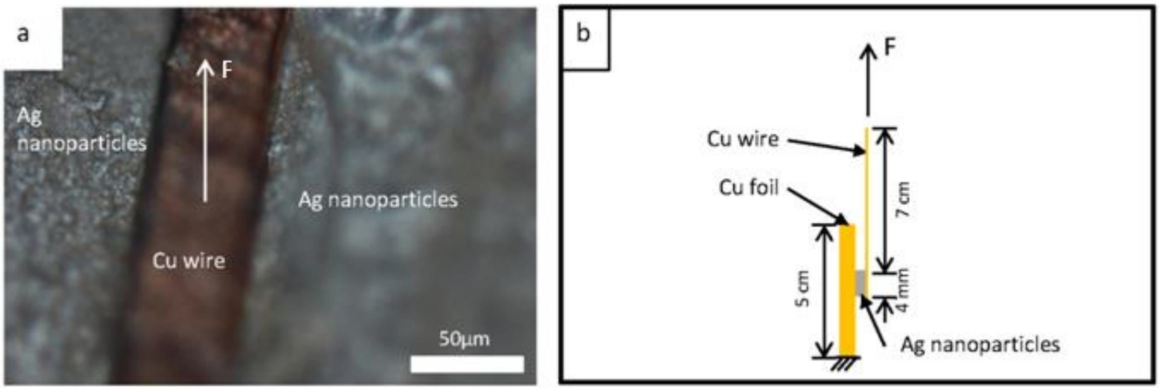

Fig. 3.2 (a) Optical image and (b) schematic diagram of a shear sample.

3.1.7 Microstructure Analysis

A field-emission scanning electron microscope (Leo1530 FE-SEM; Zeiss, Germany) was used to examine the microstructure of the sintered NPs and the bonded samples. The sintering studies were performed by depositing one droplet of the Ag NP paste on silicon wafers. The sintering measurement was based on measuring the neck radius in the sintered NPs, which was measured from SEM images by ImageJ software. The radii of at least 10 necks per sample were averaged.

The bonded samples were mounted in epoxy, cross-sectioned, and then polished by 0.25-µm diamond paste. The samples were coated with a 10 nm gold layer prior to SEM observation. For TEM studies, the bonded samples were sectioned by microtomy.

3.1.8 Thermogravimetric Analysis (TGA) and Raman Spectroscopy

TGA was performed by heating the Ag NP paste from RT to 723 K. To study the effect of annealing of the Ag NP paste on the decomposition of the organic shell, the paste was annealed at 433 K and 473 K for 30 min prior to the TGA tests. The tests were run in air with a heating rate of 5 K/min.

Raman spectroscopy of the Ag NPs was performed to identify the composition of the organic shell and to study the effect of annealing of the Ag NP paste on the decomposition of the organic shell. The Raman spectra were recorded using a Renishaw spectrometer excited with an Ar laser at wavelength of 488 nm. The samples were prepared by depositing Ag NP paste on a silicon wafer.

3.2 Computational Methods

The initial atomic structure of all simulated Ag NPs in this work is arranged in FCC truncated octahedral, which defines planes (111) and (100) as surface facets [106]. Fig. 3.3 shows the initial atomic arrangement of a 4 nm Ag NPs viewed at the (100) and the (111) surface facets. A previously developed linear scaling parallel MD code was used to investigate the melting and the surface premelting behaviours of the NPs [165]. This code was based on the Voter-Chen version [166] of the embedded atom method (EAM) potential [167]. Unlike a first-principles method, semi-empirical methods such as EAM can be used to simulate large sizes of NPs as well as very small clusters [168]. Simulation of large NPs can only be performed by using semi-empirical potentials such as Sutton-Chen [169], the many-body Gupta [170], Finnis-Sinclair [171], the embedded atom [172-176] and related methods [127,177-178], and molecular dynamics simulations [114,179-182]. The EAM was chosen for the generality of its functional, good agreement with experiments and the first principles calculations, and the high computational efficiency that allows the simulation of relatively large NPs. The embedded-atom model was originally developed by Daw and Baskes [183] and parameterized by Voter and Chen [166] by simultaneously fitting the potential to the properties of bulk silver and Ag_2. The total energy E of a mono-atomic system in the EAM potential is represented by

$$E_{\mathrm{tot}} = \sum_{\mathrm{i}} F(\bar{\rho}_{\mathrm{i}}) + \frac{1}{2}\sum_{\mathrm{i}\neq\mathrm{j}} V(r_{\mathrm{ij}}) \qquad (3.1)$$

where $V(r_{\mathrm{ij}})$ is a pair-wise potential as a function of the inter-atomic distance r_{ij} between atoms i and j, F is the embedding energy, and $\bar{\rho}_{\mathrm{i}}$ is total host electron density at the position of atom i and can be calculated by the following formula

$$\bar{\rho}_{\mathrm{i}} = \sum_{\mathrm{i}\neq\mathrm{j}} \rho(r_{\mathrm{ij}}) \qquad (3.2)$$

where $\rho(r)$ is the density function and can be calculated by the following equation:

$$\rho(r) = r^6\left[e^{-\beta r} + 2^9 e^{-2\beta r}\right] \qquad (3.3)$$

where r is the distance between the atoms, and β is an adjustable parameter.

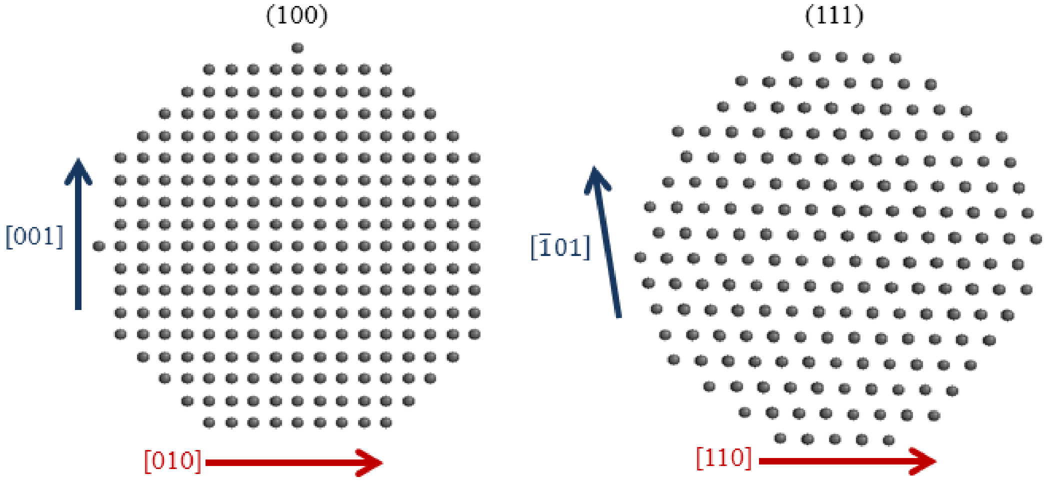

Fig. 3.3 Initial atomic arrangement of the 4 nm Ag particles showing (100) and (111) facets of the truncated octahedral configuration.

The pair-wise potential $V(r)$ based on Morse potential is calculated using the following equation

$$V(r) = D_{\mathrm{M}}\left[1 - e^{\alpha_{\mathrm{M}}(r-R_{\mathrm{M}})}\right]^2 - D_{\mathrm{M}} \qquad (3.4)$$

where D_{M} is depth of the potential well, R_{M} is the inter-atomic distance at the minimum of the potential well, and α_{M} is a measure of the curvature of the potential well at its minimum, respectively. Table 3.1 shows the values of the fitting parameters of the embedded atoms potential for Ag.

Table 3.1: Fitting parameters of the embedded atom potential for Ag.

D_{M} (eV)	R_{M} (Å)	α_{M} (Å^{-1})	β_{M} (Å^{-1})	r_{cut} (Å) *
0.6721	2.5700	1.8260	3.9060	5.5420

*cutoff radius.

For higher precision, Hamming's modified 4th order predictor-corrector propagator has been employed with a step size of 2 femto seconds, which guarantees the conservation of total energy of a NP within an accuracy range of 0.03%-0.15%. The initial velocities of atoms in the

NP were assigned according to the Maxwell-Boltzmann distribution at a specific temperature. The NPs were first relaxed at 300 K (room temperature) for 20 ps to achieve equilibration before heating, which was gradually applied by increasing the NP temperature in intervals. This was achieved by multiplying the velocities of atoms by a scaling factor that is calculated as a ratio of the target temperature to the present temperature. Accordingly, the total kinetic energy (E_{k}) of the atoms in the NPs is obtained via the equipartition theorem. The NPs were then equilibrated for 20 ps at each temperature, which was long enough to dampen the fluctuations in temperature. Consequently, the NPs reached the desired temperature at each heating interval in a reliable manner. From this fact, one may argue that the equilibrium averages, which are sensitive to temperature fluctuations, were reasonably taken into consideration. However, it is important to point out that a simple velocity rescaling scheme was used to fix the temperature rather than contacting with a heat bath such as the Nose-Hoover thermostat. Nevertheless, one may argue that the present velocity rescaling scheme has successfully maintained thermodynamic properties in the canonical ensemble averages by applying an appropriate heating rate.

During the heating process, the last phase space point of a calculation was used as an input for the next temperature calculation and the temperature (or E_{k}) and average potential energy (PE) were calculated. Heating of the NPs was then gradually applied by increasing their internal kinetic energies (E_{k}) for 20 ps at each temperature interval. The temperature of the NP was calculated by the following equation:

$$T = \frac{2\langle E_{\mathrm{k}} \rangle}{k(3N - 6)} \qquad (3.5)$$

where E_k is the total kinetic energy of the atoms in the NP, k is the Boltzmann constant, and N is total number of atoms in the NP. The dynamics were monitored by short-time (10 fs) averages of the NP temperature. The short-time average was taken to lower the fluctuation in the kinetic energy values that occurred due to the flow between the potential energy and the kinetic energy during the oscillation of the atoms around their equilibrium positions. Taking the short-time average is more important at high temperatures as the fluctuations in the kinetic energy values become larger.

The heating rate was chosen based on a trade-off between physical reasoning and computational expenses. Although instantaneous heating is computationally less expensive than gradual heating, the system may stick on a local minimum at the potential energy surface (PES). Therefore, gradual heating on the NPs were performed. The heating rate was chosen based on a preliminary simulation performed on a 4 nm particle in the range of 325 K to 1675 K with 50 K steps leading to a T_m value of about 875 K. For better accuracy during the melting stage, temperature step was reduced for all sizes of NPs to 10 K in the range of 825 K to 1275 K. The maximum temperature of this range was chosen to be slightly higher than T_m of the bulk (1235 K).

3.3 Analytical Methods

3.3.1 Melting of Ag Nanoparticles

T_m values obtained here will be compared to those obtained by the liquid drop model (LDM) [21], Shi's model [22], and Hanszen's model [23]. The liquid drop model assumes that T_m of a NP is primarily based on the variation of the cohesive energy and the surface tension of the NP. According to the liquid drop model, the bulk atomic cohesive energy per coordination number can be related to the melting point of the bulk $T_{\mathrm{m}}(\infty)$ by the following equation

$$a_{\mathrm{v}} = 0.0005736T_{\mathrm{m}}(\infty) + c \qquad (3.6)$$

also, average cohesive energy per atom of a NP can be related to its complete melting point $T_{\mathrm{m}}(d)$ by the following equation

$$a_{\mathrm{v,d}} = 0.0005736T_{\mathrm{m}}(d) + c \qquad (3.7)$$

where c is a constant in both equations and d is the diameter of the NP. Average cohesive energy per atom ($a_{\mathrm{v,d}}$) of a NP can be directly related to cohesive energy of the bulk (a_{v}), atomic volume (v_{o}), and the solid-vapor interfacial energy (γ_{sv}) by the following equation:

$$a_{\mathrm{v,d}} = a_{\mathrm{v}} - \frac{6v_{\mathrm{o}}\gamma_{\mathrm{sv}}}{d} \qquad (3.8)$$

Equation (3.8) shows that cohesive energy per atom decreases as the size of the NP decreases and the rate of the decrease depends on the atomic volume (v_{o}) and the solid-vapor interfacial energy (γ_{sv}). By replacing the values of the cohesive energies in equation (3.8) by the values of the complete melting points from equations (3.6) and (3.7), we get

$$T_{\mathrm{m}}(d) = T_{\mathrm{m}}(\infty)\left(1 - \frac{6v_{\mathrm{o}}\gamma_{\mathrm{sv}}}{0.0005736dT_{\mathrm{m}}(\infty)}\right) \qquad (3.9)$$

where $T_{\mathrm{m}}(d)$ and $T_{\mathrm{m}}(\infty)$ are complete melting points of the NP and the bulk; respectively. Equation (3.9) was modified to equation (3.10) by introducing a dimensional parameter β that depends on v_{o} and γ_{sv}

$$T_{\mathrm{m}}(d) = T_{\mathrm{m}}(\infty)\left(1 - \frac{\beta}{d}\right) \tag{3.10}$$

where melting point of bulk Ag is 1235 K and β is estimated as 0.96564 nm [21].

Shi's model was also considered to find T_{m} of the NPs [22]. The model was based on Lindemann's criterion [24], which suggested a NP melts when the msd value of the atoms exceeds a certain fraction of the interatomic distance. Shi specified T_{m} based on the average msd value of both the bulk and surface atoms and can be calculated by the following equation

$$T_{\mathrm{m}}(d) = T_{\mathrm{m}}(\infty) exp\left[-(\alpha - 1)/\left(\frac{d}{2r_{\mathrm{o}}} - 1\right)\right] \tag{3.11}$$

where r_{o} is the NP radius at which all atoms are located at the surface, and α is a material constant that can be calculated by the following equation

$$\alpha = \frac{2S_{\mathrm{vib}}(\infty)}{3R} + 1 \tag{3.12}$$

where $S_{\mathrm{vib}}(\infty)$ is a vibrational component of melting entropy (= 7.98 J/mol.K for bulk Ag) [184] and R is the ideal gas constant (=8.314 J/mol.K), this will give $\alpha = 1.64$. The value of r_{o} is equal to $3h$, where h is the height of a monolayer of atoms on the bulk crystal surface. The value of h is equal to $a/2$ for FCC material, where a is the lattice constant (a = 0.409 nm for Ag). This will give r_{o} as 0.6135 nm for Ag.

Hanszen's model was also considered for finding T_{m} of a NP [23]. Hanszen assumed that T_{m} and T_{sm} are equal and the melting process starts at the surface of the NP by forming a liquid layer of a given critical thickness (t_{o}) around the solid core at T_{m} of the NP. Any infinitesimal increase of the temperature above T_{m} destroys the equilibrium between the liquid layer and the solid core and the liquid layer would expand into the solid core of the NP. According to Hanszen's model, the complete melting point of a NP can be determined by the following equation

$$T_{\mathrm{m}}(d) = T_{\mathrm{m}}(\infty) - \frac{2T_{\mathrm{m}}(\infty)}{Q}\left[\frac{\gamma_{\mathrm{sl}}}{\rho_{\mathrm{s}}\left(\frac{d}{2} - t_{\mathrm{o}}\right)} + \left(\frac{2\gamma_{\mathrm{lv}}}{d} + \frac{\Delta P}{2}\right)\left(\frac{1}{\rho_{\mathrm{s}}} - \frac{1}{\rho_{\mathrm{l}}}\right)\right] \quad (3.13)$$

where Q is the latent heat of fusion of the bulk, t_{o} is the critical thickness of the liquid layer, γ_{sl} and γ_{lv} are the bulk interfacial energy between solid-liquid and liquid-vapor, respectively, ρ_{s} and ρ_{l} are the densities of solid and liquid, respectively, ΔP is the difference between the vapour pressure of a flat liquid surface $(r = \infty)$ at $T_m(\infty)$ and the vapour pressure at the surface of a liquid shell with an outer radius r at $T_{\mathrm{m}}\,(d)$. By substituting the following values of Ag variables into Equation (3.13): (Q =1.06×10^9 erg/g, γ_{sl}= 184 dyn/cm, γ_{lv}= 910 dyn/cm , ρ_{s}= 10.49 g/cm^3, ρ_{l} = 9.35 gm/cm^3, ΔP can be ignored for Ag) [185], we get the following simplified equation

$$T_{\mathrm{m}}(d) = T_{\mathrm{m}}(\infty) - 2463\left(\frac{1}{0.603\left(\frac{d}{2} - t_{\mathrm{o}}\right)} - \frac{2}{d}\right) \quad (3.14)$$

The theoretical surface premelting point (T_{sm}) was calculated by the following equation that was developed by Chernyshev [102]

$$T_{\mathrm{sm}}(d) = \left(\frac{3}{4}\alpha\right)^{-1}\{1 + y(d)\}exp[-y(d)]T_{\mathrm{m}}(\infty) \quad (3.15)$$

where $y(d)$ is a function that can be calculated by equation (3.16).

$$y(d) = \frac{(\alpha - 1)}{\left(\frac{d}{2r_{\text{o}}} - 1\right)} \qquad (3.16)$$

Chernyshev developed the model based on Shi's model and has shown that surface premelting does not take place if the NP radius is smaller than a critical radius r_{c}, which is different for different materials. Instead, the surface layer makes a transition to a pseudo-crystalline state before the whole particle melts [103].

3.3.2 Sintering of Ag Nanoparticles

Sintering rates of the Ag NPs was calculated based on three different mechanisms, surface diffusion, lattice diffusion, and grain boundary diffusion. Diffusion coefficients of NPs are size and temperature dependent and can be calculated by the following equation [186].

$$D(r,T) = D_{\text{o}}(\infty)\text{exp}\left[\frac{-E(\infty)}{RT} exp\left[\frac{-2S_{\text{vib}}(\infty)}{3R}\frac{1}{\frac{r}{r_{\text{o}}}-1}\right]\right] \qquad (3.17)$$

where *r* is the NP radius, *T* is the temperature, $D_{\text{o}}(\infty)$ is the bulk pre-exponential constant which is equal to ($D_{\text{o}}(\infty)$=5×10^{3} m^{2}/s) for surface diffusion, ($D_{\text{o}}(\infty)$=1.2×10^{-5} m^{2}/s) for grain boundary diffusion, and ($D_{\text{o}}(\infty)$=4.4×10^{-5} m^{2}/s) for volume diffusion [187], $E(\infty)$ is bulk activation energy and is equal to ($E(\infty)$=2.661×10^{5} J/mol), ($E(\infty)$=9×10^{4} J/mol), and ($E(\infty)$=18.5×10^{4} J/mol) for surface diffusion, grain boundary diffusion, and lattice diffusion, respectively [187].

Rates of sintering can be determined based on the change in neck radius to particle radius ratio (*x/r*), which can be calculated by the following equation [188].

$$\frac{x}{r} = \left(\frac{Bt}{r^m}\right)^{\frac{1}{n}} \qquad (3.18)$$

where t is the sintering holding time, B is a temperature dependent sintering function, the values of n and m vary based on the sintering diffusion mechanism. If sintering is driven by surface diffusion, equation 3.18 becomes

$$\left(\frac{x}{r}\right)_{\mathrm{surf}} = \left(\frac{4.17\delta D_{\mathrm{s}}\gamma_{\mathrm{sv}}\Omega t}{r^4RT}\right)^{\frac{1}{6}} \qquad (3.19)$$

where δ is the surface layer thickness and is estimated as 0.3 nm for Ag [187], D_{s} is the surface diffusion coefficient calculated by equation 3.17, γ_{sv} is the bulk solid-vapor interfacial surface energy and can be estimated as 1.14 J/m^2 for Ag [189], and Ω is the molar volume (10.3 cm^3/mol for Ag),. If sintering is driven by grain boundary diffusion, equation 3.18 becomes

$$\left(\frac{x}{r}\right)_{\mathrm{gb}} = \left(\frac{32wD_{\mathrm{gb}}\gamma_{\mathrm{sv}}\Omega t}{r^4RT}\right)^{\frac{1}{6}} \qquad (3.20)$$

where w is the grain boundary width and is estimated as to 0.5 nm for Ag [187], and D_{gb} is the grain boundary diffusion coefficient, which can be calculated by equation 3.17. For lattice diffusion sintering, equation 3.18 becomes

$$\left(\frac{x}{r}\right)_{\mathrm{l}} = \left(\frac{42.05D_{\mathrm{l}}\gamma_{\mathrm{sv}}\Omega t}{r^3RT}\right)^{\frac{1}{4.78}} \qquad (3.21)$$

where D_{l} is the lattice diffusion coefficient calculated by equation 3.17.

4 Ag NANOPARTICLE PASTE FOR LOW-TEMPERATURE BONDING OF Cu

This chapter reports the characteristics of the fabricated Ag NPs paste and the formed bonds between Cu wires to Cu foils in temperature range of 433 to 573 K. The Ag NPs paste was characterized by SEM, TEM, TGA and Raman spectroscopy. The effects of temperature and time on the sintering behavior of the bonding paste were examined by SEM. The Ag NPs in the paste are coated with a 1 nm organic shell of citrate group. The decomposition of the organic shell and its role in promoting the bonding process is discussed. The interfaces between the Ag NPs and Cu were examined by SEM and TEM. The strength of the formed bonds was examined by shear tests. The bond strength was also investigated at a higher temperature than the temperature at which the bond was formed. Parts of the reported research in this chapter have been published in *Journal of Electronic Materials* [190], and in *Applied Physics Letters* [191].

4.1 Results and Discussion

4.1.1 Organic Shell Decomposition and Sintering of Ag Nanoparticles

Fig. 4.1 shows that the concentration of Ag NPs was dramatically increased after centrifugation. Fig. 4.2 shows a TEM image of a single Ag NP coated with the organic shell of about 1 nm thickness. TGA analysis of the Ag NPs is shown in Fig. 4.3. The weight loss percentage showed two major drops in sample weight. The first, at 373 K, corresponds to evaporation of water. The second weight loss, between 423 K and 473 K, corresponds to decomposition of the organic shell. These weight drops disappeared after annealing the NPs for 30 min at 433 K and 473 K. This indicates that most part of the organic shell was decomposed at these temperatures.

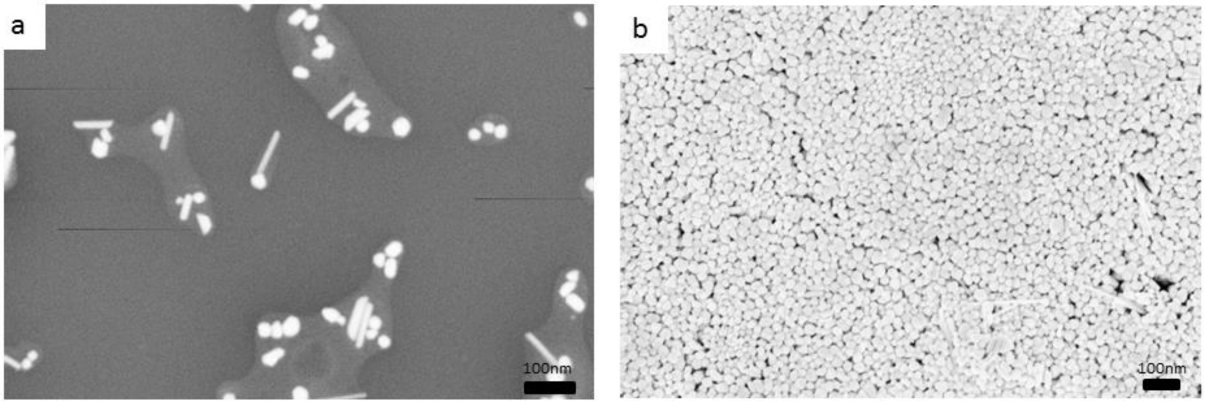

Fig. 4.1 Concentration of Ag NPs (a) before and (b) after centrifugation.

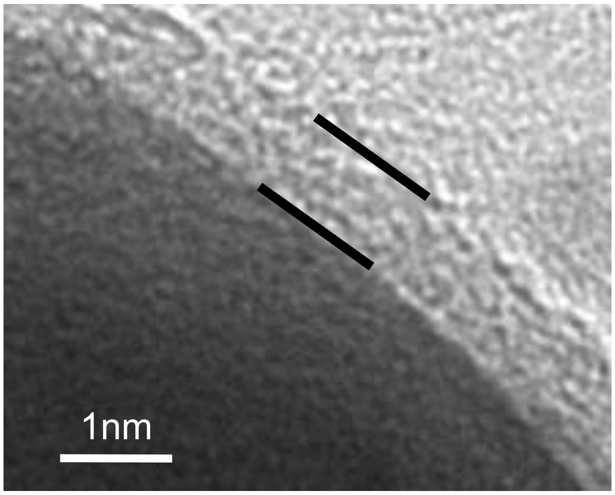

Fig. 4.2 TEM image of the surface of the NP coated by an organic shell of 1 nm thickness.

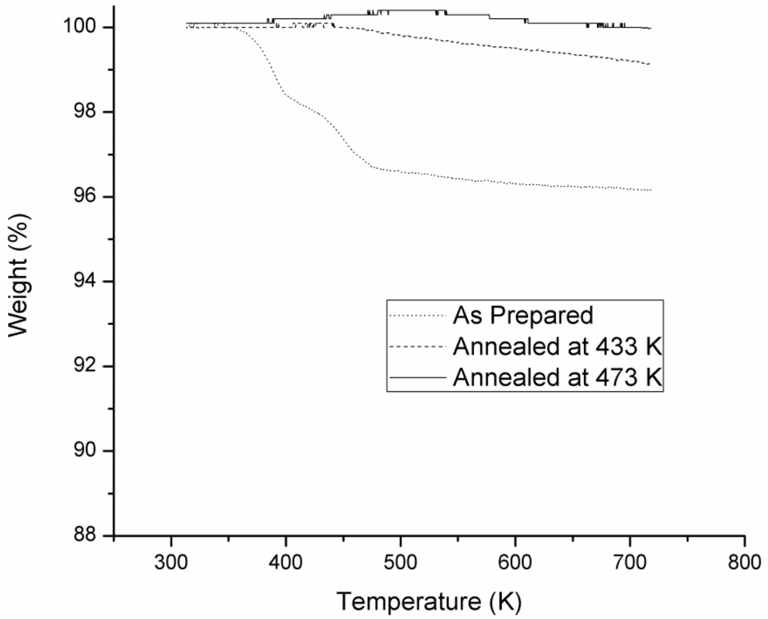

Fig. 4.3 TGA curves of Ag NPs sintered at RT, 433 K, and 473 K.

Raman spectroscopy analysis of the Ag NPs annealed at 473 K for different times is shown in Fig. 4.4. The resulting Raman peaks correspond to CH_2 at 2919 cm^{-1} (2939 cm^{-1}) [192], COO group and CO_3 at 690 cm^{-1} (663-683 cm^{-1}) [192], 1375 cm^{-1} (1360-1373 cm^{-1}) [192], and 1522 cm^{-1} (1470-1530 cm^{-1}) [192], $AgCO_3$ at 1056 cm^{-1} (1072 cm^{-1}) [193], and CO at 2116 cm^{-1} (2143 cm^{-1}) [193]. The intensities of the hydrocarbon peaks decreased as the annealing time increased due to the continuous decomposition of the organic shell. Raman curve for 5 min annealing showed very weak citrate peaks, which confirms the decomposition of the organic shell.

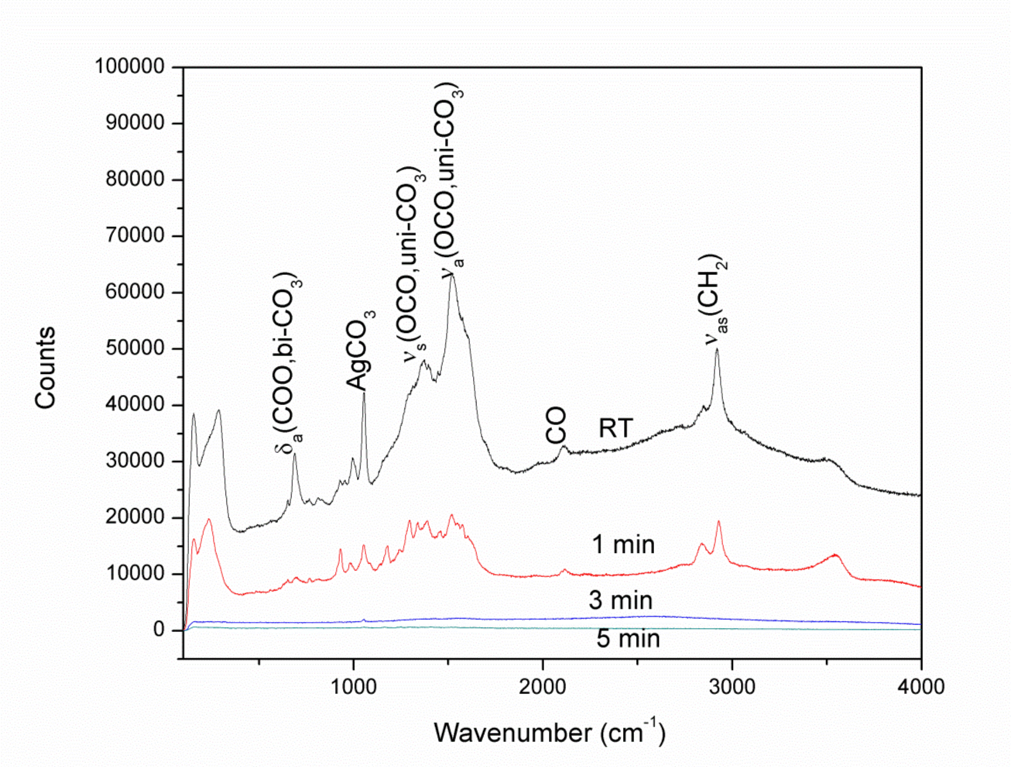

Fig. 4.4 Raman spectroscopy of Ag NPs annealed at 473 K for different times.

Fig. 4.5 shows the effect of sintering time at 473 K on the pressureless sintering behavior of the Ag NPs. The degree of sintering was enhanced as the period of sintering is increased. Measurement of the radius of a few necks and grains is shown in the figure. The relationship between the sintering time and the neck radius is shown in Fig. 4.6. Neck growth was observed after 1 min of sintering, it continued for 5 min, and then the neck radius became nearly constant.

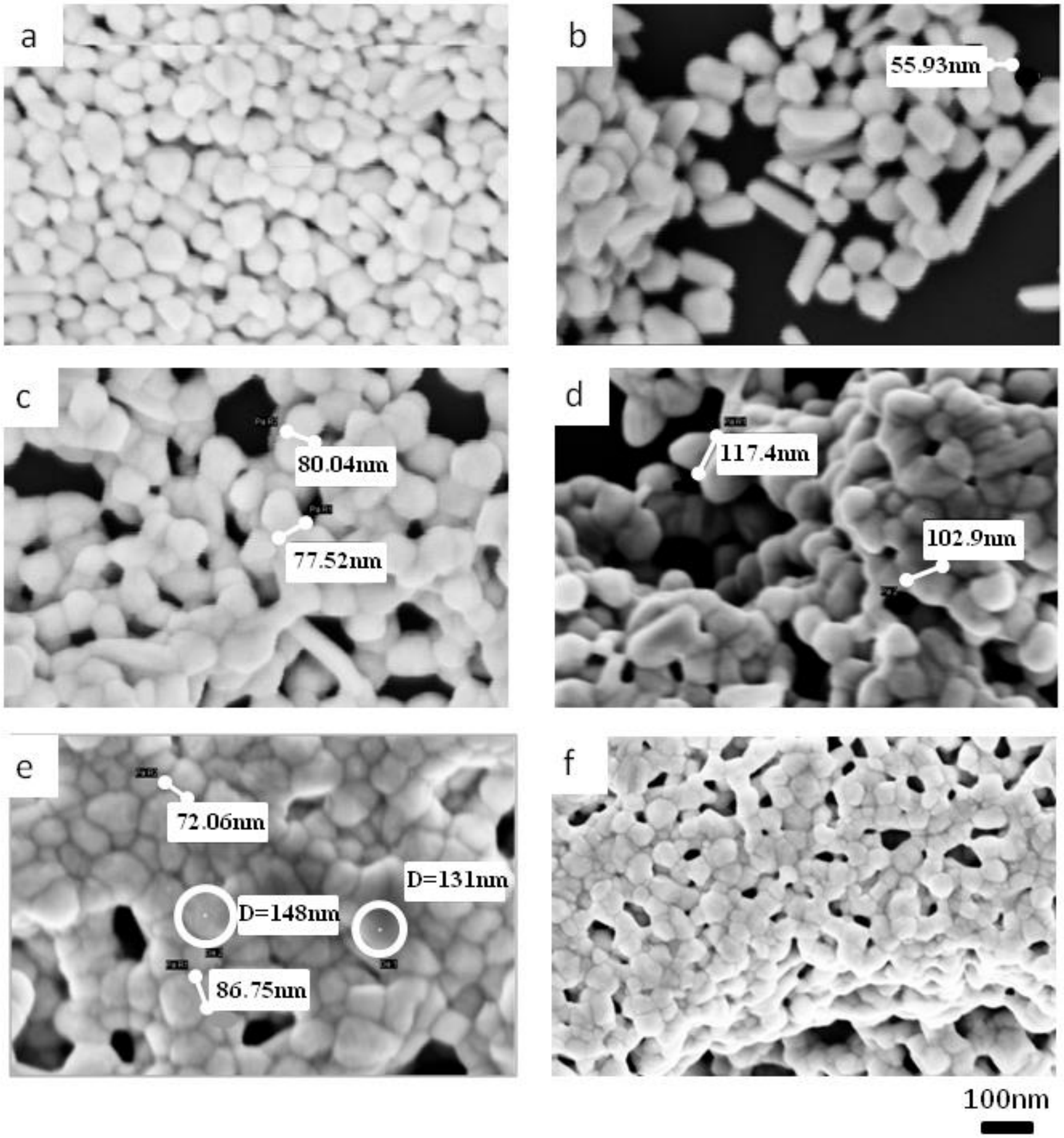

Fig. 4.5 SEM images of Ag NPs (a) at RT and sintered at 473 K for (b) 1 min, (c) 3 min, (d) 5 min, (e) 10 min, and (f) 30 min.

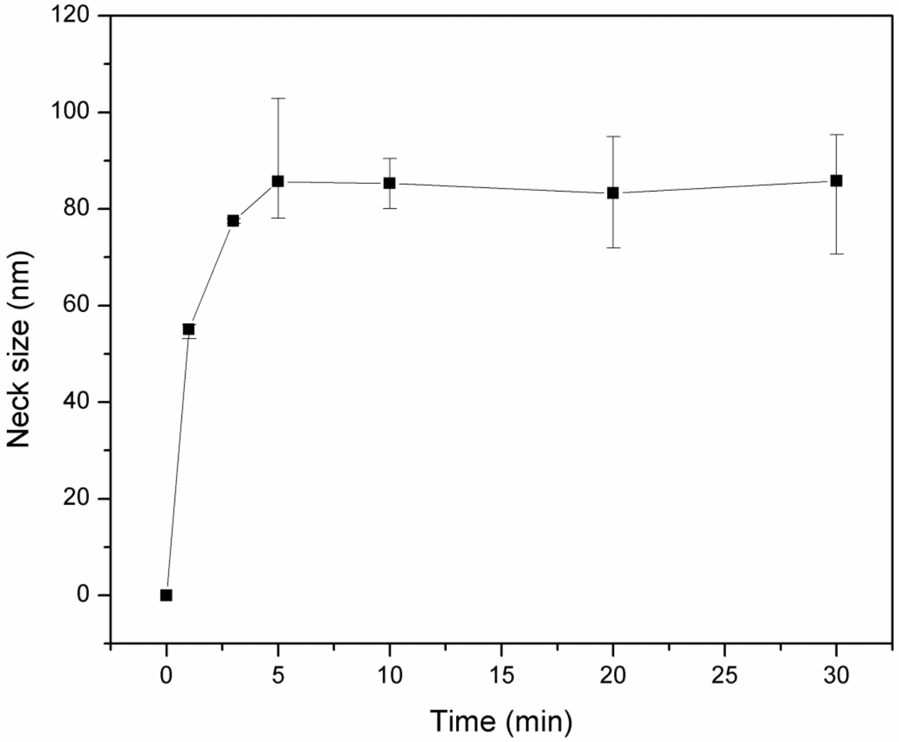

Fig. 4.6 Relation between neck radius of Ag NPs and sintering time at 473 K.

The effect of sintering temperature on the sintering behavior of Ag NPs is shown in Fig. 4.7. The Ag NPs were sintered for 30 min at 373 K, 423 K, 473 K, 523 K, and 573 K. The SEM images showed clear sintering and neck growth between Ag NPs at 373 K and 423 K. No coalescence was observed at these low temperatures. As the sintering temperature increased to 473 K, coalescence and grain growth started to appear in some areas. Dramatic coalescence and grain growth to 500 nm was observed at 523 K and 573 K.

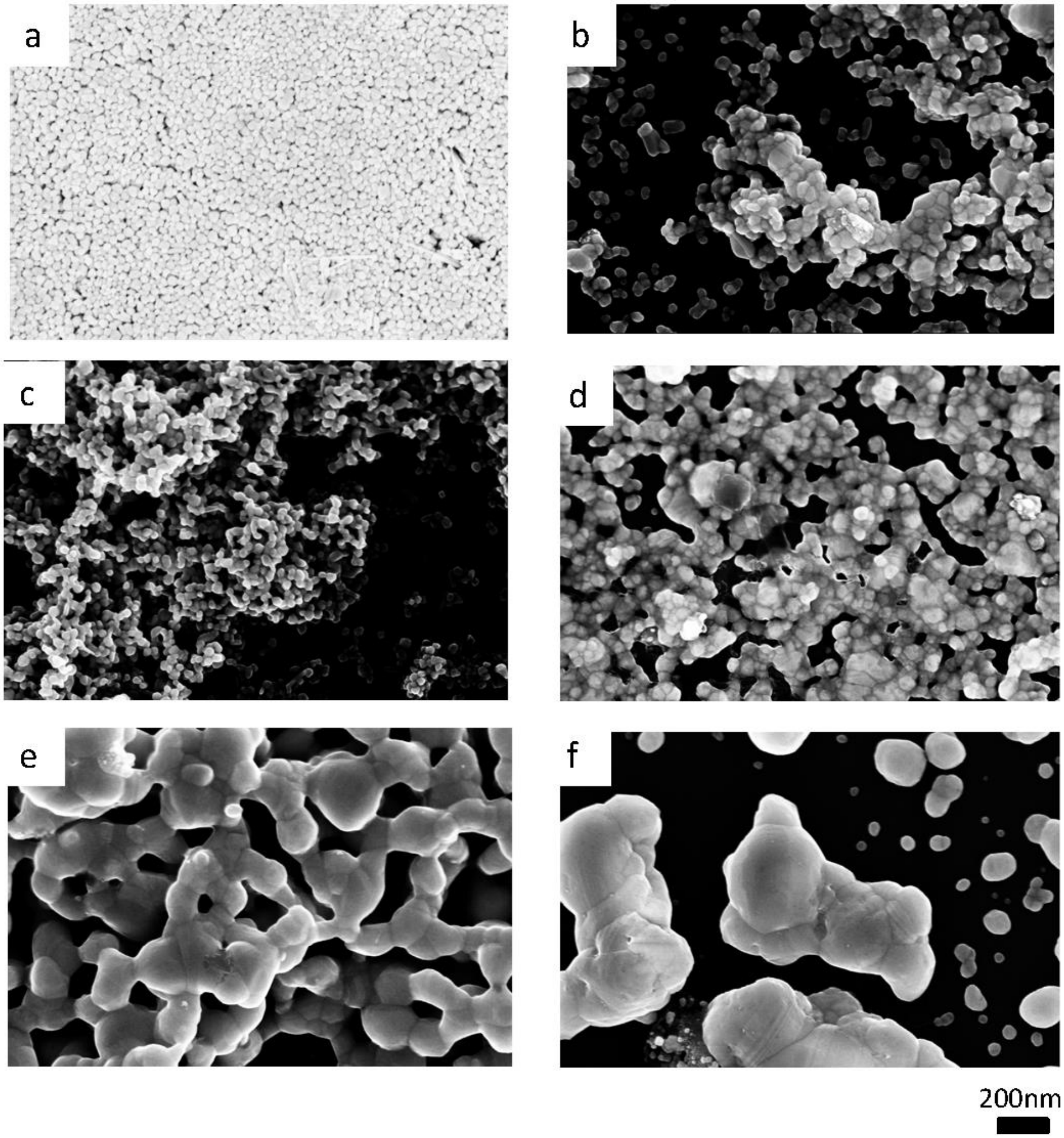

Fig. 4.7 SEM images of Ag NPs (a) at RT and sintered for 30 min at (b) 373 K, (c) 423 K, (d) 473 K, (e) 523 K, and (f) 573 K.

4.1.2 Metallurgical Bond between Cu and Ag Nanoparticles

To get a uniform distribution of Ag NPs, multiple depositions of the NP paste onto the Cu foil were performed. Fig. 4.8 (a) clearly shows the CRE after one deposition, i.e., there was high concentration of NPs in the ring and relatively less distribution in the central area. After multiple depositions, the CRE disappeared and more uniform thickness of the Ag NPs was achieved, as shown in Fig. 4.8 (b).

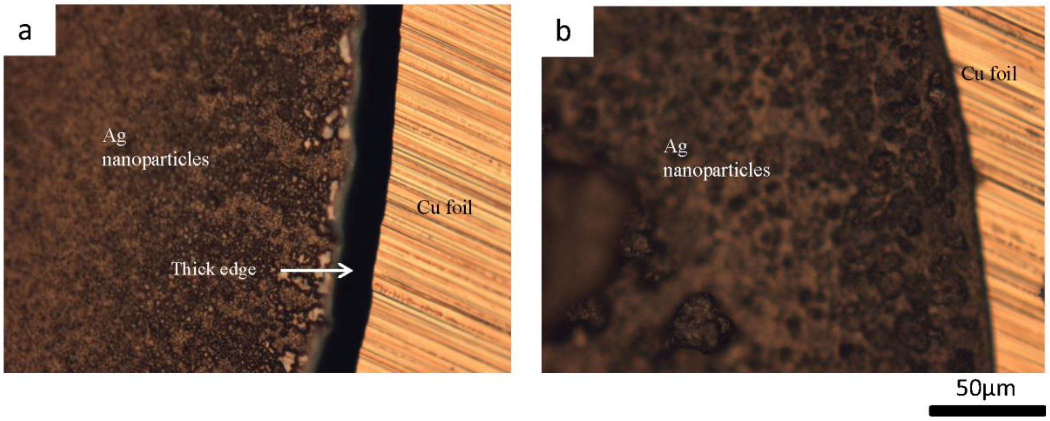

Fig. 4.8 A top view of the distribution control of Ag NPs by (a) one deposition and (b) multiple depositions.

Fig. 4.9 shows cross-sectional SEM images of joints formed with 50-μm Cu wires at 433 K and 473K. The joint formed at 433 K showed close contact between the sintered Ag NPs and the wire while there was a remarkable gap between the NPs and the foil except for a small area. The partial joining is not expected to provide a strength that can cause wire fracture, as will be discussed in the shear strength results. Thus, it is reasonable to deduce that some joined areas between Cu foil and Ag NPs broke during preparation of SEM samples. This gap also indicates that the wire–NPs joint was stronger than the foil–NPs joint. At 473 K, there was always close contact between the Ag NPs and Cu at both sides of the joint.

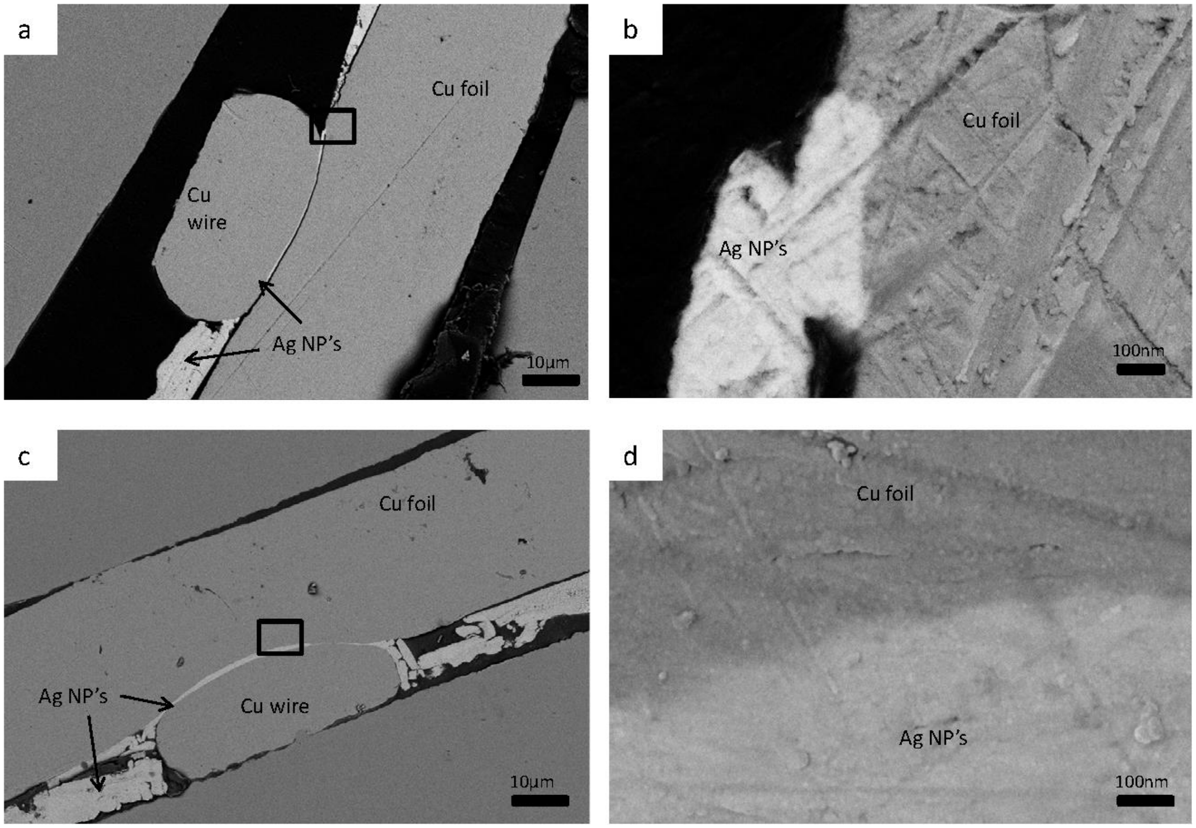

Fig. 4.9 Cross-sectional SEM images of Cu wire bonded to Cu foil (a) at 433 K, (b) higher magnification of (a), (c) at 473 K, and (d) higher magnification of (c).

The SEM images of the bonded samples clearly showed the effect of pressure on the sintering behavior of the Ag NPs compared with pressureless sintering in Figs. 4.5 and 4.7. Under a pressure of 5 MPa, the porosity that was shown in the pressureless sintering disappeared and the NPs formed a bulk layer without distinguishable particle morphology. These images also show clear plastic deformation of the wire and the foil as a result of the 5 MPa applied pressure.

TEM images of the interfaces of a joint bonded at 523 K are shown in Fig. 4.10 between 50-µm Cu wire and Ag NPs, and in Fig. 4.11 between Ag NPs and Cu foil. Close contact at the lattice level between Ag and Cu is shown in Figs. 4.10 (b) and 4.11 (b). These high-resolution TEM images also show that both Cu wire and Cu foil are nanocrystalline. This may have had enhanced the diffusion process with the Ag NPs. The dark areas on both sides of the interface were caused by the nonuniform thickness of the TEM sample.

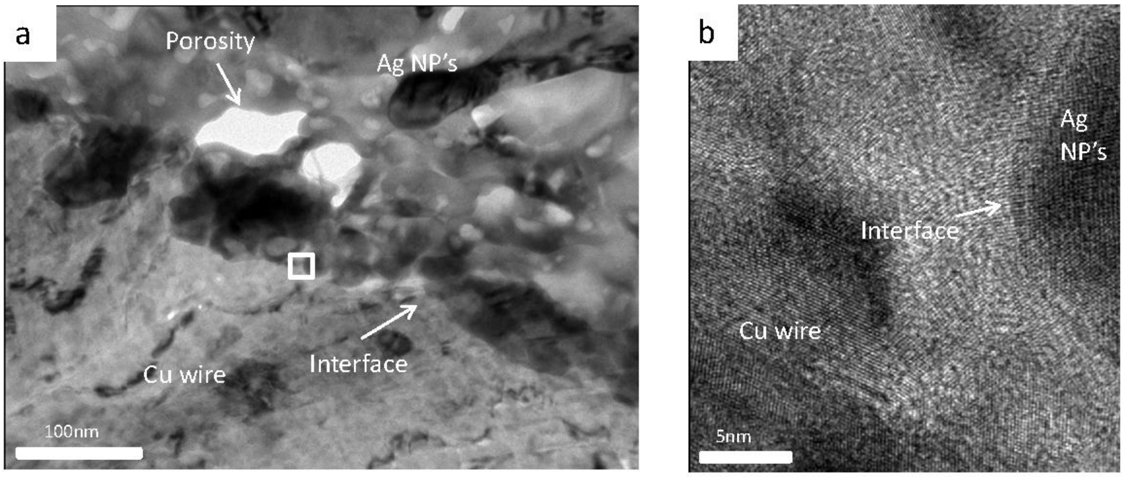

Fig. 4.10 TEM images of Cu wire–Ag interface (a) at low resolution and (b) at high resolution.

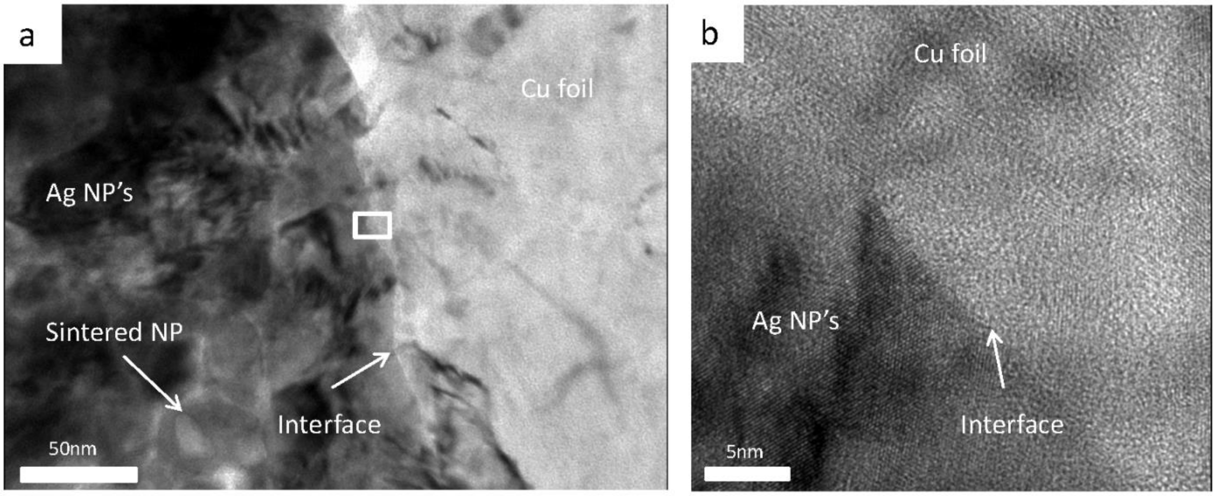

Fig. 4.11 TEM images of Cu foil–Ag interface (a) at low resolution and (b) at high resolution.

The previously reported microstructure analysis of the bonds formed by Ag NPs showed a distorted layer of about 3 nm between lattices of Ag and Cu [7,8,13] . The presence of the distorted layer in the current work cannot be confirmed due to the nanocrystalline nature of the NPs, the foil, and the wire.

4.1.3 Shear Strength and Electrical Resistivity

The lowest temperature at which a bond could be formed was 433 K, which is the same temperature at which the organic shell decomposed. Table 4.1 presents the average shear strength of the bonded samples for Cu wires of three different diameters. The coefficient of variation is calculated by dividing the standard deviation by the average shear strength value. All measurements were carried out at RT except one set of tests performed at 523 K for 250-µm wire bonded at 473 K. Shear tests of 50-µm Cu wires resulted in wire fracture for all bonding temperatures. Thus, under pure shear load, 433 K provides sufficient joint strength that the wire fractures before the joint. This is an even lower temperature than the lowest reported bonding temperature of 523 K [7,8,13].

Table 4.1 Shear strength of the joints.

Wire diameter (µm)	Bonding temperature (K)	Average shear strength (MPa)	Coefficient of variation	Fracture type
50	413	0	0	Joint
50	433	2.8	0.26	Wire
50	473	3.2	0.38	Wire
50	523	2.5	0.17	Wire
250	473	4.2	0.13	Joint
250	473*	7.0	0.13	Wire
250	523	11.9	0.06	Wire
500	473	3.9	0.12	Joint
500	523	17.3	0.15	Joint
500	573	21.9	0.02	Joint

*Tested at 523 K.

If the fracture occurs at the wire, the measured shear strength is actually the critical tensile strength of the wire, which is less than the real shear strength of the joint. To examine the real strength of the joints, 250-µm and 500-µm wires were tested. The 250-µm wire showed joint fracture at 473 K and wire fracture at 523 K. For 500-µm wire, joint fracture occurred at 473 K, 523 K, and 573 K, and the joint strength increased as the bonding temperature increased due to enhanced sintering of NPs at higher temperatures. This trend could not be observed with the 50-µm wire since the fracture occurred at the wire for all bonding temperatures. It is important to mention that wire fracture is based on the joint area achieved by the bonding method explained in chapter 3, larger joint area may instead lead to joint fracture.

Although the bonds formed below 523 K had very low shear strength values (Table 3.1), they are strong enough to break the 50-µm wire. Besides, for thicker wire, higher bonding temperature is recommended. The reported shear strength values of joints formed by Ag NPs were 27 MPa at 523 K [8] and 36 MPa at 573 K [13]. Although these shear strength values are higher than the values obtained here for the same bonding temperature, previous work on bonding below 523 K was unsuccessful.

Shear tests were also performed at temperatures above the bonding temperatures to examine joint reliability at higher operating temperatures. Table 4.1 shows that a bond formed with 250-µm wire at 473 K had higher shear strength when tested at 523 K than when tested at RT. This clearly indicates that these bonds do not degrade at temperatures above the bonding temperature. The increase in strength is due to enhanced sintering of Ag NPs at the testing temperatures.

The contact resistivity showed no dependence on the bonding temperature and has a value around $8.71*10^{-6}$ Ω.m. The joints were good enough at all bonding temperatures to show no difference in the resistivity values.

4.2 Summary

SEM images showed significant increase in the concentration of the Ag NPs in the paste compared to the sol. Raman spectroscopy and TGA analysis of the bonding paste showed that the Ag NPs are coated with an organic shell of citrate group that decompose at 433 K. The TEM examination of the NPs has confirmed the presence of an organic shell of 1 nm thickness. Pressureless sintering of the Ag NPs for 30 min at different temperatures has shown enhanced sintering as the temperature is increased from 373 K to 575 K. Neck growth was also observed during the first 5 min of pressureless sintering of the Ag paste at 473 K

The bonds are formed under a pressure of 5 MPa by solid state sintering of individual Ag NPs as well sintering of the Ag NPs on the Cu wire and Cu foil. TEM examination of the interface has shown that the wire and the foil were metallurgically bonded by the Ag NP paste. It has also shown that both the foil and the wire are nanostructured, which may have enhanced the diffusion process during sintering.

Strength of joints formed with Cu wires of three different diameters (25 µm, 50 µm, and 250 µm) was examined by shear tests. Joints that were formed by the 25 µm experienced wire fracture at all bonding temperatures. The joint formed by the 500 µm wires showed joint fracture at all bonding temperatures with an increase in the average shear strength values as the bonding temperature is increased. The shear strength of the bonds formed at 473 K with the 250 µm showed higher values when tested at 523 K than when tested at RT.

4 DETERMINATION OF COMPLETE MELTING AND SURFACE PREMELTING POINTS OF Ag NANOPARTICLES BY MOLECULAR DYNAMICS SIMULATION

Complete melting points (T_m) of Ag NPs obtained experimentally have shown scattered data in the range of 383 K to 953 K [194-199] while the only published MD simulation was performed on very small clusters with 12-14 atoms [200]. Furthermore, the diversity of the analytical models found in literature for determining T_m and the different results obtained from them certainly makes it difficult to correctly predict T_m of NPs. In this chapter, a previously developed linear scaling parallel MD code [165] is used to find T_m and T_{sm} for individual FCC truncated octahedral Ag NPs in size range of 4 nm to 20 nm. It was possible by this code to utilize multiple processors simultaneously and hence simulating large sizes of NPs. T_m and T_{sm} are determined based on the potential and kinetic values of the atoms, as well as the atomic plots of the NPs. The obtained values of T_m and T_{sm} are compared to the results obtained by other theoretical models. Parts of the research reported in this chapter were published in *Journal of Physical Chemistry C* [201].

5.1 Results

5.1.1 Melting of 18 nm Ag Particle

Fig. 5.1 (a) shows the relationship between average potential energy (PE) of atoms in the NPs versus temperature for an 18 nm particle. It can be clearly seen that the PE curve passed through three stages. In the first stage, a gradual increase of the PE was seen between points A (292 K) and C (1086 K) as the temperature of the NP increased. The second stage started at point

C and ended at point I (1251 K) with a higher rate of increase than the first stage within a shorter range of temperatures. The third stage started at point I, at which the slope of the PE curve decreases but is still slightly higher than the slope of the first stage. Fig. 5.1 (b) shows the atomic arrangement of the NP at different temperatures by cutting a cross section at the centre of the NP with a thickness of three atomic layers (0.6 nm), which is enough to identify the crystallographic planes across the NP. By relating the PE curve with the cross sectional images of the NP, the crystallographic planes were found to be clear through the NP during the first stage of the curve indicating a solid phase. Point C is the beginning of the second stage at which amorphous regions started to appear on the surface as indicated by arrows. These regions are amorphous since the atomic coordinator does not display any long range orders with them. As provided in literature [20], an amorphous region is determined as a quasi-liquid phase if its transport properties are in between solid and liquid. As further discussed below in the discussion of Fig. 5.2 and Fig. 5.4, the identification of the liquid and the quasi-liquid phases was based on PE and KE plots of the surface layers. These quasi-liquid ponds grew and coalesced as the temperature increased to point D (1121 K) at which a nearly full quasi-liquid layer was formed except for small regions indicated by arrows. A contiguous quasi-liquid layer of 1.9 nm thickness was formed at point E (1128 K) and reached a thickness of 5 nm as the temperature increased to F (1193 K). At this point, the outer 1.8 nm layer converted into liquid while the rest of the amorphous layer remained in the quasi-liquid phase. The minimum thickness that can be considered as a liquid is 1.8 nm and is equal to about 9 atomic layers, where the thickness of a single atomic layer is equal to half of the lattice parameter for FCC material [202]. Both liquid and quasi-liquid layers expanded to the core and completed the melting process as the temperature is increased toward points G (1222 K), H (1234 K), and I (1251 K), which stands for the end of the second stage on the PE curve. Since the PE is an average value of all atoms, the dramatic increase of the PE values during the second stage is attributed to the continuous conversion of solid-like atoms to quasi-liquid like atoms and then to liquid-like atoms. Therefore, T_{sm} and T_{m} of NPs have been determined at the temperature at which the PE or KE dramatically changed its slope.

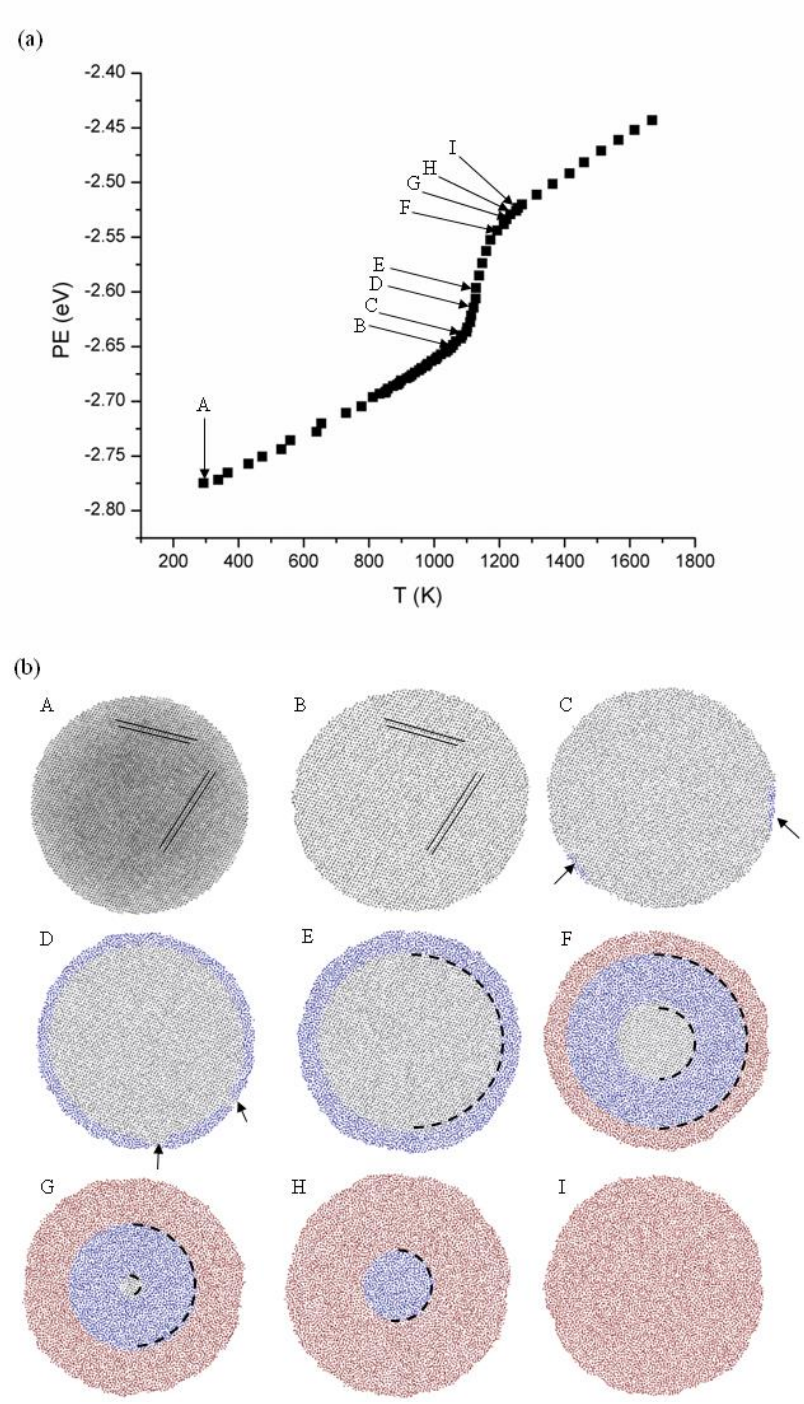

Fig. 5.1 **(a) Potential energy (PE) values during heating of 18 nm Ag particle. (b) Atomic arrangement of the 18 nm Ag particle at different temperatures indicated by letters on the PE curve. Atoms are represented by dots. The lines in the atomic plot of point B represent the orientations of the crystallographic planes. Arrows on plot C point toward quasi-liquid ponds. Arrows at plot D point toward solid regions at the surface. Each color in the atomic plots represent a phase (grey: solid, blue: quasi-liquid, red: liquid) and the dashed arcs represent the interfaces between these phases.**

Fig. 5.2 shows the average PE of surface atoms of the outermost layers of the 18 nm particle during heating. These curves showed a similar trend to the average PE of all atoms in Fig. 5.2 except for the second stage. The outer 1 nm and 1.8 nm surface layers showed two peaks at the melting stage. The first corresponds to the transition of the layer from solid to a quasi-liquid phase while the second indicates transition to a liquid. The decrease of PE values after reaching these peaks was interpreted as due to the conversion of the PE to KE instantaneously after phase transition. These two peaks merged into a single kink once the thickness of the quasi-liquid layer reached 5 nm and the outer 1.8 nm layer converted to liquid, at which the liquid layer was formed before the average potential energy was further decreased.

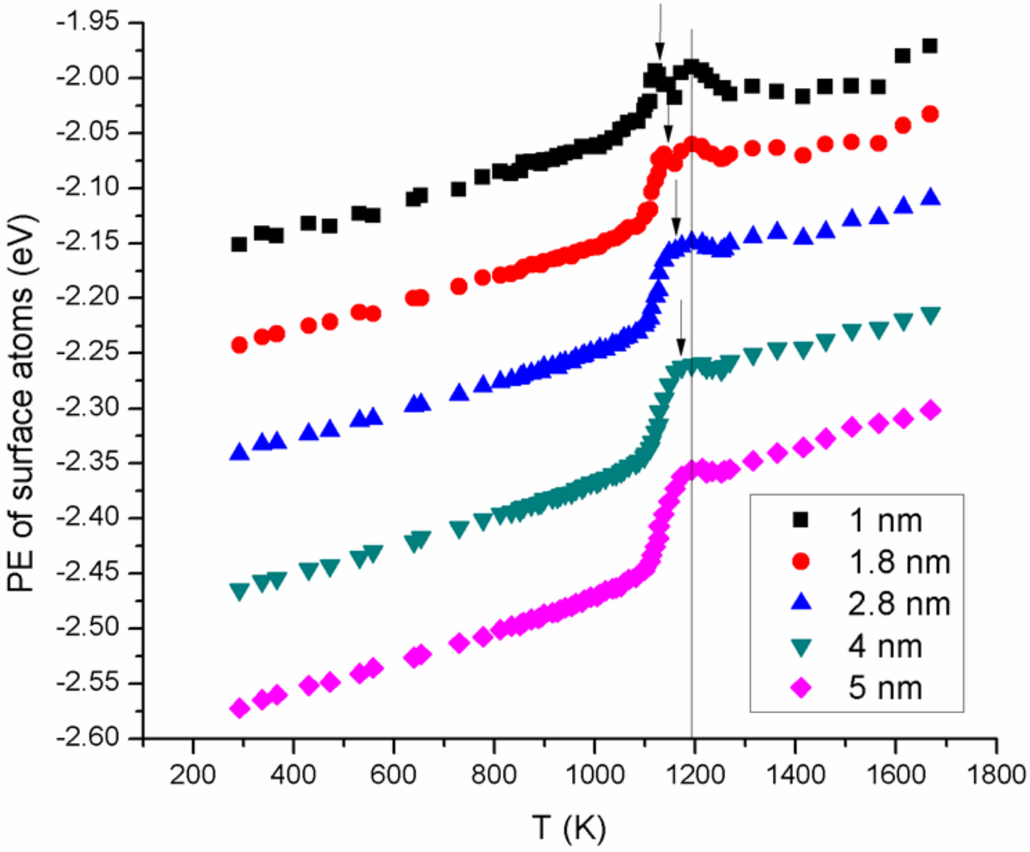

Fig. 5 2 Potential energy (PE) values of the outer layer of 18 nm particle with different thicknesses during the heating process. The arrows show the temperature at which the layer transits to quasi-liquid phase. The vertical line shows the point at which the 1.8 nm liquid layer is formed.

Fig. 5.3 shows the average kinetic energy (KE) of atoms in each 0.2 nm layer starting from the center to the surface of an 18 nm particle at different temperatures during melting. The KE values showed constant values across the NP during the solid and the liquid phase at 1021 K and 1251 K, respectively. At 1099 K and 1114 K, the KE values started a gradual decrease toward the surface due to the increase of the PE values before the first kink in Fig. 5.2. At 1127 K, the KE values of outer 0.8 nm started to increase and are associated with the formation of 0.8 nm amorphous layer and a decrease in the PE values after the first kink in Fig. 5.2. As the temperature is increased to 1160 K, the KE values increased and kept higher values at the outer layers. The outer layers started to have a constant value at 1193 K indicating the formation the liquid layer at the surface and solid phase in the inner layers. The quasi-liquid layer connects the solid and the liquid layers with a gradient increase in KE values.

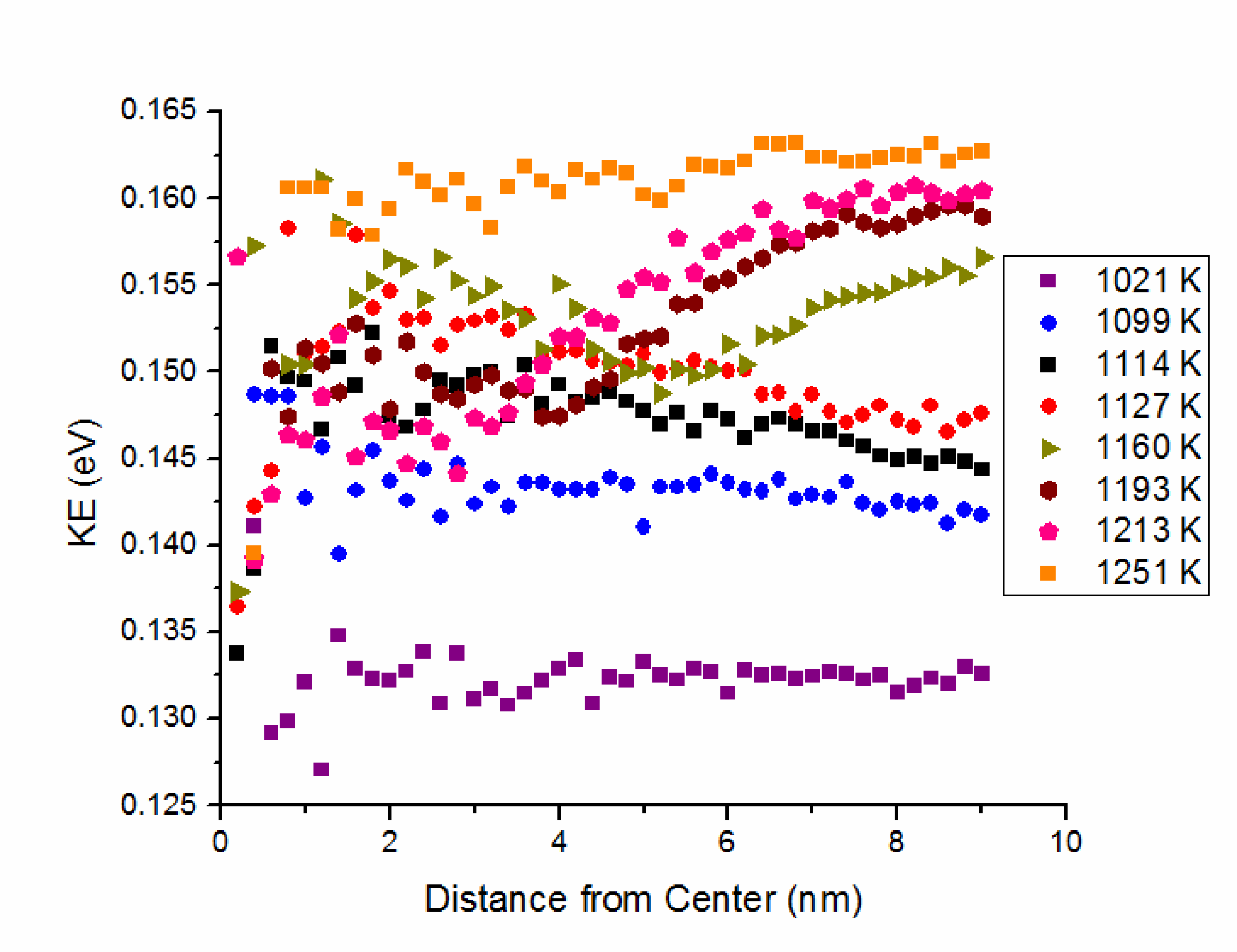

Fig. 5 3 Average kinetic energy (KE) of atoms in each 0.2 nm layers of 18 nm particles at different temperatures. Error bars were eliminated due to their interference with the average value of KE of other temperatures.

Fig. 5.4 shows the borders between different phases during the melting process. Only KE values of outer layers that showed stable states in temperature range of 1114 K to 1213 K were plotted while the KE values of the inner unstable layers were eliminated from the plot. Kinetic energy (KE) values of these unstable layers did not display a minimum (a stable state) prior to transition to quasi-liquid phase and therefore they resided in the quasi-liquid region although they were solid. At 1127 K, the KE values of outer layers started to increase and transit to the quasi-liquid regions. Although the temperature of the NP was increased by increasing total KE of all atoms as shown in equation (3.5), only KE of outer layers increased and the heat was not transferred to the inner layers. This can be attributed to free vibration of the surface atoms and the larger bond length between atoms at the inner layers [203]. The figure shows that the thickness of the quasi-liquid layer increased as the temperature increased to 1160 K. At 1193 K (point F in Fig. 5.1), which is the same temperature of the second peak in Fig. 5.2, the quasi-liquid layer thickness reached 5 nm and the outer 1.8 nm layer became constant as an indication of forming the first liquid layer with critical thickness (t_o = 1.8 nm). The 5 nm can thus be considered as the minimum thickness of a quasi-liquid layer that allows the outer 1.8 nm layer to transit to liquid without having a high interfacial energy with the solid core. The border line between the liquid and quasi-liquid phases is specified at the KE value of the 1.8 nm liquid layer. The thickness of the liquid layer increased as the temperature increased and completed the melting process at 1251 K (point I in Fig. 5.1), which is higher than T_m of the bulk (1234 K). As it will be discussed below, slower heating rate would reduce T_m of the 18 nm particle to 1210 K.

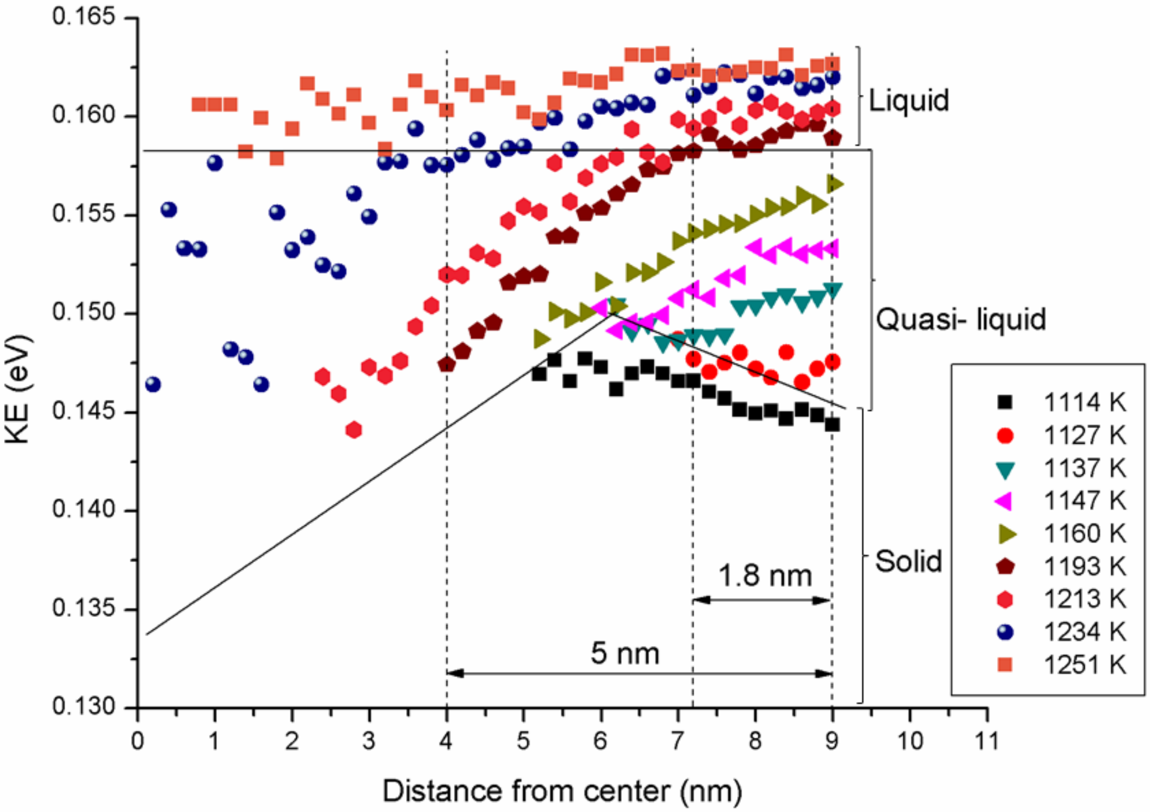

Fig. 5.4 Average kinetic energy (KE) of atoms in each 0.2 nm layers of 18 nm particles at different temperatures. The lines show the borders between different phases. KE values of inner layers at the lower temperatures were eliminated. Error bars were also eliminated due to their interference with the average value of KE of other temperatures.

Fig. 5.5 shows the relationship between the thicknesses of the quasi-liquid and the liquid layers during the heating process. In the range of temperatures between 1086 K and 1128 K (points C and E in Fig. 5.1), quasi-liquid ponds were formed on the surface. The first contiguous quasi-liquid layer was of 1.9 nm thickness and was formed at 1128 K (point E in Fig. 5.1) as indicated by the arrow on the figure. The first formed liquid layer was of 1.8 nm thickness and was formed at 1193 K (point F in Fig. 5.1) at which the quasi-liquid layer reached 5 nm thickness. As shown in the figure, the increase in the thicknesses of the quasi-liquid and liquid layers could be fitted by parabolic curves.

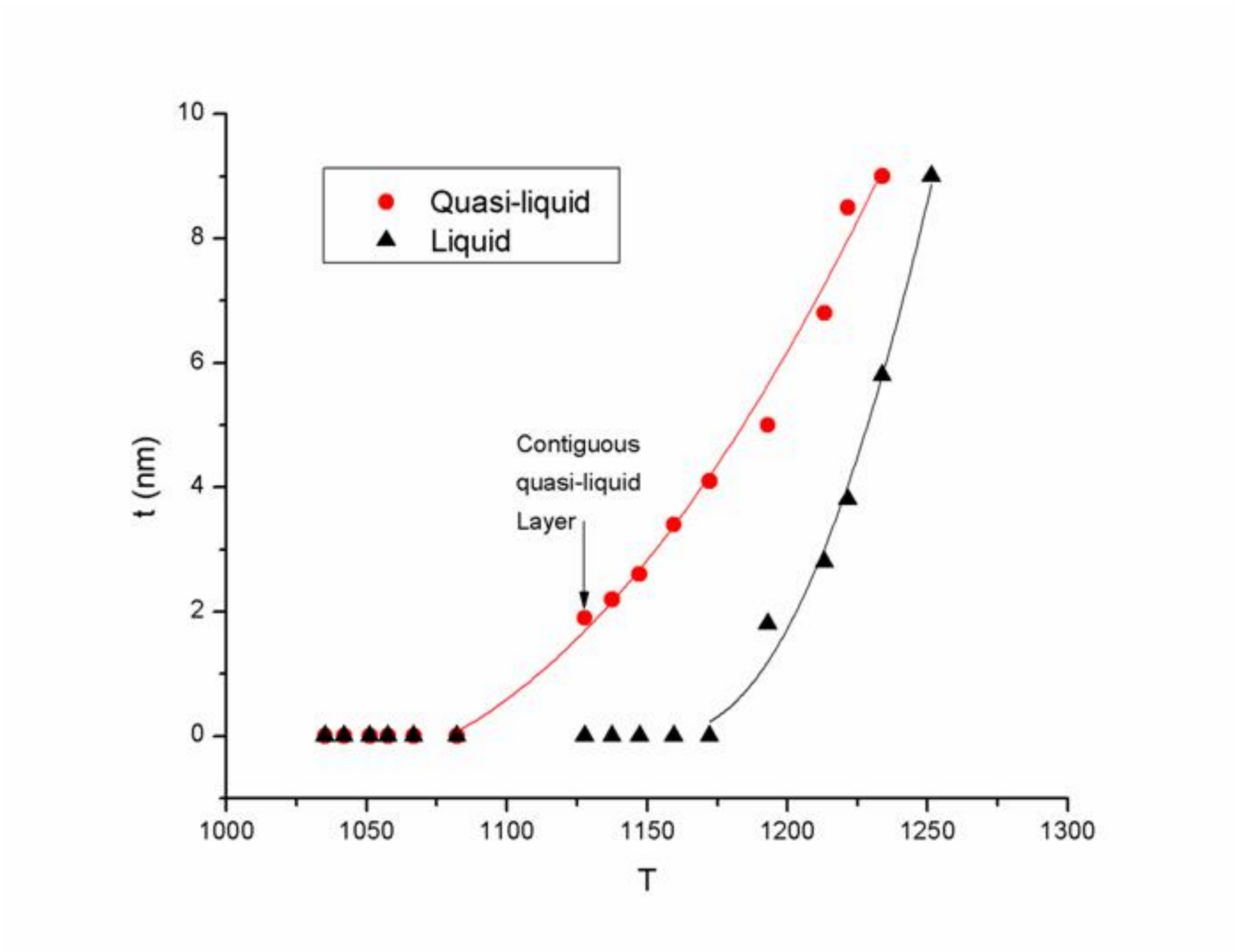

Fig. 5.5 Thicknesses of quasi-liquid and liquid layers during the heating process of 18 nm particle. The arrow points to the first contiguous quasi-liquid layer. The curves show parabolic fit of thicknesses of quasi-liquid and liquid layers.

5.1.2 Melting of 6 nm Ag Particle

As shown in Fig. 5.6 (b), melting of a 6 nm Ag particles started by forming quasi-liquid regions on the surface at which moved towards the core. The atomic plots were obtained by showing three atomic planes at the center of the NPs at different temperatures. Unlike the 18 nm particle, quasi-liquid and liquid layers did not reach equilibrium with the solid core and expanded towards inner atoms to complete melting at one temperature as shown by the PE values in Fig. 5.6 (a).

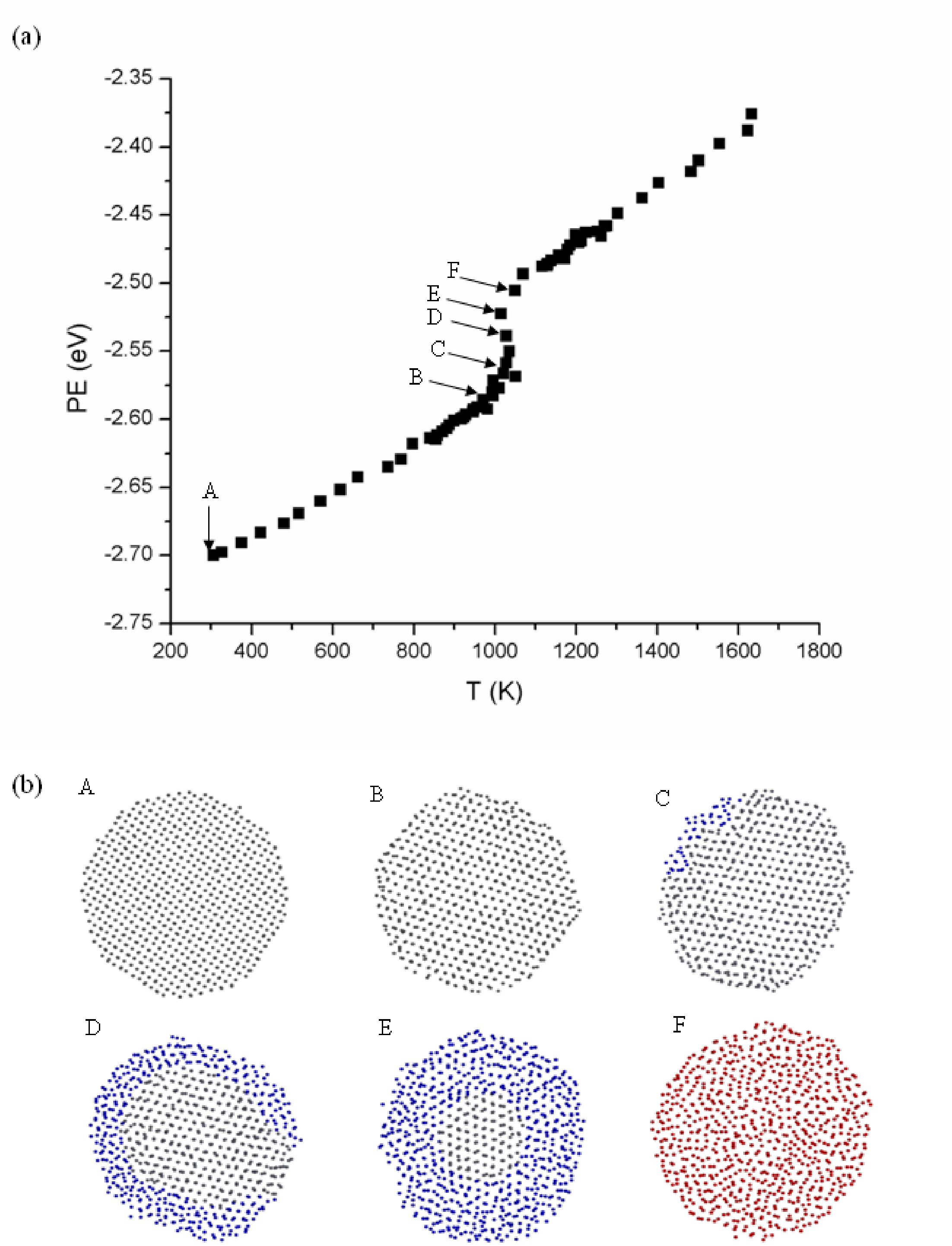

Fig. 5.6 (a) Potential energy (PE) values during heating of 6 nm Ag particle. (b) Atomic arrangement of the 6 nm Ag particle at different temperatures shown by letters on the PE curve. Atoms are represented by dots. Each color in the atomic plots represents a phase (gray: solid, blue: quasi-liquid, red: liquid).

5.1.3 Melting Kinetics of Ag Nanoparticles

Fig. 5.7 shows the average PE of the atoms in the NP versus temperature for different sizes of Ag NPs. PE curves passed through the three stages explained above in Fig. 5.1 with increasing PE values as the NP size decreased. The second stage of the PE curve for 7 nm and smaller particles showed a vertical increase of the PE. This means that T_{sm} and T_{m} are equal and surface premelting did not occur for these NPs. This confirms the previous theoretical studies that suggested that surface premelting does not take place if the radius of the NP is smaller than a critical radius (r_{c}) (3.62 nm for Ag) [103].

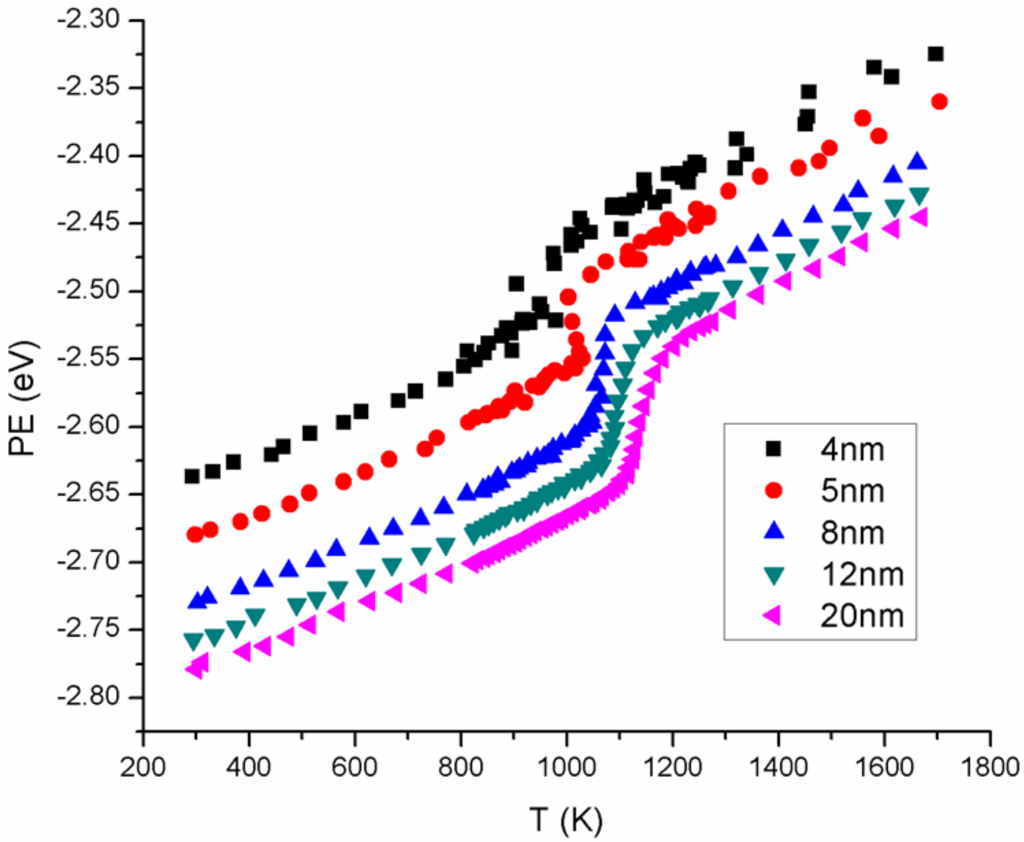

Fig. 5.7 Potential energy (PE) values of different sizes of Ag nanoparticles during the heating process.

Fig. 5.8 shows the average KE of atoms in each 0.2 nm layer starting from the center of the NP towards the surface at the temperature at which the liquid layer was formed. Horizontal lines correspond to the minimum KE of liquid atoms. The thickness of the liquid layer formed on the 20 nm particle was 1.8 nm and this was found to apply to other NPs in the size range of 8 nm to 18 nm. The thickness of the quasi-liquid layer which allowed the outer 1.8 nm to transit to liquid was found to be 5 nm and this applied to the size range of 12 nm to 20 nm and equal to radius of the NP for 8 nm to 10 nm particles. Kinetic energy (KE) values of 4 nm and 6 nm particles showed a constant value, which is evidence of melting at a single temperature.

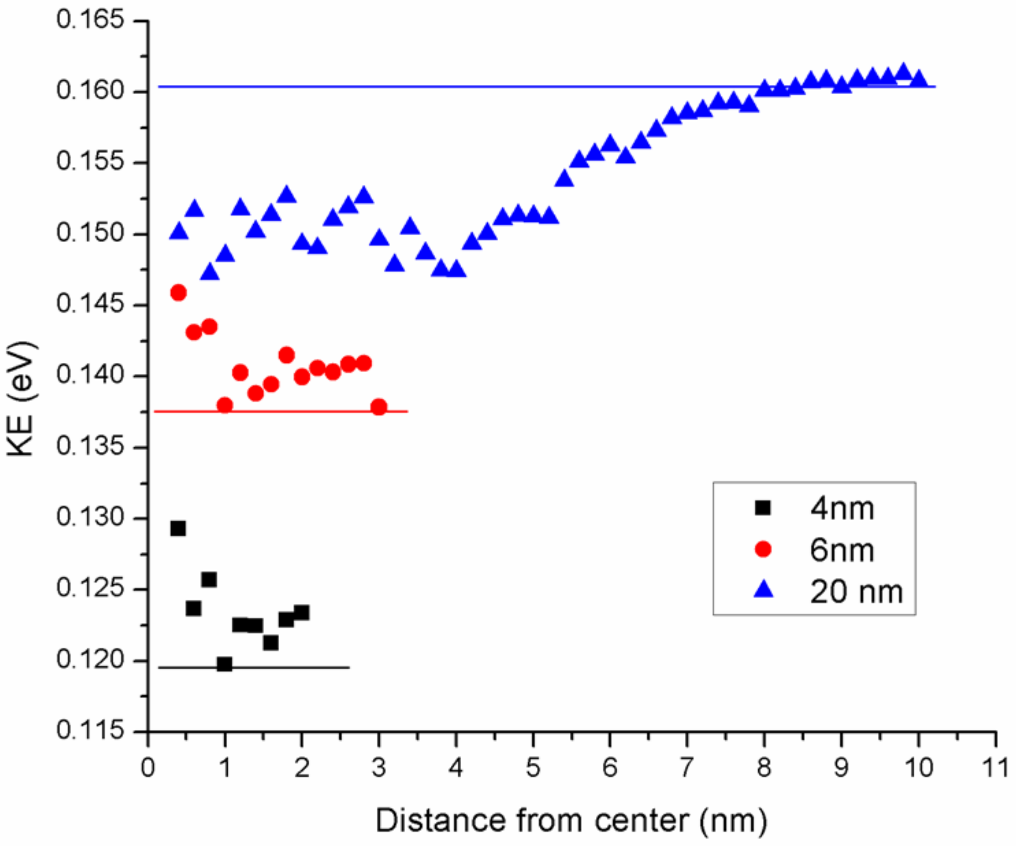

Fig. 5.8 Average kinetic energy (KE) of atoms in each 0.2 nm layer for different sizes of nanoparticles at the temperature at which the liquid layer forms at the surface. The horizontal lines show the border between liquid and quasi-liquid regions at each size. Error bars were eliminated due to their interference with the average value of KE of other temperatures.

As shown in Fig. 5.9, the ratio of quasi-liquid shell thicknesses to the NP radius was found to have a linear relationship with temperature during the surface prermelting stage. The slope of the relationship moved toward a vertical line within a shorter temperature range as the NP size decreased to 8 nm, the minimum size at which the surface premelting occurred. The figure shows that the quasi-liquid layers were stable and in equilibrium with the solid core. Further increase in temperature broke this equilibrium and the thickness of the quasi-liquid layers increased as the temperature of the NP increased. These equilibrium points did not exist for particles smaller than 8 nm. Instead, the whole particle melted at a single temperature.

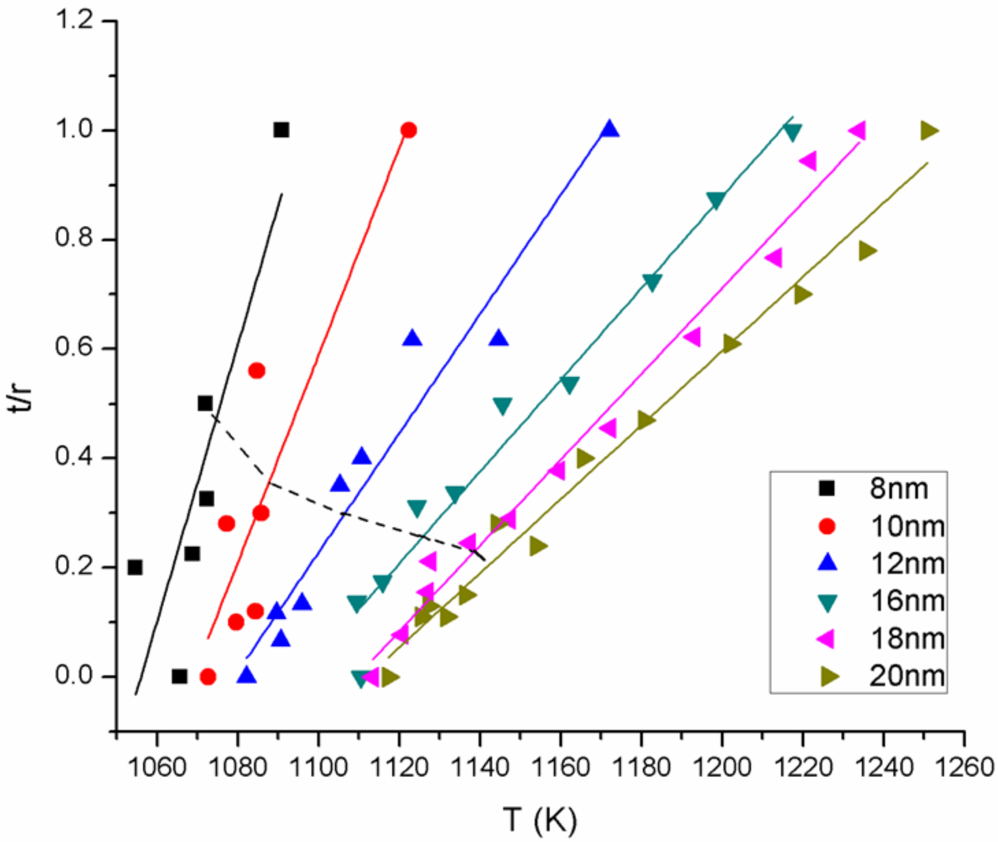

Fig. 5.9 Relationship between the ratio of the quasi-liquid layers thickness to the radius of the nanoparticle and temperature. The lines show a linear fit of the data at each nanoparticle size. The dashed line intercepts the data at the critical thickness (t_o = 1.8 nm).

5.1.4 Complete Melting and Surface Premelting Points of Ag Nanoparticles

Complete melting points (T_m) and surface premelting points (T_{sm}) obtained in this study are compared to the theoretical models in Fig. 5.10. Surface premelting points (T_{sm}) showed values lower than T_m for 8 nm and larger particles and the gap between T_m and T_{sm} increased as the NPs size increased. Fig. 5.10 also shows that surface premelting did not occur for NPs smaller than 8 nm. Complete melting point values obtained here are in good agreement with the liquid drop model and Shi's model for NPs smaller than 8 nm and with Hanszen's model for 8 nm, 9 nm, and 10 nm particles. Complete melting points (T_m) of larger NPs started to deviate from Hanszen's model and approached T_m of the bulk.

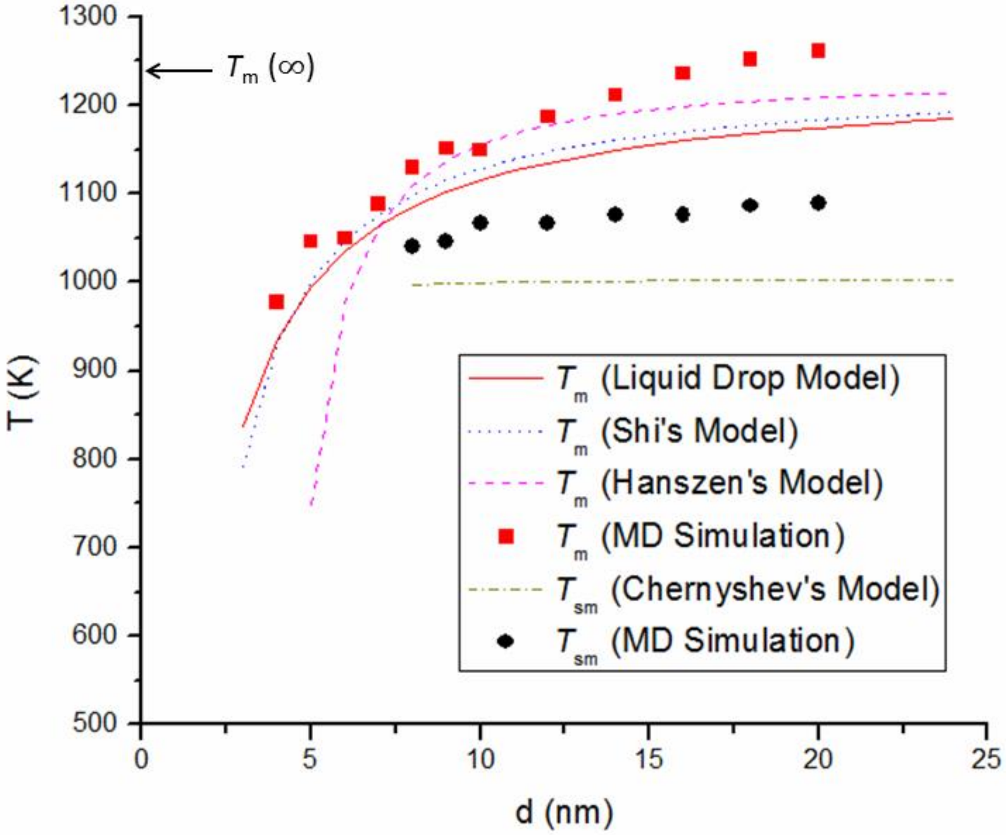

Fig. 5.10 Complete melting points (T_m) and surface premelting points (T_{sm}) of different sizes of Ag nanoparticles determined by MD simulation and by the other theoretical models.

5.1.5 Freezing and Reheating of 4 nm Ag particle

Freezing of the 4 nm particle is studied to find possible thermal hysteresis between melting and freezing. Fig. 5.11 (a) shows the PE values during the heating process of the original FCC truncated octahedral particle followed by cooling and reheating. Atomic arrangements of three atomic planes at the center of the NP during the cooling and reheating process are plotted in Fig. 5.11 (b). Plot A shows the particle in liquid state at (1698 K), which is the last temperature of the first heating cycle of the FCC truncated octahedral particle and the starting point of the cooling process. The NP remained in the liquid phase at point B (683 K) and started to freeze at point C (663 K) by forming the surface facets of the NP. The freezing process occurred at a range of temperatures and ended by forming a polycrystalline configuration at point E (470 K). The slope of the PE values decreased during the freezing process due to continuous conversion of liquid like atoms to solid like atoms. The polycrystalline configuration remained stable at the end of the cooling process at point F (299 K). The PE values of the reheating process followed the same path as the cooling values until point D (513 K), at which the NP remained in the solid phase. Quasi-liquid regions appeared on the left side of the NP at point H (906 K) and completed the melting process at point I (906 K), which is higher than the freezing temperature (470 K) and slightly lower than T_m of the FCC truncated octahedral particle (977 K). Thermal hysteresis between melting and freezing was also observed in amorphous NPs [204]. Unlike melting, freezing of the 4 nm particle has occurred over a temperature range and not at one single temperature.

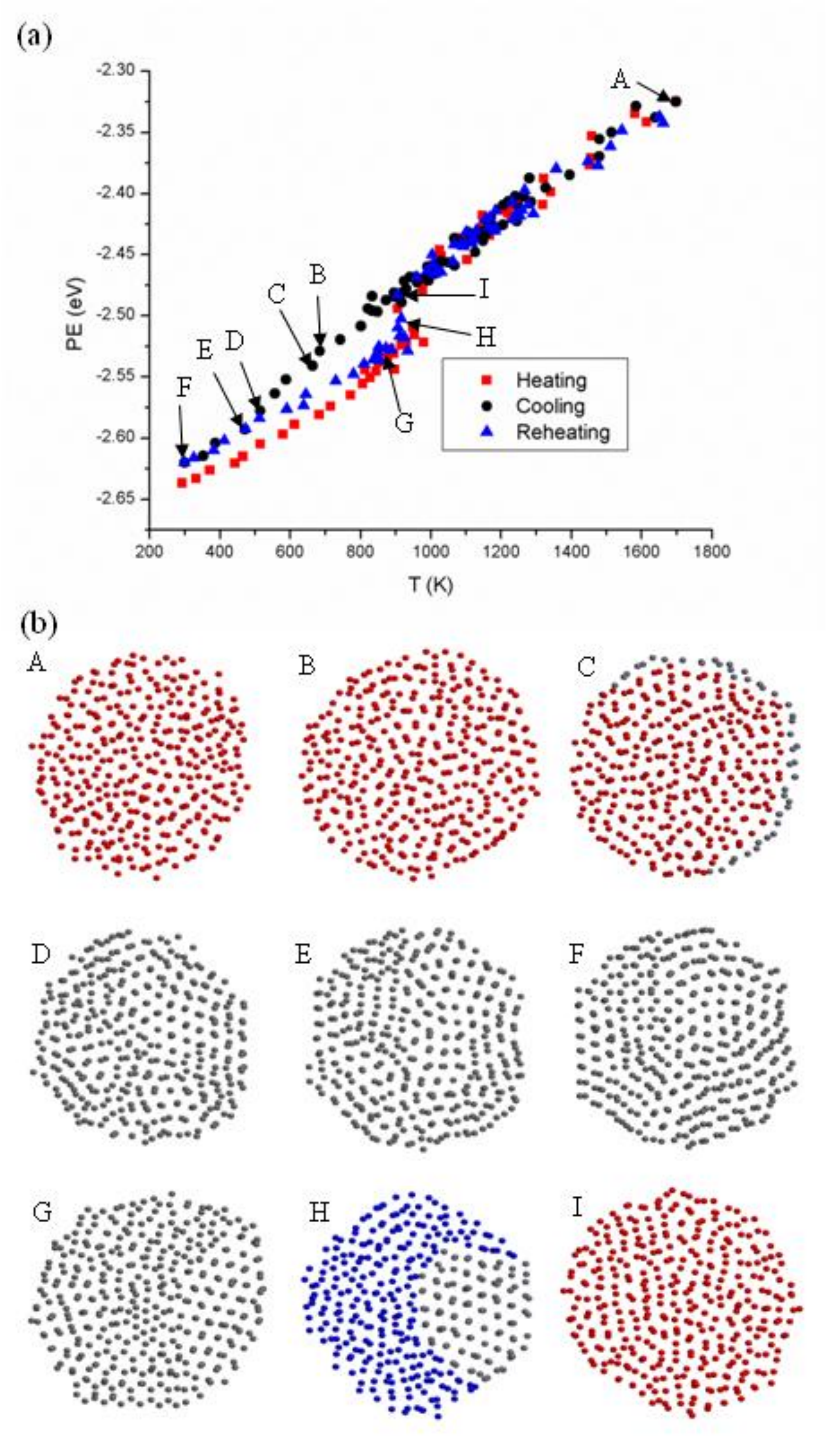

Fig. 5.11 (a) Potential energy (PE) values during heating, cooling, reheating of a 4 nm Ag particle. Arrows over the values head toward cooling points while the arrows below the values head toward reheating points. (b) Atomic arrangement of the 4 nm Ag particle at different temperatures showed by letters on the PE curve. Atoms are represented by dots. Each color in the atomic plots represent a phase (grey: solid, blue: quasi-liquid, red: liquid).

5.1.6 Effect of Heating Rate

Results in this chapter are based on the heating rate specified in section 3.2. Fig. 5.12 shows PE values during heating of the 18 nm particle with a 5 K temperature steps between 825 K and 1275 K compared to the original heating rate of 10 K temperature steps in the same temperature regime. The slower heating rate did not affect the T_{sm} value but reduces the T_{m} value from 1250 K to 1210 K. Thus, superheating of the 18 nm particle occurred due to the heating rate used in this study. For more accurate determination of T_{m} in future work, slow heating rate especially in the region between T_{sm} and T_{m} should be applied.

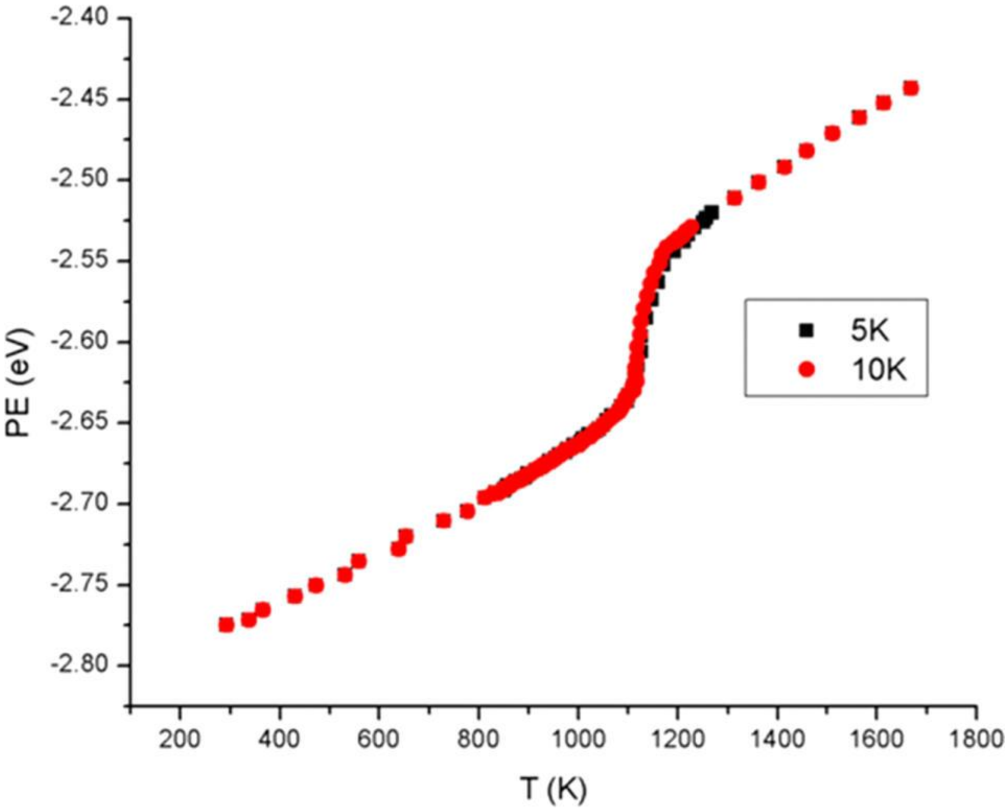

Fig. 5.12 Potential energy (PE) values during heating of 18 nm Ag particle at two different temperature steps in temperature regime of 825 K to 1275 K.

5.2 Discussion

The liquid drop model and Shi's model have ignored the effect of the formation of a liquid shell in their equations and assumed homogeneous melting of the NPs without passing through the surface premelting stage. This is the reason behind the agreement between both models and results obtained here for NPs that are smaller than 8 nm since surface premelting was not observed at those smaller particles. For 8 nm and larger particles, the MD results showed higher complete melting points than those expected by both models. Previous experimental results of relatively large Pb, Sn, In, and Bi NPs of sizes in range of 6 nm to 20 nm have also shown higher complete melting points than the liquid drop model [205] and the reason for this was suggested to be the substrate effect on the complete melting point of the NPs [21]. However, the current study shows that the formation of the liquid shell and its effect on the heat transfer within the NP might be another significant reason behind this difference.

Hanszen's model was based on classical laws of thermodynamics and assumed that the melting process begins by forming a thin liquid layer on the surface of the NP. The physical parameter of the liquid layer and the interfacial energies between this liquid layer and both vapour and solid core were introduced in equation (3.13). This is the reason behind the agreement between the results obtained here and Hanszen's model for NPs in size range of 8 nm to 10 nm and the disagreement for smaller particles on which a liquid shell does not form prior to melting. The critical thickness (t_o) of the liquid layer is introduced in equation (3.14) and can be identified by finding the best fit between T_m obtained by equation (3.14) and by the MD simulation. This is the minimum thickness at which the amorphous layer can be considered as liquid, thinner layers are considered as quasi-liquid layers [68]. The best fit of T_m determined by

MD simulation and by equation (3.14) is at a critical thickness (t_o = 1.8 nm), which is the same critical thickness obtained from KE plots in Fig. 5.8. Previous experimental work identified the critical thickness of Ag as 1.01 nm [185] and 2 nm [189].

Complete melting points (T_m) of NPs that are larger than 10 nm started to deviate from Hanszen's model and approached T_m of the bulk due to formation of multiple liquid layers during the melting stages. This is different than Hanszen's assumption that suggested that only one liquid layer of critical thickness (t_o) is formed prior to melting and further increase in temperature would lead to a complete melting of the NP without passing through other equilibrium states. However, the present study agrees with another study that showed that surface premelting of Pb occurred at broad range of temperatures and the thickness of the liquid layer increased as the temperature increased [206].

The only reported relationship between T_{sm} and the size of the NP was the theoretical model developed by Chernyshev [102]. This model defined T_{sm} as the temperature at which liquid ponds started to form on the surface of the NP. Fig. 5.10 showed that T_{sm} values obtained by Chernyshev for Ag NPs of sizes between 8 nm and 20 nm have nearly a constant value of 1000 K. T_{sm} obtained by the MD simulation are higher and increased from 1072 K for an 8 nm particle to 1144 K for 20 nm particle. Unlike Hanszen's model, Chernyshev's model has not considered the quasi-liquid state of the surface atoms.

The presented MD simulation was performed on single NPs with a free surface and a perfect crystal without defects. Lower T_m values obtained experimentally than values calculated here can be attributed to various possible reasons [194-199]. Nanoparticles with higher packing factors or with polycrystalline structure should have a lower T_m than an individual single crystal NP. Ag NPs embedded in silica matrix had T_m values in range of 423 K to 623 K in the size range of 8 nm to 30 nm [194]. Another study showed T_m values of about 700 K for Ag NPs in range of 4 nm to 7 nm and this was explained by uncontrolled oxidation of the NPs [195]. Both effects of embedding matrix and oxidation should increase T_m of the NP due the reduction of surface energy. However, packing factors or the polycrystalline structure may have had a stronger effect and caused a decreased T_m. Other studies also showed very low T_m values of (383 K) for Ag NPs of sizes in range of 8 nm to 25 nm [196-197] and 385 K to 466 K for sizes in range of 3.5 nm to 6.5 nm [198]. It is notable that the onset temperature of thermal sintering is not the complete melting point since solid state diffusion will also occur [38]. The closest T_m values to those obtained here was found for one individual NP studied under TEM with a heating stage and showed values in range of 773 K to 953 K for NPs of sizes in range of 5 nm to 50 nm [199]. In that work, the crystalline structure of the examined particles was not determined. A NP that is surrounded by other NPs might also have much lower T_{sm} value since surface atoms might detach from the NPs and melt during surface diffusion between the NPs [207].A previous experimental work showed local surface premelting of 40 nm Ag NPs at 573 K [152]. The reduction of T_{sm} in this work might also be due to the NP crystalline structure and packing factor.

The many-body EAM used here is the first alternative to the traditional pair-wise potentials, which are usually fitted based on the context of bulk properties within ambient conditions. Thus, transferability of pair-wise potentials might be problematic for systems containing surfaces and interfaces. This problem is not seen in EAM potentials that account for the energy of an embedded atom in a homogeneous electron gas. Nevertheless, any approach in computer simulation will not reproduce experimental findings unless same conditions are mimicked. Though to this fact, it is expected to mimic a realistic trend in the studied system for any thermodynamics and/or structural properties with a well-parameterized many-body potential [208].

5.3 Summary

Melting kinetics of Ag NPs in size range of 4 nm to 20 nm was studied by MD simulation. The determination of complete melting and surface premelting points of the Ag NPs was based on the atomic plots and average PE and KE values. Solid phase showed a crystalline atomic structure while the liquid and the quasi-liquid showed amorphous structure. The transition between solid, quasi-liquid, and liquid phases could be observed by the change in the slopes of average PE and KE values.

The current results showed that 8 nm and smaller Ag particles melted homogeneously and T_m values were found to be in good agreement with Shi's model and the liquid drop model. For 8 nm to 10 nm particles, the MD results showed good agreement with Hanszen's model, at which the melting starts by forming a stable liquid layer of critical thickness (t_o) that expanded to the core as the temperature is increased. Complete melting points of larger NPs are found to deviate from Hanszen's model due to the formation of a thicker stable liquid layer below T_m. It was also found that the ratio of the thickness of the quasi-liquid layer to the radius of the NP linearly increased as the temperature is increased to T_m. The reasons of agreement/disagreement between the results obtained here and the other theoretical models were justified. The minimum thickness at which an Ag amorphous layer can be considering as liquid was determined as 1.8 nm.

6 STABILITY OF FCC TRUNCATED OCTAHEDRAL Ag NANOPARTICLES BY MOLECUAR DYNAMICS SIMULATION

Based on the literature review provided in section 2.3, the stability of different phases of metallic NPs and the transitions between them are still not well understood. In this chapter, the stability of different sizes of FCC truncated Ag NPs as well as the solid phases obtained by freezing liquid droplets are studied toward drawing a phase map of Ag NPs based on the temperature and the size.

6.1 Stability of 1 nm (65 Atoms) FCC Truncated Octahedral Ag Particle

Fig. 6.1 shows PE values and atomic plots during heating and cooling of 1 nm (65 Atoms) Ag particle. Unlike larger particles, the PE values during heating below T_m fluctuated between lower and higher values. Plot A in Fig. 6.1 (b) shows the atomic plots of the initial truncated octahedral configuration. As the NP is relaxed at RT, the NPs transformed into an amorphous configuration at point B. Based on the minimum liquid thickness of Ag determined in chapter 5 (1.8 nm), it is reasonable to deduce that this amorphous NP is in quasi-liquid phase. As the temperature of the NP is increased to point C, the average PE value dropped and the atomic plot showed a solid icosahedral configuration. The PE values keep fluctuating as the temperature is increased due to the transitions between the icosahedral solid and the quasi-liquid phases. The atomic plots of points C to I shows that the icosahedral configuration and the quasi-liquid phase corresponds to the lower and the higher PE values, respectively. The transition between these two phases during heating has been also observed for Ag NP with 13 to 178 atoms and was named as dynamic coexistence melting (DCM) or biastability [209]. The NP stick to the quasi-liquid phase as the temperature of the NP is increased beyond point I. During the cooling cycle, the NP froze into the icosahedral configuration at point M and preserves this structure for the whole cycle. The PE values showed a drop as the quasi-liquid NP freezes and showed stable values as the temperature of the NP is decreased toward point N. As discussed in section 5.1.5 for the 4 nm particle, the difference between melting and freezing points indicates thermal hysteresis.

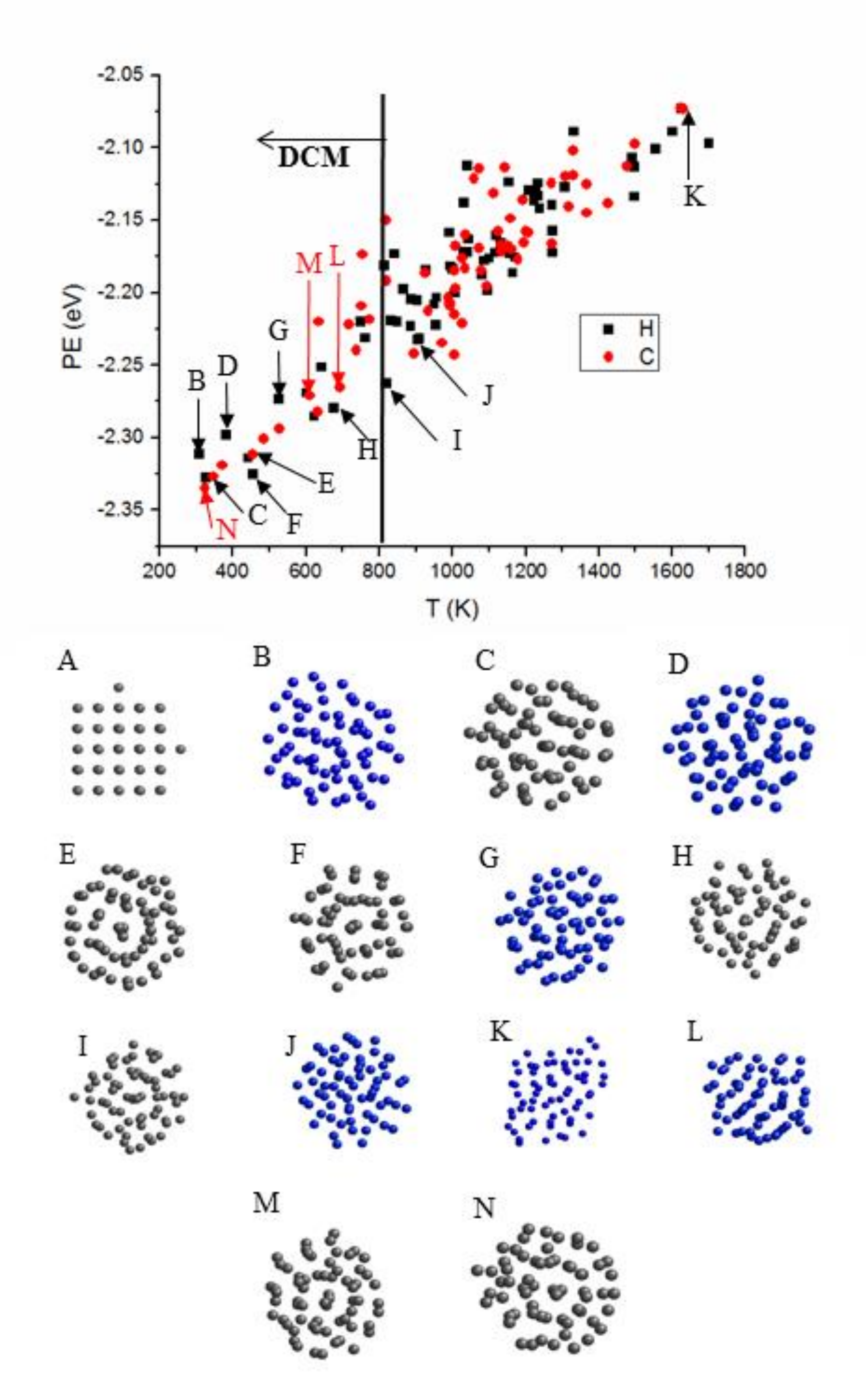

Fig. 6.1 (a) Potential energy (PE) values during heating and cooling cycles of 1 nm (65 Atoms) Ag particle. The vertical line shows the border between DCM and the quasi-liquid phase (b) Atomic arrangement of the particle at different temperatures shown by letters on the PE curve. Atoms are represented by dots. Each color in the atomic plots represents a phase (gray: solid, blue: quasi-liquid).

6.2 Stability of 1.2 nm (138 Atoms) FCC Truncated Octahedral Ag Particle

Fig. 6.2 shows average PE values and atomic plots during the heating and the cooling cycles of 1.2 nm Ag particle. The figure shows two major transitions during the heating cycle. The first is solid to solid phase transition from the truncated octahedral configuration at point B to icosahedral configuration at point C. The second is melting of the icosahedral configuration at point D to the quasi-liquid phase at point E. The solid to solid phase transition indicates that the truncated octahedral phase is not stable far below T_m of the particle. The PE values dropped during this transition, which suggests that the transition were mainly driven by minimization of the total PE of the particle. Similar to other sizes of Ag NPs, the melting process shown by the transition from the icosahedral configuration at point D to the quasi-liquid state at point E has significantly increased the average PE values.

During the cooling cycle, the average PE value has dropped due to the freezing of the NP into the icosahedral shape shown in the atomic plot. The icosahedral phase remained stable as cooling continues to RT and showed lower PE values than the truncated octahedral phase at the beginning of the heating cycle. Therefore, it can be concluded that the icosahedral phase is energetically favorable over the truncated octahedral phase. Thermal hysteresis between melting and freezing is also observed here.

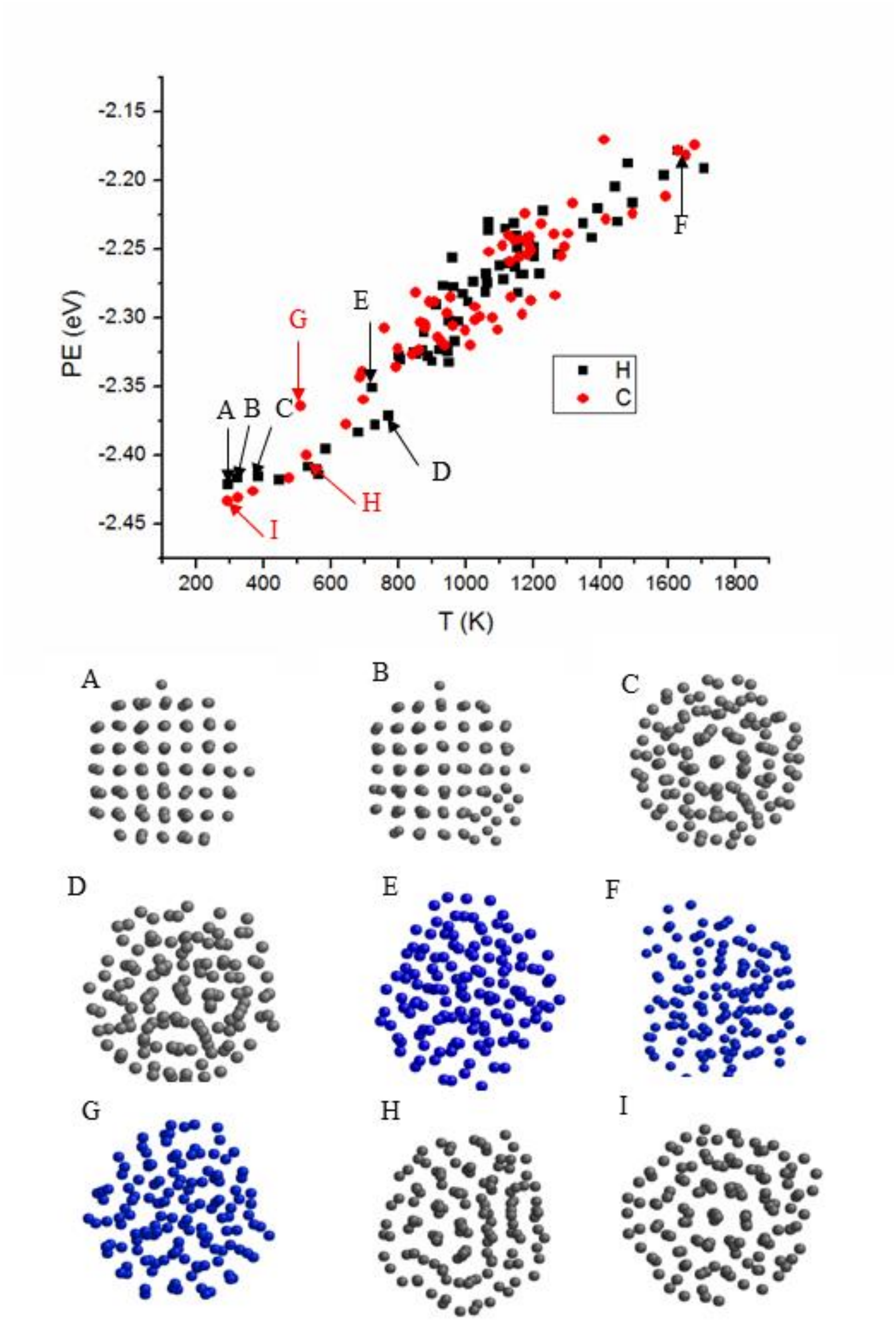

Fig. 6.2 (a) Potential energy (PE) values during heating and cooling cycles of 1.6 nm (138 Atoms) Ag particle. (b) Atomic arrangement of the particle at different temperatures shown by letters on the PE curve. Atoms are represented by dots. Each color in the atomic plots represents a phase (gray: solid, blue: quasi-liquid).

6.3 Stability of 1.8 nm (263 Atoms) and Larger FCC Truncated Octahedral Ag Particles

Fig. 6.3 shows average PE values and atomic plots during the heating and the cooling cycles of 1.8 nm Ag particle. The initial truncated octahedral remained stable during the heating cycle below T_m at point C. Since the diameter of the NP is equal to the minimum layer thickness determined in chapter 5 for a liquid Ag, the amorphous atomic structure at point E can be identified as liquid. During the cooling cycle, the PE values dropped at point F and the nanodroplet froze into an icosahedral configuration with a remarkable drop in the PE values. The icosahedral configuration remained stable as the temperature of the NP is decreased to point G at RT. Thermal hysteresis between melting and freezing is also observed here.

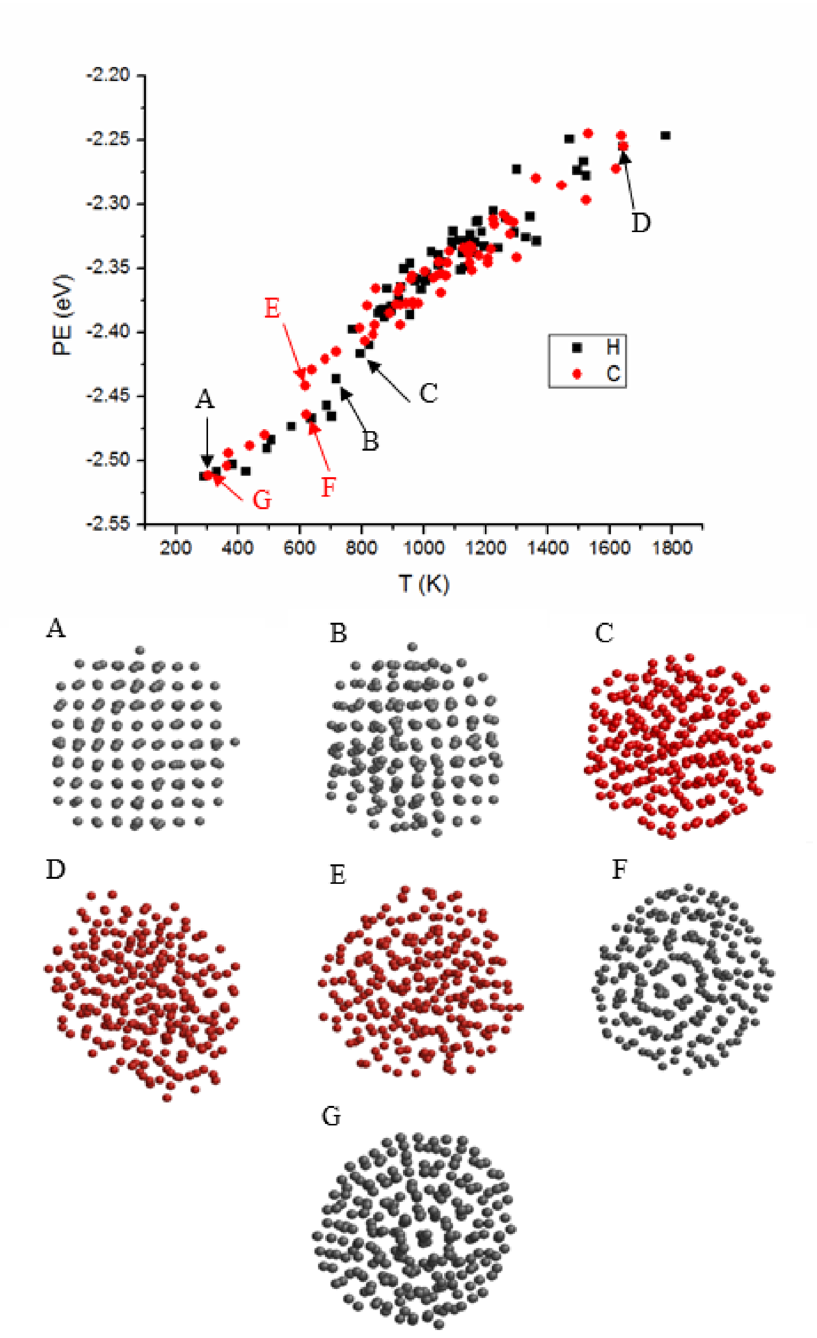

Fig. 6.3 (a) Potential energy (PE) values during heating and freezing of 1.8 nm (263 Atoms) Ag particle. (b) Atomic arrangement of the particle at different temperatures shown by letters on the PE curve. Atoms are represented by dots. Each color in the atomic plots represents a phase (gray: solid, blue: quasi-liquid, red: liquid).

Similar to these small particles, the solid state configuration obtained by freezing 2.3 nm is icosahedra. As previously shown in Fig. 2.12, Baletto et al. has previously shown that Ag NPs in this size range also froze into an icosahedral structure [106-112]. Similar to 1.8 nm Ag particle, the truncated octahedral configuration of all larger particles remained stable during the heating cycle below T_m. Therefore, it can be concluded that FCC truncated octahedral configuration is stable below T_m for 1.8 nm and larger particles.

6.4 Average Potential Energy Values during Heating of 1 nm to 4 nm Ag Particles

Fig. 6.4 shows the average PE values during the heating cycles of all simulated NPs in this chapter and of the 4 nm particle obtained in chapter 5. PE values of all NPs except for the 1 and 1.2 nm particles follows a similar trend as the larger NPs presented in chapter 5, which is characterized by a constant rate of increase during heating at the solid state and liquid state and a jump in PE values in-between them. The 1 nm showed fluctuating values during heating within DCM region determined in Fig. 6.1. The 1.2 nm particle showed a reduction in the PE values during the heating in the solid state region due to the solid to solid phase transition from the truncated octahedral configuration to the icosahedral configuration.

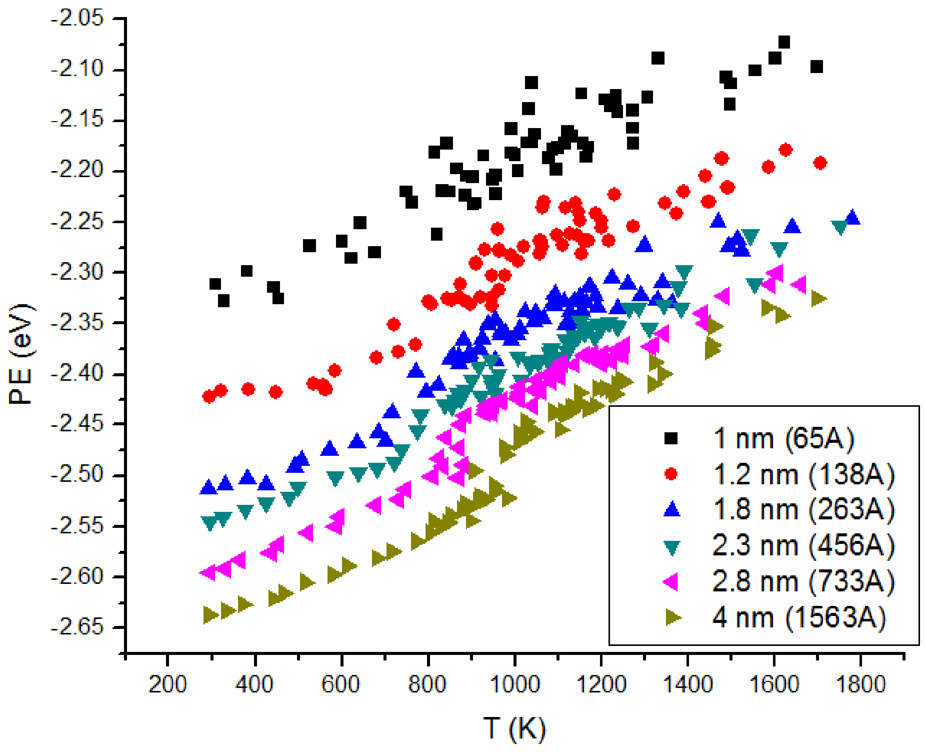

Fig. 6.4 Potential energy (PE) values of different sizes of Ag nanoparticles during the heating process. "A" stands for Atoms

6.5 Summary

FCC truncated octahedral Ag NPs are stable below T_m for 1.8 nm and larger particles but not for 1 and 1.2 nm particles. During heating below T_m, the 1 nm particle fluctuated between a quasi-liquid phase and an icosahedral solid phase as an indication of dynamic coexsistance melting (DCM). The 1.2 nm was stable at RT but transformed into an icosahedral at a temperature much lower than T_m of the particle. Droplets obtained by melting of 1 nm to 2.3 nm truncated octahedral phase froze into an icosahedral phase.

7 MOLECULAR DYNAMICS SIMULATION OF SINTERING AND SURFACE PREMELTING OF Ag NANOPARTICLES

Traditionally, sintering is characterised by three stages. The first is neck formation between two particles followed by a rapid increase in the neck radius. The second is gradual increase in the neck radius and the third is densification of the structure [38]. However, the previously developed sintering theories were based on sintering of microparticles and may not be valid for NPs. Thus, sintering process of Ag NPs in the size range of 4 nm to 20 nm was simulated in this chapter using a previously developed linear scaling parallel MD code [165]. It was possible by this code to use multiple processers simultaneously and hence to simulate sintering of relatively large NPs.

The sintering kinetics of the nanoparticles was measured based on the growth of neck radius to particles radius ratio (x/r) and shrinkage. This chapter reports the sintering kinetics of two particles in size range of 4 nm to 20 nm and sintering of three and four particles of 4 nm diameter. Sintering of three and four NPs was performed to study the effect of pore geometry on the densification process. The effect of the surface premelting on the sintering process is thoroughly discussed. Parts of this chapter was published in *Materials Transactions special issue on Nanojoining and Microjoining* [210]

7.1 Results:

7.1.1 Sintering of Two 4 nm Ag Particles

Fig. 7.1 shows average potential energy (PE) values and atomic plots during heating of two 4 nm particles. It can be clearly seen that the PE curve in Fig. 7.1(a) passed through the same three stages as for other single particles discussed in the previous two chapters. A gradual increase in the average PE values during the first stage was followed a by higher rate of increase during the second stage. During the third stage, the rate of increase in the PE values significantly decreased but was still slightly higher than the first stage. The first, the second, and the third stage are associated with solid phase, melting, and liquid phase, respectively. The atomic arrangements during the sintering process are shown in Fig. 7.1 (b) and are of three (111) atomic planes at the center of the sintered structure. Crystallographic directions of $[\bar{1}01]$ and [110] are represented by blue and red arrows, respectively. Plot A in Fig. 7.1(b) shows the initial configuration at which the two particles were separated by 0.3 nm distance and miss-oriented by 30^o. Once heating was started at point B, particle 2 rotated in anti-clockwise direction and formed a neck with particle 1. The rotation of particle 2 was to minimize the interfacial energy at the grain boundary (G.B.) formed at the neck between the two particles (grains). The neck radius increased as heating continued to point C, which resulted in formation of an edge dislocation (D.L.) inside particle 2 that climbed to the surface at point E. Dislocation climb during sintering has been discussed in previous studies and was attributed to either vacancy annihilation or sintering stress exceeding the yield stress at the sintering temperature [38]. At point E, a new grain was formed at the neck region that has slightly different $[\bar{1}01]$ direction than the $[\bar{1}01]$ directions inside the two particles. It is reasonable to deduce that the shear stress at the neck region has twisted this grain and formed a twin boundary (T.B.). The mirror crystallographic image on both sides of the twin boundary is a special characteristic of twin boundaries [211]. This process relaxed the structure and slightly reduced the slope of the PE curve as shown in Fig. 7.1(a). As the temperature is increased to point G, average PE values increased rapidly as an indication of initiation of surface premelting (S.M.) shown by amorphous regions in the atomic plot. The amorphous regions first appeared at highly curved regions of the surface, which confirms the curvature effect on melting of NPs [101]. Rapid shrinkage only occurred during the melting process at the second stage of the PE curve. The two particles merged into one particle at point I, which is the complete melting point of the sintered structure. The slight change in the shape of the sintered structure between point A and C was due to the rigid rotation of the structure, which was also observed in the simulation domain during sintering of Au NPs [147].

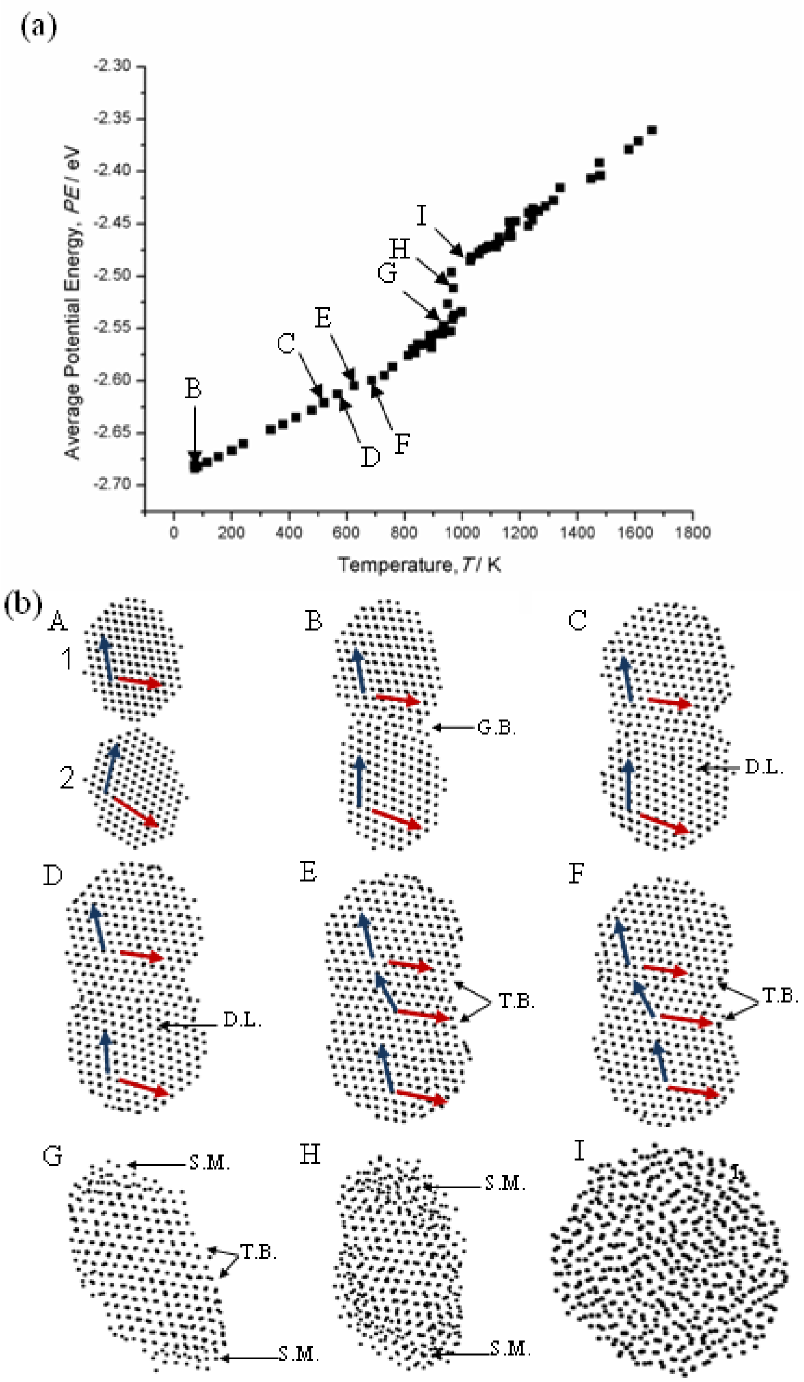

Fig. 7.1 (a) Average PE values of all atoms in the sintered structure during the heating process of two 4 nm particles. (b) Atomic plots of (111) plane at the initial configuration of the two 4 nm Ag NPs at point A and during the heating process for other plots. Each dot in the atomic plots represents an atom. Blue and red arrows follow the crystallographic directions of $[\bar{1}01]$ and [110], respectively. Black arrow heads point toward regions at which grain boundaries (G.B.), twin boundaries (T.W.), dislocations (D.L.), and surface premelting (S.M.) are located.

7.1.2 Sintering Kinetics of Two Ag Nanoparticles

Sintering of two 4 nm and larger particles was divided into three main stages as shown in Fig. 7.2. The first stage is shown in Fig. 7.2 (a) and was formation of a neck between the two NPs followed by a rapid increase in neck radius to particle radius ratio (*x*/*r)* at 50 K for 20 nm particles and at 10 K for smaller particles. According to the author's best knowledge, sintering of NPs has not previously been experimentally examined below RT although it could be performed on TEM stage cooled by liquid Nitrogen. However, sintering of different metallic particles below RT has been observed in other MD simulations shown in Fig. 2.18 and Fig. 2.20 [156-157]. The second stage of sintering showed gradual increase in the neck radius to particle radius ratio (*x*/*r*) as the temperature of the sintered structure reached its own surface premelting point. The increase of this ratio was linearly fitted as shown in Fig. 7.2 (b). Fig. 7.2 (c) shows that sintering rates of two 4 nm particles and two 20 nm particles obtained by the MD simulation were higher than these obtained by theoretical models based on surface diffusion, grain boundary diffusion, and lattice diffusion. This is because the sintering process appeared to be driven by other mechanisms including mechanical rotation and dislocation climbing. Fig. 7.2 (d) shows the shrinkage rate of the sintered structure during the heating process. The shrinkage rate shows a small fixed value during the second stage of sintering and a rapid increase as the temperature reached the surface premelting temperature of the sintered structure. The rapid shrinkage between surface premelting and complete melting points of the sintered structure can be characterized as the third stage of sintering. The temperature regime in which the rapid shrinkage and melting occurred increased as the size of the NPs increased. This agrees with the results in chapter 5 that suggested that the temperature regime at which melting of one single NP occurs increases as the size of the NP increases.

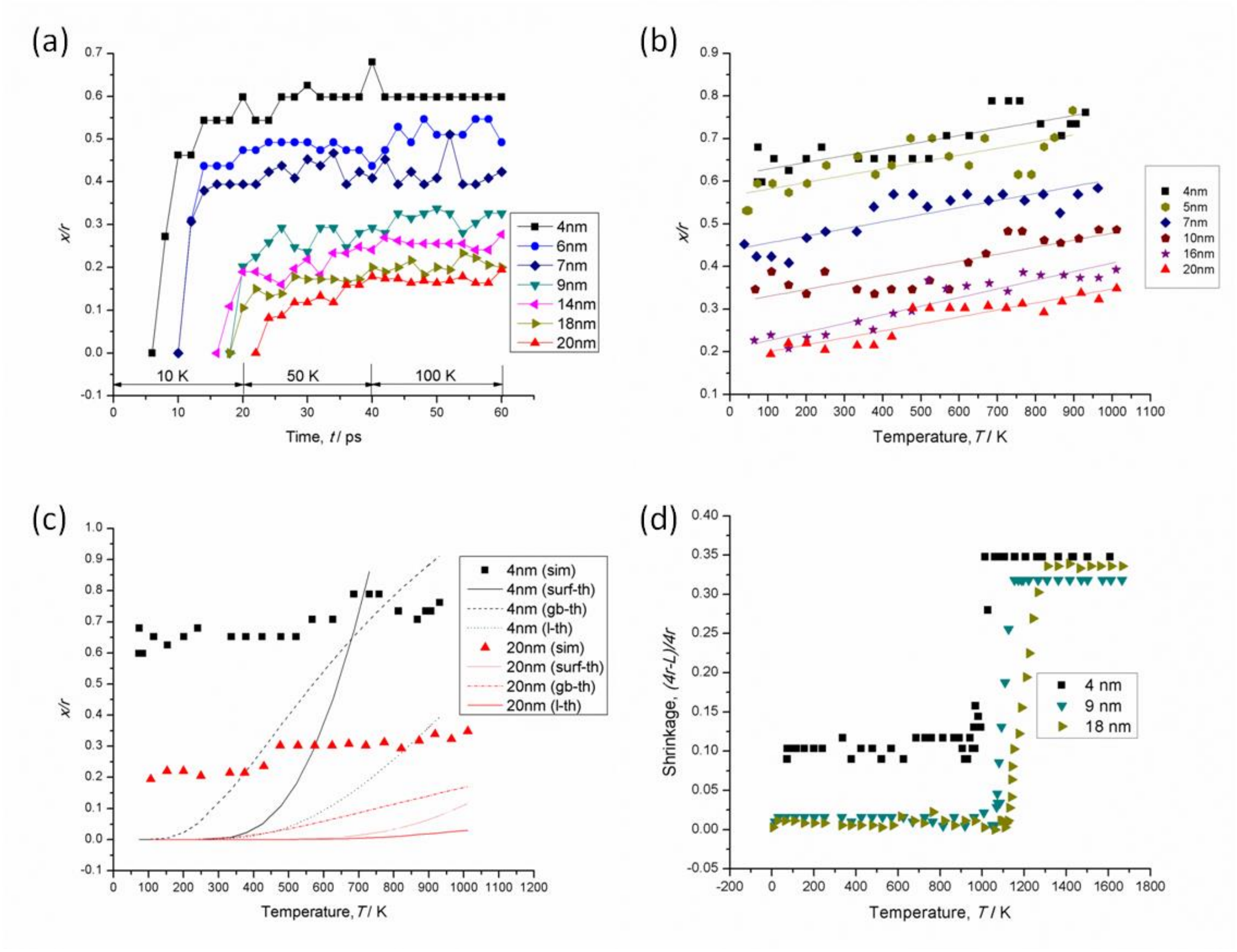

Fig. 7.2 (a) Neck radius to particle radius ratio (*x/r*) during the first stage of sintering of different sizes of Ag NPs. (b) Neck radius to particle radius ratio (*x/r*) during heating below surface premelting temperature (second stage of sintering). The lines show linear fit of the obtained data. (c) Sintering data during the second stage obtained by MD simulation (sim) and by theoretical models based on surface diffusion (surf-th), grain boundary (gb-th) diffusion, and lattice diffusion (l-th). (d) Shrinkage rate during heating of NPs (third stage of sintering).

7.1.3 Sintering of Three 4 nm Ag Particles

Fig. 7.3 shows average PE values and atomic plots of three 4 nm particles during the heating process. The initial configuration of (100) plane at the center of the particles is shown at plot A with blue and red lines following [001] and [010] directions, respectively. The three NPs were separated by about 0.3 nm with particle 1 rotated in anti-clockwise direction by 30^o. As heating of the NPs was started at point B, the three particles joined each other with a slight clockwise rotation of particle 1 to reduce the interfacial energy with the other two particles. Further heating to point C led to further rotation of particle 1, densification, and formation of a grain boundary at the neck region between particle 1 and particle 3 and a twin boundary between these two particles and particle number 2. The reduction of the surface area and the formation of the twin boundary have relaxed the structure and dropped the average PE values. Further increase in temperature to point D led to diffusion between particle 1 and particle 3, which subsequently merged them into one single grain. At point F, amorphous regions started to appear on highly curved regions of the surface as an indication of surface premelting, which led to shrinkage of the structure as heating continued up to the complete melting point of the structure at point I. Plots F, G, and H showed that the twin boundary remained stable during the surface premelting.

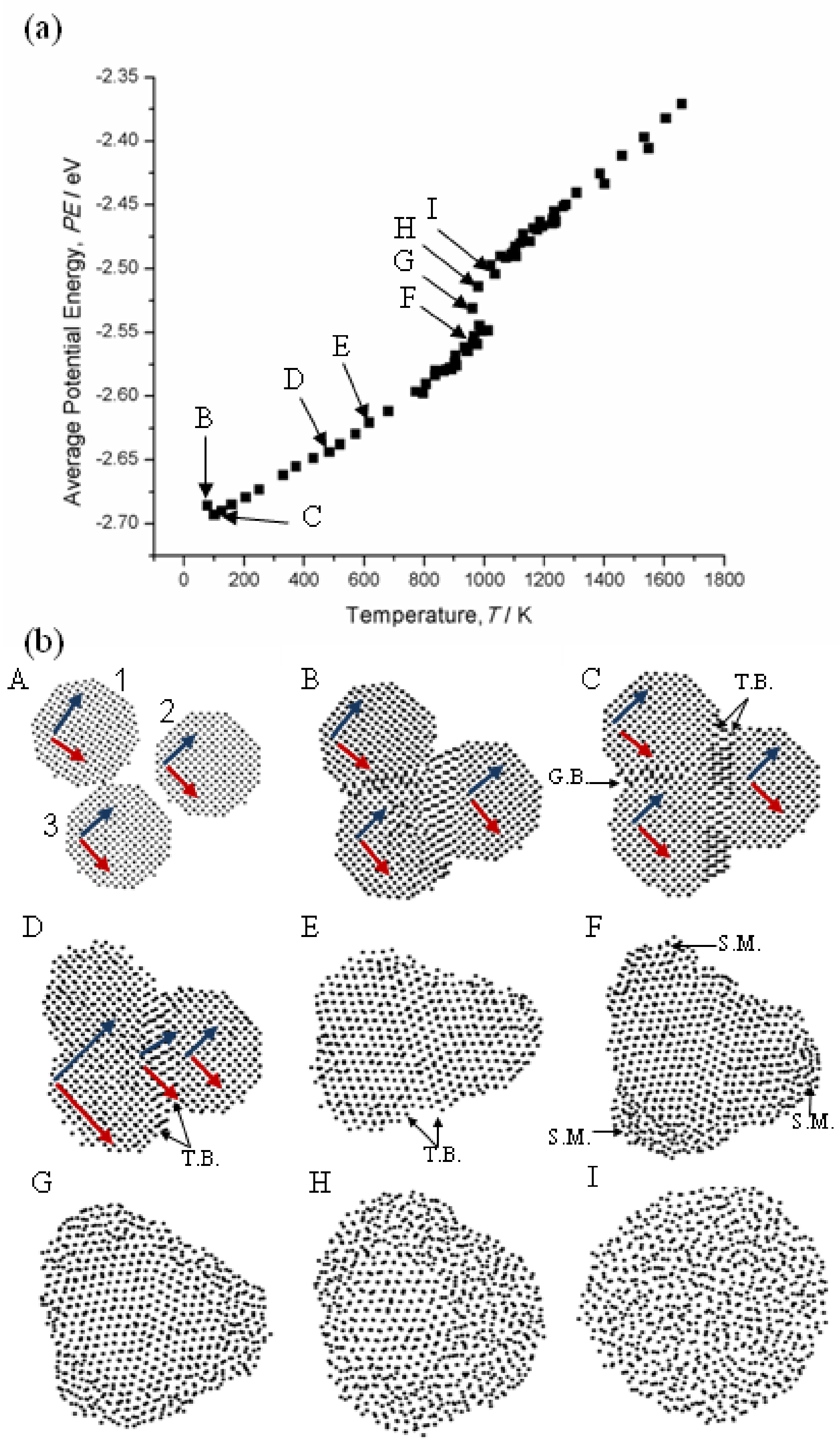

Fig. 7.3 (a) Average PE values of all atoms in the sintered structure of three 4 nm particles during the heating process. (b) Atomic plots of (100) plane at the initial configuration of the three 4 nm Ag NPs at point A and during the heating process for other plots. Each dot in the atomic plots represents an atom. Blue and red arrows follow the crystallographic directions of [001] and [010], respectively. Black arrow heads point toward grain boundaries (G.B.), twin boundaries (T.W.), and surface premelting (S.M.) regions.

7.1.4 Sintering of Four 4 nm Ag Particles

Fig. 7.4 shows average PE values and atomic plots of four 4 nm particles during the heating process. The initial configuration of (100) plane at the center of the particles is shown in plot A with blue and red arrows following [001] and [010] directions, respectively. The separating distance between the particles was about 0.3 nm. The four NPs joined each other and formed necks between them as heating started at point B. Further heating toward point C increased the neck radius, which subsequently caused formation of an edge dislocation (D.L.) at particle 3. Densification occurred at point D, at which the dislocation climbed toward the surface of the particle, possibly driven by either sintering stress or vacancy annihilation. At point E, another dislocation was formed at particle 1 that climbed to the surface of the particle at point F, at which a twin boundary was formed within particle 1 and decreased the slope of the PE curve. The twin boundary extended to particle 3 as the temperature of the structure was increased to point G, which further relaxed the structure and decreased the PE values. Similar to the sintering process of two particles in Fig. 7.1, the twin boundary was also formed and showed the crystallographic mirror on both sides of it. Melting and subsequent shrinkage of the sintered structure started at point H at which amorphous regions started to appear on the highly curved regions of the surface. These amorphous regions extended toward the core of the structure to complete the melting process at point I. Similar to the case of sintering of three particles in Fig. 7.3, the twin boundary remained stable during and prior to the melting process.

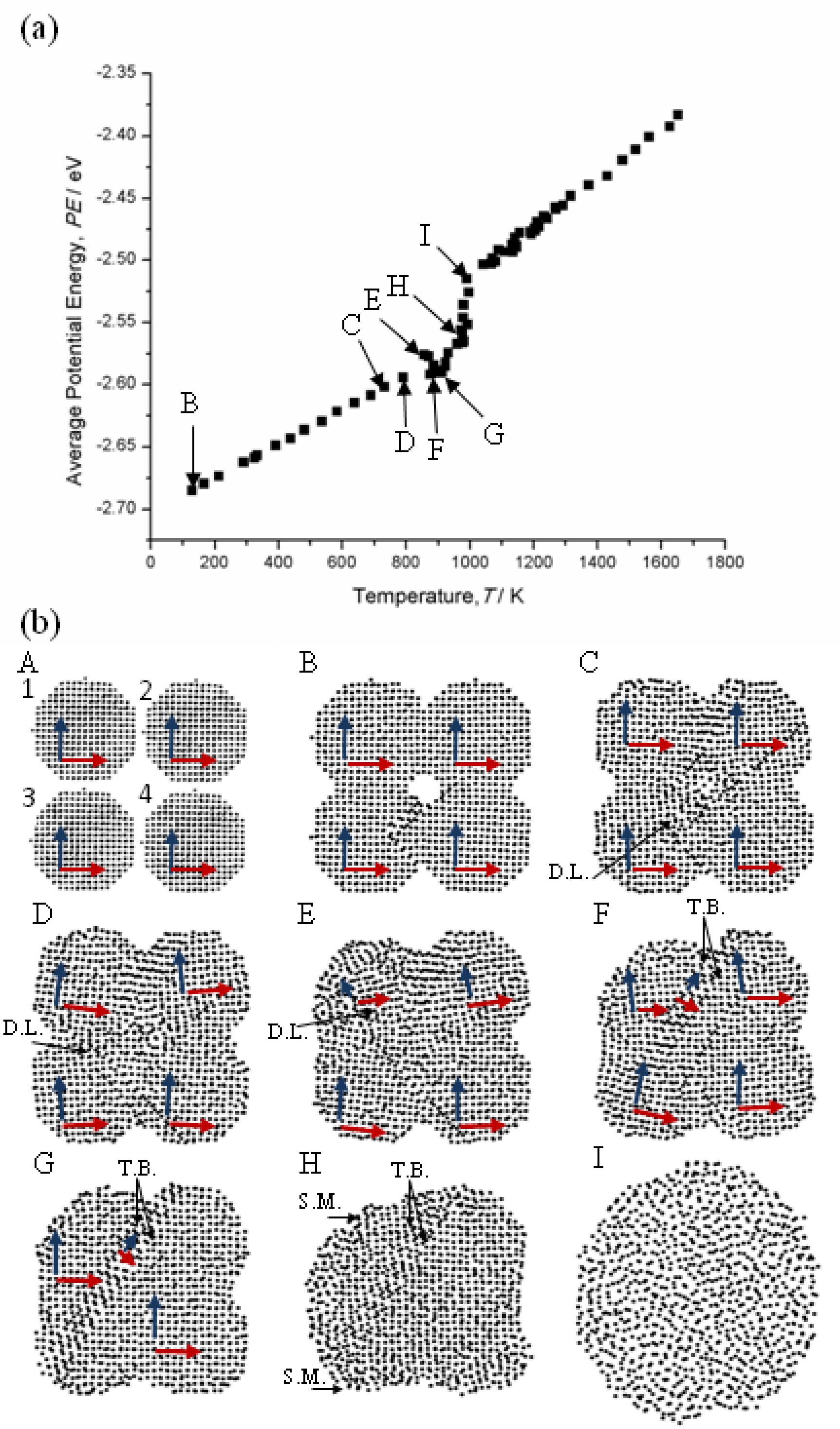

Fig. 7.4 (a) Average PE values of all atoms in the sintered structure during the heating process of four particles of 4 nm diameter. (b) Atomic plots of (100) plane at the initial configuration of the four 4 nm Ag NPs at point A and during the heating process for other plots. Each dot in the atomic plots represents an atom. Blue and red arrows follow the crystallographic directions of [001] and [010], respectively. Arrow heads toward regions at which grain boundaries (G.B.), dislocations (D.L.), twin boundaries (T.W.), and surface premelting (S.M.) are located.

7.2 Discussion

Sintering of three and four NPs showed a similar general trend and stages to sintering of two NPs. They started by forming grain boundaries at the neck region followed by neck growth, which occurred by different mechanisms such as mechanical rotation and dislocations climb. The final stage started at surface premelting temperature and caused the rapid shrinkage of the sintered structure.

Pore geometry was found to have a great effect on the densification process of NPs. The three particles were densified at about 100 K while densification of four particles occurred at about 775 K. Both were driven by mechanical rotation and dislocation climb. As shown in Fig. 2.19, seven 2.4 nm Cu cylinders in closed pack configuration were densified at 300 K [156]. The other studies shown in Fig 2.22 and Fig. 2.23 has confirmed densification of two Ag NPs on a Au substrate at 400 K [159], and at 523 K [47]. These temperatures are within the range of densification temperatures obtained here.

The sintering kinetics obtained here are different than previous sintering theories in two respects [38,212]. First, densification was not characterized as the third and last stage of sintering. Instead, it occurred during the second stage, which was characterized by gradual increase of the neck radius to NP radius ratio. Also, the temperature at which densification occurs was strongly dependent on the pore geometry. Second, the third stage was characterized as liquid state sintering driven by surface premelting of the structure.

7.3 Summary

Sintering of two Ag nanoparticles started at 50 K for the 20 nm particles and at 10 K for the smaller particles and has passed through three stages. The first was rapid increase in the neck radius to NP radius ratio (*x*/*r)*. The second was a gradual linear increase of (*x*/*r)* as the temperature of the sintered structure is increased to T_{sm}. The third stage was rapid shrinkage of the sintered structure driven by surface premelting.

The sintering rates showed higher values than values obtained by sintering models of microparticle. It appears that the sintering process of the simulated NPs was driven by mechanical rotation and dislocations climb in addition to possible diffusion mechanisms. The mechanical rotation occurred at the very beginning of the sintering process and has reduced the interfacial energy between the particles and hence reduces the average PE values of the sintered structure. The formation of the twin boundaries during the sintering process has also reduced the PE values of the sintered structure.

Sintering of three and four 4 nm Ag particles has showed similar sintering mechanisms found in two NPs sintering. Based on the pore geometry, densification of 4 nm particles has occurred during the first stage at 100 K and during the second stage at 775 K for three particles.

8 CONCLUSIONS AND OUTLOOK

This chapter reports the conclusions and outlook for future research that may complement the studies presented here.

8.1 Conclusions

The conclusions are grouped in accordance to the research objectives in section 1.2

8.1.1 Ag Nanoparticle Paste for Cu Bonding

1 Cu wire and Cu foil were successfully bonded together by solid state sintering of Ag NP paste at low temperatures down to 433 K.

2 The Ag NP paste was fabricated by increasing the concentration of 0.001 vol% Ag NP sol to 0.1 vol% through centrifugation. Silver nitrate ($AgNO_3$) was reduced by sodium citrate dihydrate ($Na_3C_6H_5O_7.2H_2O$) to fabricate the 0.001 vol% sol. The Ag NPs are coated with a citrate organic shell that decomposes at 433 K and promotes bonding with the Cu.

3 Under shear tests, the bonds that were formed at 433 K and 523 K had enough strength to cause wire fracture for 50 µm and 250 µm wires, respectively. Shear tests of 500 µm wire showed that the strength of the bond increased as the bonding temperatures increased due to enhanced sinterability of the Ag NPs at higher temperatures. Bonds that are formed by sintering of Ag NPs were proved to withstand higher temperatures than the bonding temperatures.

4 The microstructure analysis of the cross sectional area of the joint confirmed the metallic bond between the Ag NPs and the Cu.

8.1.2 Melting of Ag Nanoparticles

1 Complete melting and surface premelting temperatures of 4 nm to 20 nm FCC truncated octahedral Ag NPs were determined by MD simulation based on EAM. The applied simulation could predict T_{m} and T_{sm} for a larger size range of NPs than the previous theoretical models. Hanszen's model was found to be valid for 8 nm to 10 nm particles, while Shi's model and liquid drop model were found to be able to predict the complete melting point of smaller NPs.

2 Unlike previous surface premelting studies that suggested that surface premelting and complete melting occur at one single temperature, melting of NPs in the size range of 8 nm to 20 nm occurred at a temperature range and started by forming quasi-liquid ponds on the surface of the NP at a surface premelting temperature (T_{sm}). As temperature increased, those quasi-liquid ponds grew and formed a contiguous quasi-liquid layer.

3 As a general rule, the ratio of the quasi-liquid layer thickness to the NP radius showed a linear relationship with temperature. A liquid layer of a critical thickness (t_{o}=1.8 nm) was formed once the whole particle had transitioned to the quasi-liquid phase for NPs in size range of 8 nm to 10 nm and once the quasi-liquid layer reached a thickness of 5 nm for larger particles. The liquid layer expanded to complete the melting of the NP at its complete melting temperature (T_{m}).

4 Ag NPs smaller than 8 nm melted at a single temperature (T_{m}) without passing through the surface premelting stage.

5 Complete melting points (T_{m}) of Ag NPs in size range of 12 nm to 20 nm deviated from Hanszen's model and approached T_{m} of the bulk.

8.1.3 Stability of Truncated Octahedral Ag Nanoparticles

1 The 1 nm Ag particle fluctuated between icosahedral and quasi-liquid phases below T_{m} as an indication of DCM.

2 Heating of 1.2 nm showed solid to solid phase transition from the initial truncated octahedral to icosahedral configuration far below T_{m}.

3 The smallest Ag NP at which the truncated octahedral is stable below T_{m} is 1.8 nm.

4 Ag NPs in size range of 1 nm to 2.3 nm froze into an icosahedral configuration, which is the energetically favorable structure based on PE values.

5 Thermal hysteresis between melting and freezing was observed during heating and cooling cycles of all sizes of NPs.

8.1.4 Sintering of Ag Nanoparticles

1 The results of MD simulation of sintering behavior of Ag NPs in size range of 4 nm to 20 nm showed that sintering occurred in three main stages and showed higher sintering rates than those predicted by theoretical models of sintering of microparticles. The first stage was neck formation and rapid growth of the neck radius to particle radius ratio (x/r) in temperature regime of 10 K to 50 K for all sizes of NPs. Second stage was characterized by gradual linear increase of the neck radius to particle radius ratio (x/r) as the temperature is increased to the surface premelting temperature of the sintered structure. Rapid shrinkage of the sintered structure occurred during the third stage and was initiated at the surface premelting temperature and was driven by further melting of the surface layer toward the core of the sintered structure.

2 Edge dislocations and a twin boundary were formed within the sintered structure during the second stage of sintering. The formation of a twin boundary relaxed the structure and decreased the slope of the PE curve during the heating process.

3 Initial packing configuration of the NPs has a significant effect on the densification rate of the sintered NPs.

8.2 Outlook

Research completed in this thesis has opened new areas worth considering in future studies on different metallic NPs (ex: Ag, Au, Cu, Pd, etc…). The following are research ideas for those who would like to further investigate the work that I started in this thesis.

1 Chapter 6 reported the initial step towards drawing a phase map of Ag NPs at different sizes and temperatures. This study has only initiated the heating process on FCC truncated octahedral configuration. To complete this work, heating should be applied other structures such as icosahedra and decahedra. The transitions between different solid phases could be monitored to further understand why and how they occur.

2 Fig. 5.11 has showed that T_m of a polycrystalline 4 nm Ag particle is slightly less than T_m of the 4 nm FCC truncated octahedral particle. It is worth studying melting of different solid structures of NPs such as the icosahedral and decahedral structures, and NPs with defects. These studies may benefit the ongoing research on melting of metallic NPs

3 Sintering studies performed here has not studied the effect of the initial miss-orientation angle between the NPs on the sintering process. There might be a maximum angle for each size of NPs at which mechanical rotation will not occur. The effect of the initial miss-orientation

angle on the formation of twin boundaries is also worth looking at for further understanding of the fundamentals of NPs sintering.

4 Based on the author best knowledge, the mechanism of sintering of Ag NPs on Cu substrates has not been previously studied. This work is worth considering for further investigation of how Ag NP paste sinter on Cu substrates during the bonding process discussed in Chapter 4.

Bibliography

1. Y. Zhou (Editor), Microjoining and Nanojoining, Cambridge, UK, CRC Press/Woodhead Publishing, 2008.

2. K. Suganuma, S.J. Kim, K.S. Kim, "High-temperature lead-free solders: properties and possibilities", *JOM*, Vol. 61, No. 1, 2009, pp. 64–71.

3. Y. Takaku, I. Ohnuma, Y. Yantada, Y. Yagi, I. Nakagawa, T. Atsumi, M. Shirai, K. Ishida, "A Review of Pb-Free High-Temperature Solders for Power-Semiconductor Devices: Bi-Base Composite Solder and Zn-Al Base Solder", *ASTM Spec. Tech. Publ.*, Vol. 1530, 2009, pp. 27–49.

4. V. Chidambaram, J. Hattel, J. Hald, "High-temperature lead-free solder alternatives", *Microelectron. Eng.*, Vol. 88, No. 6, 2011, pp. 981–989.

5. Y. Zhou, A. Hu, M. I. Khan, W. Wu, B. Tam, M. Yavuz., "Recent progress in micro and nano-joining", *J. Phys. Conf. Ser.*, Vol. 165, NO. 1. 2009, pp. 012021-1-6.

6. R. Sharp, "The current status of high temperature electronics for automotive use", *IEEE Colloq. (Dig.),* 1999, pp. 1–4.

7. Y. Akeda, H. Tatsumi, T. Yamaguchi, A. Hirose, T. Morita, and E. Ide, **"**Interfacial Bonding Mechanism Using Silver Metallo-Organic Nanoparticles to Bulk Metals and Observation of Sintering Behavior", *Mater. Trans.*, Vol. 49, No. 7, 2008, pp. 1537-1545.

8. T. Morita, E. Ide, Y. Yasuda, A. Hirose, K. Kobayashi, "Study of Bonding Technology Using Silver Nanoparticles", *Jpn. J. Appl. Phys.*, Vol. 47, 2008, pp. 6615-6622.

9. E. Ide, S. Angata, A. Hirose, K.F. Kobayashi, "Bonding of Various Metals Using Ag Metallo-Organic Nanoparticles-A Novel Bonding Process Using Ag Metallo-Organic Nonoparticles', *Mater. Sci. Forum.*, Vol. 512, 2006, pp. 383-388.

10. A. Hu, P. Peng, H. Alarifi, X. Y. Zhang, J. Y. Guo, Y. Zhou, W. W. Duley "Femtosecond laser welded nanostructures and plasmonic devicess", *J. Laser, Appl.*, Vol. 24, No. 4, 2012, pp. 042001-1-7.

11. J. Yan, G. Zou, A. Wu, J. Ren, A. Hu, Y. N. ZHOU "Improvement of Bondability by Depressing the Inhomogeneous Distribution of Nanoparticles in a Sintering Bonding Process with Silver Nanoparticles", *J. Electron. Mater.,*Vol. 41, No. 7, 2012, pp. 1924-1930.

12. Y. Zhou, A. Hu "From Microjoining to Nanojoining" *Open Surf. Sci. J.*, Vol. 3, 2011 pp. 32-41.

13. E. Ide, A. Angata, A. Hirose, K.F.Kobayashi, “Metal–metal bonding process using Ag metallo-organic nanoparticles“, *Acta Mater.*, Vol. 53, No. 8, 2005, pp. 2385-93.

14. G. L. Allen, R. A. Bayles, W. W. Gile, W. A. Jesser, “Small particle melting of pure metals“ *Thin Solid Films*, Vol. 144, No. 2, 1986, pp. 297-308

15. K. Dick, T. Dhanasekaran, Z. Zhang, D. Meisel, “Size-dependent melting of silica-encapsulated gold nanoparticles”, *J. Am. Chem. Soc.*, Vol. 124, No. 10, 2002, pp. 2312-17.

16. Z. B. Güvenc, J. Jellinek, A. F. Voter, in Physics and Chemistry of Finite Systems: From Clusters to Crystals, edited by P. Jena, S. N. Khanna, B. K. Rao (Kluwer, Dordrecht, 1992), Vol. 1, p. 411.

17. E. K. Yildirim, M. Atis, Z. B. Güvenç, “Structure and Dynamical Properties of Au_N, N = 12–14 Clusters: Molecular Dynamics Simulation”, *Int. J. Mod. Phys. C*, Vol. 16, No. 6, 2005, pp. 99-116.

18. M. Boyukata Z. B. Güvenç, “MD Study of Energetics, Melting and Isomerization of Aluminum Microclusters”, *Braz. J. of Phys.*,Vol. 36, No. 3A, 2006, pp. 720-724.

19. K. Kang, S. Qin, C. Wang, “Size-dependent melting: Numerical calculations of the phonon spectrum”, *Physica E*, Vol. 41, No. 5, 2009, pp. 817-821.

20. Q.S. Mei, K. Lu, “Melting and superheating of crystalline solids: From bulk to nanocrystals”, *Prog. Mater. Sci.*, Vol. 52, No. 8, 2007, pp. 1175-1262.

21. K. K. Nanda, S. N. Sahu, S. N. Behera, “Liquid-drop model for the size-dependent melting of low-dimensional systems”, *Phys. Rev. A*, Vol. 66, No. 1, 2002, pp. 013208-1-8.

22. F. G. Shi, “Size-Dependent Thermal Vibrations and Melting in Nanocrystals”, *J. Mater. Res.*, Vol. 9, No. 5, 1994, pp. 1307-1313.

23. K-J. Hanszen, “Theoretische Untersuchungen über den Schmelzpunkt kleiner Kügelchen Ein Beitrag zur Thermodynamik der Grenzflächen”, *Z. Phys.*, Vol. 157, No. 5, 1960, pp. 523-553.

24. F. A. Lindemann, “The calculation of molecular vibration frequencies”, *Phys. Z.*, Vol. 11, 1910, pp. 609-612.

25. H. Schwarzbauer, R. Kuhnert, “Novel Large Area Joining Technique for Improved Power Device Performance”, *IEEE Trans. Ind. Appl.*, Vol. 27, 1991, pp. 93–95.

26. H. Schwarzbauer, "Method of Securing Electronic Components to a Substrate", *US Patent*, No. US4810672, Siemens AG, 1989.

27. W. Baumgartner, J. Fellinger, "Method for fastening electronic components to a substrate using a film", *US Patent,* No. US4856185, Siemens AG, 1989.

28. H. Schwarzbauer, "Heat-conducting adhesive joint with an adhesive-filled, porous heat conductor", *US Patent,* No. US6823915B2, Siemens AG, 2004.

29. G. Palm, "Method for securing electronic components to a substrate", *US Patent*, US2005/0247760A1, Semikron Elektronik GmbH, 2005.

30. I. J. Rasiah, "Electrically conductive thermal interface", *US Patent*, US7083850B2, Honeywell International Inc., 2006.

31. H. Tatsumi, Y. Akada, T. Yamaguchi, A. Hirose, "Sintering Mechanism of Composite Ag Nanoparticles and its Application to Bonding Process-Effects of Ag_2CO_3 Contents on Bondability to Cu", *Adv. Mater. Res.*, Vol. 26-28, 2007, pp. 499-502.

32. T. Morita, Y. Yasuda, E. Ide, Y. Akada, A. Hirose, "Bonding Technique Using Micro-Scaled Silver-Oxide Particles for In-Situ Formation of Silver Nanoparticles", *Mater. Trans.*, Vol. 49, No. 12, 2008, pp. 2875-2880.

33. H. Alarifi, A. Hu, M. Yavuz, Y. Zhou, "Bonding of Cu Wires by Solid State Sintering of Ag Nanoparticles at Low Temperatures", *Materials Research Society Symposium Proceedings*, Vol. 1207, 2010, pp. 7-12.

34. G. Zou, J. Yan, A. Hu, H. Alarifi, Y.N. Zhou, "Bonding of Cu to Cu Bulks through the Low Temperature Sintering of Ag Nanoparticle Paste", *Materials Science & Technology Conference and Exhibition*, Vol. 4, 2010, pp. 2642-2650.

35. Y. Morisada, T. Nagaoka, M. Fukusumi, Y. Kashiwagi, M. Yamamoto, M. Nakamoto, "A Low-Temperature Bonding Process Using Mixed Cu-Ag Nanoparticles", *J. Electron. Mater.*, 2010, Vol. 39, No. 8, 2010, pp. 1283–1288.

36. M. Tobita, Y. Yasuda, "Interconnect Material and Interconnect Formation Method", *US Patent*, No. US20090180914, Hitachi Ltd. 2009.

37. K.S. Siow, "Mechanical properties of nano-silver joints as die attach materials", *J. Alloys Compd.*, Vol. 514, 2012, pp. 6-19.

38. R. German, Sintering Theory and Practice, New York, John Wiley & Sons, Inc, 1996.

39. M. Knoerr, A. Schletz, "Power semiconductor joining through sintering of silver nanoparticles: Evaluation of influence of parameters time, temperature and pressure on

density, strength and reliability”, *Proc. 6th Int. Conf. Integr. Power Electron. Syst.*, 2010, pp. 1–6.

40. T.G. Lei, J.N. Calata, G.Q. Lu, X. Chen, S. Luo, “Low-Temperature Sintering of Nanoscale Silver Paste for Attaching Large-Area (> 100 mm^2) Chips”, *IEEE Trans. Compon. Package Tech.*,Vol. 33, No. 1, 2010, pp. 98–104.

41. S. Joo, D.F. Baldwin, “Adhesion mechanisms of nanoparticle silver to substrate materials: identification”, *Nanotech.*, Vol. 21, No.5, 2010, pp. 055204-1-12.

42. E.A. Holm, J.D. Puskar, M. Reece, V. Tikare, G.C. Cardona, L.N. Brewer, “Nanocrystal Enabled Solid State Bonding”, *Sandia National Laboratories*, SAND2010-7013, 2010, pp. 1-31.

43. T. Wang, X. Chen, G.Q. Lu, G. Lei, “Low-temperature sintering with nano-silver paste in die-attached interconnection”, *J. Electron. Mater.* Vol. 36, No. 10, 2007, pp. 1333–1340.

44. C. Fruh, M. Gunther, M. Rittner, A. Fix, M. Nowottnick, “Characterisation of silver particles used for the Low Temperature Joining Technology”, *Proc. 3rd Electron. Syst. Integr. Tech. Conf.,* 2010, pp. 1–5.

45. J. Jiu, K. Murai, K. Kim, K. Suganuma, “Synthesis of Ag nanorods and application to soft die attaching”, *Proc. 7th IEEE Conf. Polym. Adhes. Microelectron. Photonics*, 2008, pp. 1–5.

46. H. Zheng, L. Xu, J. Calata, K. Ngo, S. Luo, G.Q. Lu, “Effect Of Oxygen Partial Pressure On Sintering Nanoscale Silver Die-attachment On Copper Substrate”, *Center for Power Electronics Systems conference*, 2011.

47. T. Ogura, M. Nishimura, H. Tatsumi, N. Takeda, W. Takahara, A. Hirose, “Evaluation of Interfacial Bonding Utilizing Ag2O-Derived Silver Nanoparticles Using TEM Observation and Molecular Dynamics Simulation”, *Open Surf. Sci. J.*, Vol. 3, 2011, pp. 55–59.

48. W. Sutherland, “A kinetic theory of solids, with an Experimental Introduction“, *Philos. Mag.*, Vol. 32, No.194, 1891, pp. 31-43.

49. J. J. Gilvarry, ”The Lindemann and Gruneisen Laws”, *Phys. Rev.*, Vol. 102, No.2, 1956, pp. 308-316.

50. L. Brillouin, “On thermal dependence of elasticity in solids” *Phys Rev.*, Vol. 54, No.11, 1938, pp. 916-917.

51. M. Born, “Thermodynamics of crystals and melting”, *J. Chem. Phys.*, Vol. 7, No. 8, 1939, pp. 591-603.

52. K. F. Herzfeld, M. Goeppert-Mayer, "On the theory of fusion", *Phys. Rev.*, Vol. 46, No. 11, 1934, pp. 995-1001.

53. J. Frenkel, Introduction to the theory of metals. Warsaw: PWN, 1955.

54. H. Eyring, MS. John, Significant liquid structures. New York, Wiley, 1969.

55. T. Gorecki, "Vacancies and changes of physical-properties of metals at melting-point", *Z. Metall.*, Vol. 65, No.6, 1974, pp. 426-431.

56. T. Gorecki, "Vacancies of changes of 1st coordination sphere radius of metals at melting-point", *Z. Metall.*, Vol. 67, No.4, 1976, pp. 269-273.

57. F. Delogu, "Molecular dynamics simulations of homogeneous and heterogeneous melting scenarios in metals: Volume scaling and concentration of defects" *Phys. Rev. B*, Vol. 73, No. 18, 2006, pp. 184108-1-10.

58. F. Delogu, "Mechanistic aspects of homogeneous and heterogeneous melting processes", *J. Phys. Chem. B*, Vol. 110 No. 25, 2006, pp. 12645-52.

59. JF. Lutsko, D. Wolf, SR. Phillpot, S. Yip, "Molecuar-Dynamics Study of Lattice-Deffect-Nucleated Melting in Metals using an Embedded-Atom-Method Potential", *Phys. Rev. B*, ,Vol. 40, No.5, 1989, pp. 2841-55.

60. A. M. Alsayed, M. F. Islam, J. Zhang, P. J. Collings, A. G. Yodh, "Premelting at Defects within Bulk Colloidal Crystals", *Science*, Vol. 309, No. 5738, 2005, pp. 1207-10.

61. M. Faraday, "Note on Regelation", *Proc. R. Soc. Lond.*, Vol. 10, 1859, pp. 440-450.

62. K. C. Prince, U. Breuer, H. P. Bonzel, "Anisotropy Of The Order-Disorder Phase Transition On The PB(110) Surface ", *Phys. Rev. Lett.*, Vol. 60, No. 12, 1988, pp. 1146-1149.

63. A. Pavlovska, M. Tikhov, Yingjun Gu, E. Bauer, "Thermal Disordering of the Al(110) Surface", *Surf. Sci.*, Vol. 278, No. 3, 1992, pp. 303-316.

64. B. Pluis, J.M. Gay, J.W.M. Frenken, S. Gierlotka, J.F. Van Der Veen**,** J.E. Macdonald, A.A. Williams**,** N. Piggins**,** J. Als-Nielsen**,** "X-ray Reflectivity Study of Surface-Initiated Melting: Density Profile at the Pb(110) surface", *Surf. Sci.*, Vol. 222, No. 2-3, 1989, pp. L845-L852.

65. J. W. M. Frenken, P. M. J. Maree, J. F. Vanderveen, "Observation of Surface-Initiated Melting", *Phys. Rev. B*, Vol. 34. No. 11, 1986, pp. 7506-16.

66. A. W. D. Vandergon, R. J. Smith, J. M. Gay, D. J. O'connor, J. F. Vanderveen, "Melting of Al surfaces", *Surf. Sci.*, Vol. 227, No. 1-2, 1990, pp. 143-149.

67. Y. Lereah, R. Kofman, J. M. Pénisson, G. Deutscher, P. Cheyssac, T. Ben David, A. Bourret, "Time-Resolved Electron Microscopy Studies of the Structure of Nanoparticles and their Melting", *Philos. Mag. B,* Vol. 81, No. 11, 2011, pp. 1801-19.

68. C. R. M. Wronski, "The Size Dependence of Melting Point of Small Particles of Tin", *Brit. J. Appl. Phys.,* Vol. 18, No. 12, 1967, pp. 1731-37.

69. M. Polcik, L. Wilde, J. Haase, "Partial Order of the Quasiliquid during Surface Melting of Al(110)", *Phys. Rev. Lett.,* Vol. 78, No.3, 1997, pp. 491-494.

70. E. T. Chen, R. N. Barnett, U. Landman, "Surface Melting of Ni(110)", *Phys. Rev. B,* Vol. 41, No. 1, 1990, pp. 439-450.

71. H. Häkkinen, M. Manninen, "Computer Simulation of Disordering and Premelting of Low-Index Faces of Copper", *Phys. Rev. B,* Vol. 46, No. 3, 1992, pp. 1725-42.

72. L. Pedemonte, G. Bracco, R. Beikler, E. Taglauer, A. Robin, W. Heiland, "A Low-Energy Ion Scattering Study of Al(110) Surface Melting", *Surf. Sci.*, Vol. 532-535, 2003, pp. 13-18.

73. N. Georgiev, A. Pavlovska, E. Bauer, "Surface Disordering without Surface Roughening", *Phys. Rev. B,* Vol. 52, No.4, 1995, pp. 2878-2888.

74. A. Hoss, M. Nold, P. von Blanckenhagen, O. Meyer, "Roughening and Melting of Au(110) Surfaces", *Phys. Rev. B*, Vol. 45, No. 15, 1992, pp. 8714-20.

75. G. Bilalbegović, E. Tosatti, "Incomplete Melting of the Au(100) Surface", *Phys. Rev. B*, Vol. 48, No.15, 1993, pp. 11240-48.

76. Y. Cao, E. Conrad, "Anomalous Thermal Expansion of Ni (001)", *Phys. Rev. Lett.*, 1990, Vol. 65, No. 22, 1990, pp. 2808-11.

77. H. M. van Pinxteren, J. W. M. Frenken, "Incomplete Melting of Pb(001) and Vicinal Surfaces", *Surf. Sci.*, Vol. 275, No.3, 1992, pp. 383-394.

78. B. Pluis, A. W. Denier van der Gon, J. W. M Frenken, J. F. van der Veen, "Crystal-Face Dependence of Surface Melting", *Phys. Rev. Lett.,* Vol. 59, No.23, 1987, pp. 2678-81.

79. B. Pluis, D. Frenkel, JF. Vanderveen, "Surface-Induced Melting and Freezing II. a Semiempirical Landau-Type Model", *Surf. Sci.*, 1990, 239(3), pp. 282-300.

80. P. Carnevali, F. Ercolessi, E. Tosatti, “Melting and Nonmelting Behavior of the Au(111) Surface”, *Phys. Rev. B*, 1987, 36(12), pp. 6701-4.

81. G. Bilalbegovic, F. Ercolessi, E. Tosatti, “Orientational Phase-Separation for Vicinal Surfaces close to the Nonmelting Pb(111) Face”, *Europhys. Lett.*, Vol. 17, No. 4, 1992, pp. 333-337.

82. Z. H. Jin, K. Lu, in: Encyclopedia of materials: Science and technology. Amsterdam, Elsevier, 2002.

83. L. Pedemonte, G. Bracco, A. Robin, W. Heiland, “Residual Order within the Molten Al(110) Surface Layer”, *Phys. Rev. B*, Vol. 65, No. 24 , 2002, pp. 245406-1-5.

84. M. Takagi, “Electron-Diffraction Study of Liquid-Solid Transition of Thin Metal Films”, *J. Phys, Soc. Jpn.* Vol. 9, No. 3, 1954, pp. 359-363.

85. B. T. Boiko, A. T. Pugachev, V. M.. Bratsykh, “Melting of Subcritically Thin Condensed Films of Indium”, *Sov. Phys.-Solid State,* Vol. 10, No.12, 1969, pp. 2382-84

86. M. Blackman, AE. Curson, Structure and properties of thin films. New York: Wiley, 1959. p. 217.

87. C. J. Coombes, “The Melting of Small Particles of Lead and Indium”, *J. Phys. F*, Vol. 2, No. 3, 1972, pp. 441-449.

88. Ph. Buffat, J-P Borel, “Size Effect on the Melting Temperature of Gold Particles”, *Phys. Rev. A*, Vol. 13, No. 6, 1976, pp. 2287-98.

89. R. Berman, Z. Curzon, “Size Dependence of Melting-Point of Small Particles of Indium”, *Can. J. Phys.*, Vol. 52, No. 11, 1974, pp. 923-929.

90. R. A. Bayles, “Melting Behavior of Small Tin Crystallites”, *University of Virginia*, Ph.D Dissertation, 1979.

91. M. Blackman, S. J. Peppiatt, J. R. Sambles,,“Superheating of Bismuth”, *Nat. Phys. Sci.* Vol. 239, No. 91, 1972, pp. 61-62.

92. S. L. Lai, J. Y. Guo, V. Petrova, G. Ramanath,L. H. Allen, “Size-Dependent Melting Properties of Small Tin Particles: Nanocalorimetric Measurements”, *Phys. Rev. Lett.*, Vol. 77, No. 1, 1996, pp. 99-102.

93. K. F. Peters, Y. Chung, J. B. Cohen, “Surface Melting on Small Particles”, *Appl. Phys. Lett.*, Vol. 71, No. 16, 1997, pp, 2391-1-3.

94. K. F. Peters, J. B. Cohen, Y. Chung, “Melting of Pb Nanocrystals”, *Phys Rev. B*, 1998, Vol. 57, No. 21, pp. 13430-38.

95. X. Y. Qin, X. J. Wu, L. F. Cheng, “Exothermal and Endothermal Phenomena in Nanocrystalline Aluminum”, *Nanostruct. Mater.*, Vol. 2, No.1, 1993, pp. 99-108.

96. J. Eckert, J. C. Holzer, C. C. Ahn, Z. Fu, W. L, Johnson, “Melting Behavior of Nanocrystalline Aluminum Powers”, *Nanostruct. Mater.*, Vol.2, No.4, 1993, pp. 407-413.

97. T. Bachels, H-J. Güntherodt, and R. Schäfer, “Melting of Isolated Tin Nanoparticles”, *Phys. Rev. Lett.*, Vol. 85, No. 6, 2000, pp. 1250-53.

98. Z. L. Wang, J. M. Petroski, T. C. Green, and M. A. El-Sayed, “Shape Transformation and Surface Melting of Cubic and Tetrahedral Platinum Nanocrystals”, *J. Phys. Chem. B*, Vol. 102, No. 32, 1998, pp. 6145-6151.

99. N. Wang, S. I. Rokhlin, D. F. Farson, “Nonhomogeneous Surafce Premelting of Au Nanoparticles”, *Nanotechnology*, Vol. 19, No. 41, 2008, pp. 415701-1-7.

100. E. C. Neyts, A. Bogaerts, “Numerical Study of the Size-Dependent Melting Mechanisms of Nickel Nanoclusters”, *J. Phys. Chem. C*, Vol. 113, No. 7, 2009, pp. 2771-76.

101. R. Kofman, P. Cheyssac, Y. Lereah, A.Stella “Melting of Clusters Approaching 0D”, *Eur. Phys. J. D*, Vol. 9, No. 1-4, 1999, pp. 441-444.

102. A. P. Chernyshev, “Effect of Nanoparticle Size on the Onset Temperature of Surface Premelting”, *Mater. Lett.* Vol. 63, No. 17, 2009, pp. 1525-1527.

103. A. P. Chernyshev, “Melting of Surface Layers of Nanoparticles: Landau Model”, *Mater. Chem. Phys.*, Vol. 112, No. 1, 2008, pp. 226-229.

104. Z. L. Wang, “Transmission Electron Microscopy of Shape-Controlled Nanocrystals and Their Assemblies”, *J. Phys. Chem. B*, Vol. 104, No. 6, 2000, pp. 1153-1175.

105. M. José-Yacamán, M. Marin-Almazo, J. A. Ascencio ,“High Resolution TEM Studies on Palladium Nanoparticles” *J Mol. Catal. A-Chem.* ,Vol.173, No. 1-2, 2001, pp. 61–74.

106. F. Baletto, C. Mottet, R. Ferrando, “Microscopic Mechanisms of the Growth of Metastable Silver Icosahedra”, *Phys. Rev. B*, Vol. 63, No. 15, 2001, pp. 155408-1-10.

107. F. Baletto, C. Mottet, and R. Ferrando, “Reentrant Morphology Transition in the Growth of Free Silver Nanoclusters”, *Phys. Rev. Lett.*, Vol. 84, No. 24 2000, pp. 5544-5547.

108. Y. G. Chushak, L. S. Bartell, "Melting and Freezing of Gold Nanoclusters", *J. Phys. Chem. B,* Vol. 105, No. 47, 2001, pp. 11605-11614.

109. H. S. Nam, N. M. Hwang, B. D. Yu, J. K. Yoon, "Formation of an Icosahedral Structure during the Freezing of Gold Nanoclusters: Surface-Induced Mechanism", *Phys. Rev. Lett.*, Vol. 89, No. 27, 2002, pp. 275502-1-4.

110. S. C. Hendy, B. D. Hall, "Molecular-Dynamics Simulations of Lead Clusters", *Phys. Rev. B*, Vol. 64, No. 8, 2001, pp. 085425-1-11.

111. C. L. Kuo and P. Clancy, "Melting and Freezing Characteristics and Structural Properties of Supported and Unsupported Gold Nanoclusters" *J. Phys. Chem. B,* Vol. 109, No. 28, 2005, pp. 13743-13754.

112. F. Baletto, C. Mottet , R. Ferrando "Freezing of Silver Nanodroplets", *Chem. Phys. Lett*., Vol. 354, No. 1-2, 2002, pp. 82–87.

113. J. Uppenbrink. D. J. Wales "Packing Schemes for Lennard-Jones Clusters of 13 to 150 Atoms : Minima, Transition States and Rearrangement Mechanisms", *J. Chem. Soc. Farady, Trans.*, Vol. 87, No.2, 1991, pp. 215-222.

114. F. Baletto , R. Ferrando , A. Fortunelli , F. Montalenti , C. Mottet, "Crossover among structural motifs in transition and noble-metal clusters", Vol. 116, No.9, 2002, pp. 3856-3863.

115. P. M. Ajayan and L. D. Marks "Phase Instabilities in Small Particles", *Phase Transit*., Vol. 24-26, No. 1, 1990, pp. 229-258.

116. C. L. Cleveland and U. Landman, "The energetics and structure of nickel clusters: Size dependence", *J. Chem. Phys*., Vol. 94, No. 11, 1991, pp. 7376-7396.

117. F. Baletto, A. Rapallo,3 G. Rossi,1 and R. Ferrando, "Dynamical Effects in the Formation of Magic Cluster Structures", *Phys. Rev. B,* Vol. 69, No. 23, 2004, pp. 235421-1-6.

118. T. Ling, L. Xie, J. Zhu, H. Yu, H. Ye, R. Yu, Z. Cheng, L. Liu, L. Liu, G. Yang, Z. Cheng, Y. Wang, X. Ma., "Icosahedral Face Centered Cubic Fe Nanoparticles: Facile Synthesis and Characterization with Aberration-Corrected TEM" *Nano Lett.,* Vol. 9, No.4, 2009, pp. 1572-1576.

119. K. Kwon, K. Y. Lee, Y. W. Lee, M. Kim, J. Heo, S. J. Ahn, S. W. Han, "Controlled Synthesis of Icosahedral Gold Nanoparticles and Their Surface-Enhanced Raman Scattering Property" *J. Phys. Chem. C*, Vol. 111, No. 3, 2007, pp. 1161-1165.

120. D. Reinhard, B. D. Hall, D. Ugarte, and R. Monot, “Size-independent fcc-to-icosahedral structural transition in unsupported silver clusters: An electron diffraction study of clusters produced by inert-gas aggregation” Phys. Rev. B 55, 7868 -7881 (1997).

121. Q. Zhang, J. Xie, J. Yang, J. Y. Lee, “Monodisperse Icosahedral Ag, Au, and Pd Nanoparticles: Size Control Strategy and Superlattice Formation” *ACS Nano,* Vol. 3, No. 1, 2009, pp. 139-148.

122. Z. Zhang, W. Hu, S. Xiao, “Melting, melting competition, and structural transitions between shell-closed icosahedral and octahedral nickel nanoclusters”, *Phys. Rev. B*, Vol. 73, No. 12, 2006, pp. 125443-1-8**.**

123. T. X. Li, S. M. Lee, S. J. Han, G. H. Wang, “Structural transitions of Au_{55} isomers”, Phys. Lett. A, Vol. 300, No.1, 2002, pp. 86–92.

124. D. J. Wales. L. J. Munro, “Changes of Morphology and Capping of Model Transition Metal Clusters” *J. Phys. Chem.*, Vol. 100, No. 6, 1996, pp. 2053-2061.

125. K. Sato, W. J. Huang, F. Bohra, S. Sivaramakrishnan, A. P. Tedjasaputra, J. M. Zuo, “Size-dependent structural transition from multiple-twinned particles to epitaxial fcc nanocrystals and nanocrystal decay” *Phys. Rev. B*, Vol. 76, No. 14, 2007, 144113-1-8**.**

126. N. P. Young, M. A. van Huis, H. W. Zandbergen, H. Xu, A. I. Kirkland, “Transformations of gold nanoparticles investigated using variable temperature high-resolution transmission electron microscopy”, *Ultramicroscopy*, Vol. 110, No. 5, 2010, pp. 506-516.

127. S. Valkealahti, M. Manninen, “Instability of cuboctahedral copper clusters”, *Phys. Rev. B*, Vol. 45, No. 16, 1992, pp. 9459-9462.

128. K. Koga, T. Ikeshoji, K. Sugawara, “Size- and Temperature-Dependent Structural Transitions in Gold Nanoparticles” *Phys. Rev. Lett.*, Vol. 92, No. 11, 2004, pp. 115507-1-4.

129. B. Cheng, A. H. W. Ngan, “Thermally Induced Solid-Solid Structural Transition of Copper Nanoparticles through Direct Geometrical Conversion”, *J. Chem. Phys.*, Vol. 138, No. 16, 2013, pp. 164314-1-11.

130. F. Thummler, W. Thomma, “The Sintering Process”, *Int. Met. Rev.*, Vol. 12, No. 1, 1967, pp. 69-108.

131. G. C. Kuczynski, “Study of the Sintering of Glass”, *J. Appl. Phys.*, Vol. 20, No. 12, 1949, pp. 1160-1163.

132. W. D. Kingery, M . Berg, “Study of the Initial Stages of Sintering Solids by Viscous Flow, Evaporation-Condensation, and Self-Diffusion”, *J. Appl. Phys.*, Vol. 26, No. 10 1955, pp.1205-1212.

133. M. J. Readey, D. W. Readey. “Sintering of ZrO_2 in HCL Atmospheres*”, J. Amer. Ceram. Soc.,* Vol. 69, No. 7, 1986, pp. 580-582.

134. G. C. Kuczynski, “Self-Diffusion in Sintering of Metallic Particles”, *Trans. AIME*, Vol. 185, 1949, pp. 169-178.

135. W. Schatt, W. Hermel, E. Friedrich, P. Lanyi “On the status of Sintering Theory of One-Component Systems” *Sci. Sinter.*, Vol 15, 1993, pp. 5-26.

136. R. L. Coble, “Initial Sintering of Alumina and Hematite”, *J. Amer. Ceram. Soc.,* Vol. 41, No. 2, 1958, pp. 55-62.

137. F. B. Swinkels, M. F. Ashby “Role of Surface Redistribution in Sintering by Grain Boundary Transport”, *Powder Met.*, Vol. 23, No.1, 1980, pp. 1-6.

138. W. Schatt, E. Friedrich, K. P. Wieters “Dislocation-Activated Sintering”, *Rev. Powder Met. Phys. Ceram.*, Vol. 3, 1986, pp. 1-111.

139. C. S. Morgan “Material Transport by Dislocation Motion in Sintering”, *Phys. Sinter.*, 1973, Vol. 5, No. 1, 1973, pp. 31-39.

140. J. H. Jean, T. K. Gupta, “Liquid Phase Sintering in the Glass-Cordierite System”, *J. Mater. Sci.*, Vol. 27, No. 6, 1992, pp. 1575-1584.

141. A. P. Savitskii, E. S. Kim, L. S. Martsunova “Compact Shrinkage During Liquid-Phase Sintering” *Soviet Powder Met. Metal Ceram.*, Vol. 19, No. 9, 1980, pp. 593-596.

142. R. M. German. “Formation of Necklace Microstructure During Liquid Phase Sintering: Model Calculations” *Intern. J. Powder Met.*, Vol. 22, 1886, pp.31-38.

143. A. P. Savitskii, “Current Views on the Processes of Sintering in the Presence of a Liquid Phase” *Soviet Powder Met. Metal Ceram.*, Vol. 26, No. 8, 1987, pp. 631-636.

144. R. Ge “Development of a New Hot-Pressing Equation in Powder Metallurgy*” Powder Met. Intern.*, Vol. 24, No. 4, 1992, pp. 229-232.

145. E. K. H. Li, P. D. Funkenbusch, “Hot Isostatic Pressing (HIP) of Powder Mixtures and Composites: Packing, Densification, and Microstructural Effects”, *Met. Trans. A*, Vol. 24, No. 6, 1993, pp. 1345-1354.

146. J. Besson, M. abouaf, “Grain Growth Enhancement in Alumina During Hot Isostatic Pressing”, *Acta. Met. Mater*., Vol. 39, No. 10, 1991, pp. 2225-2234.

147. S. Arcidiacono, N.R. Bieri, D. Poulikakos, C.P Grigoropoulos, “On the coalescence of Gold Nanoparticles”, *Int. J. Multiphase Flow*, Vol. 30. No. 7-8, 2004, pp. 979-994.

148. P. Zeng, S. Zajac, P. C. Clapp, J.A. Rifkin, “Nanoparticle Sintering Simulations”, *Mat. Sci. Eng. A*, Vol. 252, No. 2, 1998, pp. 301-306.

149. H. Zhu, R. S. Averback, “Molecular Dynamics Simulations of Densification Processes in Nanocrystalline Materials” *Mat. Sci. Eng. A* , Vol. 204, No. 1-2, 1995, pp. 96-100.

150. B. S. Bokstein, H.D. Bröse, L. I. Trusov, T. P. Khvostantseva, “Diffusion in Nanocrystalline Nickel” *Nanostruct. Mater*., Vol. 6, No. 5-8, 1995, pp. 873-876.

151. K. Moon, H. Dong, R. Maric, S. Pothukuchi, A. Hunt, Y. Li, C.P. Wong, “Thermal behavior of silver nanoparticles for low-temperature interconnect applications”, *J. Electron. Mater.*, Vol. 34, No. 2, 2005, pp. 168-175.

152. H. Alarifi, A. Hu, M. Yavuz, Y. Norman Zhou. “Pressureless Sintering Behavior of Ag Nanoparticles at Low Temperatures”, *Materials Science and Technology Conference*, Vol. 4, 2010, pp. 2633-3641.

153. D. Wakuda, M. Hatamura, K. Suganuma, “Novel method for room temperature sintering of Ag nanoparticle paste in air”, *Chem. Phys. Lett.*, Vol. 441, No 4-6, 2007, pp. 305-308.

154. D. Wakuda, K. Kim, K. Suganuma, “Room-Temperature Sintering Process of Ag Nanoparticle Paste”, *IEEE Trans. Compon. Packag. Technol.*, Vol. 32, No.3, 2009, pp. 627-632.

155. J. Rankin, B. W. Sheldon “In situ TEM sintering of nano-sized ZrO_2 particles”, *Mat. Sci. Eng. A*, Vol. 204, No. 1-2, 1995, pp. 48-53.

156. H. Zhu, R. S. Averback “Sintering of Nano-Particle Powders: Simulations and Experiments” Mater. Manuf. Process, Vol. 11, No. 6, 1996, pp. 905-923.

157. J. Y. Guo, C. X. Xu, A. M. Hu, K. D. Oakes, F. Y. Sheng, Z. L. Shi, J. Dai, Z. L. Jin, “Sintering dynamics and thermal stability of novel configurations of Ag cluster”, *J. Phys. Chem. Solids*, Vol. 73, No. 11, 2012, 1350-1357.

158. M. Yeadon, J. Yang, R. Averback, J. Bullard, J. Gibson, “Sintering of silver and copper nanoparticles on (001) copper observed by in-situ ultrahigh vacuum transmission electron microscopy”, *Nanostruct. Mater.*, Vol. 10, No.5, 1998, pp. 731-739.

159. F. Hussain, S. S. Hayat, M. Imran, S. A. Ahmad, F. Bouafia “Sintering and deposition of nanoparticles on surface of metals: A molecular dynamics approach”, *Comp. Mater. Sci.*,Vol. 65, 2012, pp. 264–268.

160. D. V. Goia, E. Matijević, “Preparation of Monodispersed Metal Particles”, *New J. Chem.*, Vol. 22, No. 11, 1998, pp. 1203-1215.

161. P. C. Lee, D. Meisel, “Adsorption and Surface-Enhanced Raman of Dyes on Silver and Gold Sols”, *J. Phys. Chem.*, Vol. 86, No. 17, 1982, pp. 3391-95.

162. Y. Badr, M.G. Abd El Wahed, M.A. Mahmoud, “On 308 nm Photofragmentation of the Silver Nanoparticles”, *Appl. Surf. Sci.*, Vol. 253, No.5, 2006, pp. 2502-2507.

163. Y. Tan, Y. Li, D. Zhu, “Preparation of Silver Nanocrystals in the Presence of Aniline”, *J. Colloid. Interf. Sci.*, Vol. 258, No. 2, 2003, pp. 244-251.

164. R. D. Deegan, “Pattern Formation in Drying Drops” *Phys. Rev. E,* Vol. 61, No. 1, 2000, pp. 475-485.

165. M. Atis, C. Ozdogan, Z. B. Guvenc, “Parallelization of a Molecular Dynamics Simulation of an Ion-Surface Collision System: Ar–Ni(100)”, *Int. J. Mod. Phys. C*, Vol. 16, No. 6, 2005, pp. 969-990.

166. A. F. Voter, *Los Alamos Unclassified Technical Report LA-UR 93-3901*, 1993.

167. S. M. Foiles, M. I. Baskes, M. S. Daw, “Embedded-Atom-Method Functions for the FCC Metals Cu, Ag, Au, Ni, Pd, Pt and their alloys”, *Phys. Rev. B*, Vol. 33, No. 12, 1986, pp. 7983-7991.

168. V. J. Grigoryan, D. Alamanova, M. Springborg, “Structure and Energetics of Cu_N Clusters with ($2 \leq N \leq 150$): An Embedded-Atom-Method Study”, *Phys. Rev. B,* Vol. 73, No. 11, 2006, 115415-1−13.

169. J. P. K. Doye, D. J. Wales, “Global Minima for Transition Metal Clusters Described by Sutton-Chen Potentials”, *New J. Chem.*,Vol. 22, No. 7, 1998, pp. 733−744.

170. S. Darby, T. V. Mortimer-Jones, R. L. Johnston, C. Roberts, “Theoretical Study of Cu-Au Nanoalloy Clusters Using a Genetic Algorithm”, *J. Chem. Phys.*, Vol. 116, No. 4, 2002, pp. 1536−1550.

171. M. W. Finnis, J. E. Sinclair, “A Simple Empirical N-body Potential for Transition Metals”, *Philos. Mag. A*, Vol. 50, No. 1, 1984, pp. 45−55; and Vol. 53, No. 1 1986, pp. 161−161.

172. J. García-Rodeja, C. Rey, L. J. Gallego, J. A. Alonso, “Molecular-Dynamics Study of the Structures, Binding Energies, and Melting of Clusters of FCC Transition and Noble metals Using the Voter and Chen Version of the Embedded-Atom Model”, *Phys. Rev. B*, Vol. 49, No. 12, 1994, pp. 8495−8498.

173. C. Kuiying, L. Hongbo, L. Xiaoping, H. Qiyong, H. Zhuangqi, “Molecular Dynamics Simulation of Local Structure of Aluminium and Copper in Supercooled Liquid and Solid State by Using EAM”, *J. Phys.: Condens. Matter.*, Vol. 7, No. 12, 1995, pp. 2379−2394.

174. S. Chantasiriwan, F. Milstein, “Higher-Order Elasticity of Cubic Metals in the Embedded-Atom Method” *Phys. Rev. B*, Vol. 53, No. 21, 1996, pp. 14080−14088.

175. S. Chantasiriwan, F. Milstein, “Embedded-Atom Models of 12 Cubic Metals Incorporating Second- and Third-Order Elastic-Moduli Data” *Phys. Rev. B*, Vol. 58, No. 10, 1998, pp. 5996−6005.

176. L. G. González, J. M. Montejano-Carrizales, “Embedded Atom Method Applied to Ni, Cu, Ag, and Pd” *Phys. Status Solidi B*, Vol. 220, No. 1, 2000, pp. 357−362.

177. L. B. Hansen, P. Stoltze, J. K. Nørskov, B. S. Clausen, W. Niemann, “Is There a Contraction of the Interatomic Distance in Small Metal Particles?” *Phys. Rev. Lett.*, Vol. 64, No. 26, 1990, pp. 3155−3158.

178. O. B. Christensen, K. W. Jacobsen, “The Coupling between Atomic and Electronic Structure in Small Cu Clusters” *J. Phys.: Condens. Matter*, Vol. 5, No. 31, 1993, pp. 5591−5602.

179. E. E. Zhurkin, M. Hou, “Structural and Thermodynamic Properties of Elemental and Bimetallic Nanoclusters: An Atomic Scale Study” *J. Phys.: Condens. Matter*, Vol. 12, No. 30, 2000, pp. 6735−6754.

180. T. Zhang, A.-L. Wu, L. Guan, Y.-H. Qi, “Simulations of Metal Cu in Heating Process”. *Chin. J. Chem.*, Vol. 22, No. 2, 2004, pp. 148−151.

181. M. Kabir, A. Mookerjee, A. K. Bhattacharya, “Structure and Stability of Copper Clusters: A Tight-Binding Molecular Dynamics Study”, *Phys. Rev. A*, Vol. 69, No. 4, 2004, pp. 043203-1−10.

182. D. Schebarchov, S. C. Hendy, “Static, Transient, and Dynamic Phase Coexistence in Metal Nanoclusters” *J. Chem. Phys.*, Vol. 123, No. 10, 2005, pp. 104701-1−9.

183. M. S. Daw, M. I. Baskes, “Embedded-Atom Method: Derivation and Application to Impurities, Surfaces, and Other Defects in Metals” *Phys. Rev. B*, Vol. 29, No. 12, 1984, pp. 6443−6453.

184. Q. Jiang, X. H. Zhou, M. Zhao, “Nucleation Temperature of Elements”, *J. Chem. Phys.*, Vol. 117, No. 22, 2002, pp. 10269-1-5.

185. S. Zhao, S. Wang, H. Ye, “Size-Dependent Melting Properties of Free Silver Nanoclusters” *J. Phys. Soc. Jpn.*, Vol. 70, No. 10, 2011, pp. 2953-2957.

186. Q. Jiang, S. H. Zhang, J. C. Li, ”Grain size-dependent diffusion activation energy in nanomaterials”, *Solid State Commun.*, Vol. 130, No. 9, 2004, pp. 581-584.

187. W. K. Lee, R. L. Eadie, G. C. Weatherly, K. T. Aust, “A study of the sintering of spherical silver powder-II. The intial Stage” Acta Metall. Vol. 26, No. 12, 1978, pp. 1837-1843.

188. F. E. Kruis, K. A. Kusters, S. E. Pratsinis, B. Scarlett “A Simple Model for the Evolution of the Characteristics of Aggregate Particles Undergoing Coagulation and Sintering”, *Aerosol Sci. Tech.*, Vol. 19 , No. 4, 1993, pp. 514-526.

189. M. I. Alymov, E. I. Maltina, Y. N. Stepanov, “Model of Initial Stage of Ultrafine Metal Powder Sintering”, *Nanostruct. Mater.*, Vol. 4, No. 6, 1994, pp. 737-742.

190. H. Alarifi, A. Hu, M. Yavuz, Y. Zhou, “Silver Nanoparticle Paste for Low-Temperature Bonding of Copper”, *J. Electron. Mater.*, Vol. 40, No. 6, 2011, pp. 1394-1402.

191. A. Hu, J.Y. Guo, H. Alarifi, G. Patane, Y. Zhou, G. Compagnini, C. X. Xu, “Low temperature sintering of Ag nanoparticles for flexible electronics packaging”, *Appl. Phys. Lett.*, Vol. 97, No. 15, 2010, pp. 153117-1-3.

192. H. Tada, J. Bronkema, A. T. Bell, “Application of In *Situ* Surface-Enhanced Raman Spectroscopy (SERS) to the Study of Citrate Oxidation on Silica-Supported Silver Nanoparticles”, *Catal. Lett.*, Vol. 92, No. 3-4, 2004, pp. 93-99.

193. E. L. Force, A. T. Bell, “Infrared Spectra of Adsorbed Species Present during the Oxidation of Ethylene over Silver”, *J. Catal.*, Vol. 38, No. 1-3, 1975, pp. 440-460.

194. O. A. Yeshchenko, I. M. Dmitruk, A. A. Alexeenko, A. V. Kotko, “Surface Plasmon as a Probe for Melting of Silver Nanoparticles”, *Nanotechnology*, Vol. 21, No. 4, 2010, 045203-1–6.

195. T. Castro, R. Reifenberger, E. Choi, R. P. Andres, “Size-Dependent Melting Temperature of Individual Nanometer-Sized Metallic Clusters”, *Phys. Rev. B,* Vol. 42, No. 13, 1990, pp. 8548-8556.

196. R.-X. Dong, C.-C. Chou, J.-J. Lin, "Synthesis of Immobilized Silver Nanoparticles on Ionic Silicate Clay and Observed Low-Temperature Melting", *J. Mater. Chem.*, Vol. 19, No. 15, 2009, pp. 2184–2188.

197. C.-W. Chiu, P.-D. Hong, J.-J. Lin, "Clay-Meditated Synthesis of Silver Nanoparticles Exhibiting Low-Temperature Melting" *Langmuir*, Vol. 27, No. 18, 2011, pp. 11690–11696.

198. N. H. Kim, J. Y. Kim, K. J. Ihn "Preparation of Silver Nanoparticles Having Low Melting Temperature Through a New Synthetic Process without Solvent" *J. Nanosci. Nanotechnol*, Vol. 7, No. 11, 2007, pp. 3805–3809.

199. M. A. Asoro, D. Kovar, J. Damiano, P. J. Ferreira "Scale Effect on the Melting Behavior of Silver Nanoparticles" *Microsc. Microanal.*, Vol. 16, No. S2, 2010, pp. 1802–1803.

200. Atiş, M.; Aktaş, H.; Güvenç, Z. B. Structures and Melting of AgN (N = 7, 12−14) Clusters. Modell. Simul. Mater. Sci. Eng. 2005, 13, pp. 1411−1432.

201. H. A. Alarifi, M. Atis, C. Ozdogan, A. Hu, M. Yavuz, Y. Zhou "Determination of Complete Melting and Surface Premelting Points of Silver Nanoparticles by Molecular Dynamics Simulation", *J. Phys. Chem. C*, Vol. 117, No. 23, 2013, pp. 12289-12298.

202. L. D. Marks, "Modified Wulff Constructions for Twinned Particles", *J. Cryst. Growth*, Vol. 61, No. 3, 1983, pp. 556-566.

203. R. P. Gupta, "Lattice Relaxation at a Metal Surface" *Phys. Rev. B*, Vol. 23, No. 12, 1981, pp. 6265−6270.

204. V. V. Hoang, "Melting of Simple Monoatomic Amorphous Nanoparticles" *J. Phys. Chem.* C, Vol. 116, No. 27, 2012, pp. 14728−14735.

205. V. P Skripov, V. P. Koverda, V. N. Skokov, "Size Effect on Melting of small Particles", *Phys. Status Solidi A*, Vol. 66, No. 1, 1981, pp. 109-118.

206. R. Garrigos, P. Cheyssac, R. Kofman, "Melting for Lead Particles of Very Small Sizes; Influence of Surface Phenomena", *Z. Phys. D*, Vol. 12, No. 1-4, 1989, pp. 497-500.

207. T. Karabacak, J. S. DeLuca, Pei-I Wang, G. A. Ten Eyck, D. Ye, Gwo-Ching Wang, Toh-Ming Lu, "Low Temperature Melting of Copper Nanorod Arrays", *J. Appl. Phys.*, Vol. 99, No. 6, 2006, pp. 064304-1-6.

208. S. M. Foiles, M. I. Baskes, "Contributions of the Embedded-Atom Method to Materials Science and Engineering" *MRS Bull.*, Vol. 37, No. 5, 2012, pp. 485−491.

209. S. J. Zhao, S. Q. Wang, D. Y. Cheng, H. Q. Ye, “Three Distinctive Melting Mechanisms in Isolated Nanoparticles” *J. Phys. Chem. B*, Vol. 105, No. 51, pp. 12857−12860.

210. H. A. Alarifi, M. Atis, C. Ozdogan, A. Hu, M. Yavuz, Y. Zhou,.”Molecular Dynamics Simulation of Sintering and Surface Premelting of Silver Nanoparticles” *Mater. Trans*., Vol. 54, No. 6, 2013, pp. 884-889.

211. D. R. Askeland, P. P. Phulé: The Science and Engineering of Materials, 5th Ed., (Thomson, Toronto, Canada, 2006) p. 129.

212. V. Tikare, M. Braginsky, D. Bouvard, A. Vagnon “Numerical simulation of microstructural evolution during sintering at the mesoscale in a 3D powder compact” *Comp. Mater. Sci*., Vol. 48 , 2010, pp. 317-325.